UNIVERSITÀ DEGLI STUDI DI UDINE
hic sunt futura

FONDAZIONE BRUNO KESSLER

PhD Course in Computer Science, Mathematics and Physics
XXXIV Cycle

Radiation damage of FBK Silicon Photomultipliers for HEP applications

Author:
Anna Rita Altamura

Supervisor:
Dr. Alberto Gola

Co-Supervisor:
Prof. Andrea Vacchi

Academic Year 2020/2021

"Le lavagne vanno cancellate anche quando sopra ci hai scritto grandi verità, perché gli altri possano scriverci le loro."

(C.Valerio - La matematica è politica)

To all those searching for their place in the world,
To all those fighting to hold on to it,
To the forgotten ones,
To the discriminated ones

If the world is not fair,
Thank God science is.

Abstract

Silicon Photomultipliers (SiPMs) are photo-detectors currently experiencing a significant development in several fields: from medical applications to LiDAR, homeland security, analytical instrumentation, High Energy Physics (HEP). In particular, this work deals with SiPMs in HEP with a focus on their tolerance to the radiation. In fact, in HEP sensors are usually exposed to a large amount of radiation and they are expected to survive in such an environment.

After a detailed introduction on the main SiPM characteristics, the main mechanisms of damage in SiPMs are addressed. They mainly consist into the generation of defects into the bulk, resulting in an increase of the noise, and in the surface layer, resulting in the generation of fixed charge in the oxide and defects at interface between the oxide and the silicon and, as a consequence, in an increase of the leakage current. This work aims to verify these theoretical assumptions through three irradiation test campaigns, where FBK SiPMs are exposed to the effects of both ionizing and non-ionizing radiation at medium-high doses.

The first irradiation test took place at the Laboratori Nazionali del Sud (LNS) in 2019, where SiPMs were exposed to increasing 62 MeV proton fluences up to about 10^{14} n_{eq}/cm^2. The main SiPMs parameters were assessed after irradiation and some information about the damage into the bulk of the sensors were derived. In fact, the noise was observed to increase significantly with respect to the non-irradiated SiPM, as expected from theory. Information were then extracted about activation energy, and a preferred spatial localization of the defects inside the single microcell was also observed.

During the second irradiation test, FBK SiPMs were irradiated at the Trento Protontherapy Center with 74 MeV protons at increasing fluences, up to 6.4×10^{11} n_{eq}/cm^2, using a custom setup which allowed direct reverse current-voltage measurement shortly after each irradiation step, reducing the impact of the annealing on the results. SiPMs were characterized extracting DCR, breakdown voltage and other key parameters from reverse current measurements. Then, the several technologies under test were compared using figures of merit such as Signal-to-Noise Ratio (SNR) and energy resolution, in X-rays or γ-rays spectroscopy, assumed as possible applications. The NUV-HD technologies with smaller cell sizes showed the best best performances, in terms of energy resolution, SNR and noise level after annealing.

The third irradiation campaign aimed to test the tolerance of FBK SiPMs to ionizing radiation through an X-rays irradiation at the TIFPA facility in Trento up to a dose of 100 kGy. SiPMs were irradiated using the same custom setup used in the second irradiation test, performing reverse current measurement after each irradiation step. After a 30-day annealing, samples irradiated at 100 kGy were fully characterized and compared to the non-irradiated ones. RGB-HD was the only technology to show a decrease of the PDE due to border effects in the electric field inside the microcells of the SiPM, while the NUV-HD-cryo was the only technology not showing variations neither in the noise nor in the PDE.

Contents

Introduction

Silicon sensors are semiconductor devices used to detect particles. The kind of particles detected depends on the application. In this thesis the attention will be focused mainly on photo-sensors or photo-detectors, which detect electromagnetic radiation.

The long story of the silicon sensors begins in 1905, when Albert Einstein submits a paper called *Über einen die Erzeugung und Verwandlung des Lichtes betreffenden heuristischen Gesichttspunkt* ("On a Heuristic Viewpoint Concerning the Production and Transformation of Light"), where he suggests a completely new way of conceiving the light and its nature. In fact, until then the light was supposed to have only an electromagnetic nature, as described by James Clerk Maxwell in 1865 in his *A Dynamical Theory of the Electromagnetic Field* paper, starting the classical theory of the electromagnetic radiation.

Einstein takes Plank's *quantum theory*, which states that the electromagnetic waves emit energy in the form of energy packets, the quanta, through the well-known formula:

$$E = h\nu = h\frac{c}{\lambda}$$

where h is the *Planck's constant* and ν is the frequency of the elecromagnetic wave.

Einstein's theory marks a turning point in physics and engineering. In fact, it suggests that charge carriers can be produced from light and collected to produce measurable electrical signals.

Several ways of detecting light have been developed from 1905 onward, based on the main light-matter interaction effects:

- Photoelectric effect: the photon energy is absorbed by an atom in the target material and one of the electrons of the atom is emitted, under the hypothesis that the photon energy is larger than the binding energy of the electron, thus that $E_{e^-} = E_\gamma - E_b > 0$

- Compton effect: when a photon (x-ray or γ-ray) interacts with shell electrons or free electrons, it undergoes to a scattering effect by an angle θ and the scattered photon results to have a longer wavelength (thus a lower energy) than the incident one.

- Pair production: when a photon passes by the Coulomb field of a nucleus or atomic electron, it may disappear producing an $e^- - e^+$ pair, with no energy release. The threshold energy for this effect is $E_\gamma \leq 2m_e c^2$, thus the photon energy must be higher than the sum of the rest energies of the two final particles.

As an example, the first prototype of photo-multiplier, which dates back to 1934, was based on the photoelectric effect. The device consisted of a semi-cylindrical photocathode, a secondary emitter mounted on the axis, and a collector grid surrounding the secondary emitter. The tube had a gain of about eight and operated at frequencies well above 10 kHz[1]. Further improvements of this technology over time resulted in structures with a much higher gain. For instance, this is the case of the Photomultiplier Tube (PMT), which can reach an amplification of 10^8, enabling the detection of single photons. PMT is one of the most popular devices capable of detecting single visible or near-visible photons, due to its high gain, low noise and ultra-fast response. PMT consists of a vacuum tube, including a photocatode on the entrance, which is usually a thin vapor-deposited conducting layer[1] emitting electrons through photoelectric effect when struck by photons. Electrons are then collimated toward the first internal dynode, where they are multiplied by secondary emission, and then toward the following ones. The potential applied at each dynode accelerates electrons toward the following one, until reaching the anode, which represents the last stage of this chain. In this way, an avalanche of electrons has been created. Once electrons get to the anode, these can be read as a current pulse. In Fig.1 a schematic of a PMT is shown, where the several stages of the detection chain are clearly visible.

The total gain of a PMT is usually around $10^6 - 10^8$, considering the average number of electrons generated from the primary photon. As a consequence of its high internal gain, PMT ensures a reasonably good single photon resolution, which does not need extremely low temperatures, providing a very good quantum efficiency in the NUV and visible range of the light spectrum. Furthermore, its large size range (from a few mm to even 20 inches diameter) enables to cover very large areas. On the other hand, PMT suffers of a not-negligible dependence on the magnetic field which makes it suited only to a certain number of applications. Another key feature of the PMTs is the high bias voltage required to produce such a high internal gain, estimated at around 1000-1500 V, which implies a high power consumption

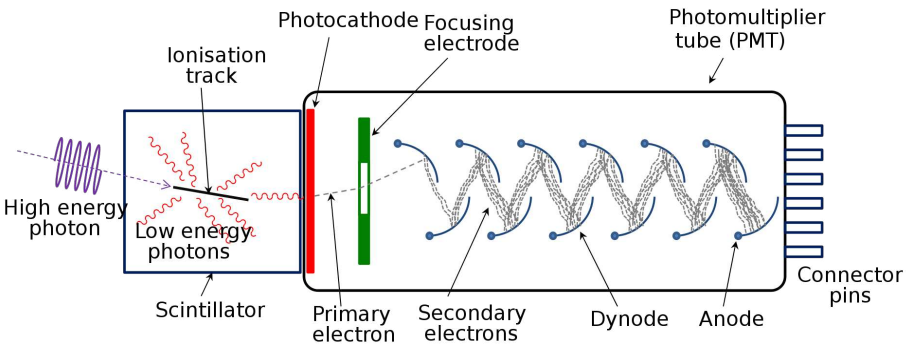

Figure 1: PMT coupled to a scintillator, showing the several stages of the detection chain[1].

for the whole lifetime of the detector. Also a stabilization period is needed before starting to operate, in the order of several hours. Furthermore, they are fragile, expensive and show problems with the cryogenic vacuum estate.

Today, PMTs are still widely used in many applications but several alternatives have been developed throughout the years, due to their fragility, their dependence on the magnetic field and the high voltage required to work properly.

One of the most valid alternatives to PMT developed so far is represented by *Solid State Sensors*, combining a good position measurement (in the range of several μm) with a high rate capability (few hundred kHz). Solid state detectors exploit the properties of the semiconductors. In particular, their characteristic of creating a p-n junction when doped is crucial in detecting light and ionizing particles. Standard solid state sensors enable to detect tens or hundreds photons as a minimum detectable light, reaching a single photon detection only at very low temperature[2, 3]. One of the first solid state technologies was the strip detector, still in use for a wide rage of applications. Strip detectors resulted to have a rather low efficiency in case of high particle densities. This led to the development of pixel detectors, which provided a more accurate spatial detection of the light. In fact, each pixel has its own readout channel and as the readout methods got faster over time, pixel detectors started to play a leading role in several applications. High energy resolutions combined with high position sensitivity brought semiconductor detectors into new applications: X-rays astronomy, synchrotron radiation experiments and many others[4].

In the last decade, multi-pixels detectors have experienced a considerable spread in a wide field of applications, including the more frequent use of detectors with internal gain, obtained through avalanche multiplication of the

charge generated in the active volume of the detector by impact ionization. One of the most interesting detectors among avalanche detectors is the Silicon Photomultiplier (SiPM), a silicon detector made of several pixels (SPADs) working in Geiger mode and connected in parallel. Contrary to standard APD detectors, SiPMs combine a low bias voltage, an excellent single photon resolution (because of their high ENF, silicon APDs cannot count the single photons), a significant compactness and a negligible sensitivity to magnetic field. Furthermore, their high gain and very good Photo Detection Efficiency in the NUV and visible range in the light spectrum made them the detector of choice for several experiments over the last years. In particular, SiPMs are suitable for a wide range of applications, such as nuclear medicine [5], large physics experiments [6], optical spectroscopy [7, 8], automotive LiDAR [9], etc.

When applied to High Energy Physics (HEP), SiPMs are usually expected to survive to a huge amount of radiation, which can produce a significant radiation damage leading to a gradual deterioration of their performance. For example, Fig.2 shows the dose and the fluence expected in the electromagnetic calorimeter (ECAL) of CMS experiment during the Phase-2 upgrade, which represents an example of the amount of radiation to which silicon sensors are usually exposed. In particular, the dose is related to the ionizing radiation, while the fluence (cm^{-2}) takes into account the non-ionizing radiation and it is usually measured as the number of 1 MeV neutron equivalent over a 1 cm^2 area.

When the SiPM is too much damaged and noise becomes comparable with signal, the sensor is no longer reliable, the sensitivity to the single photon is lost and the sensor must be replaced with a new one. This has implications in terms of time and cost which could affect the sustainability of the experiments.

This issue opens a completely new research field: the radiation hardness of the SiPMs. This thesis arises form the need of testing FBK (Fondazione Bruno Kessler, Trento) SiPMs with the main purpose of searching for potential new layout and fabrication combinations to improve their radiation hardness. This was accomplished by irradiating as many FBK technologies as possible, with both protons and X-rays to test the radiation damage induced by non-ionizing and ionizing radiation. The response of the several technologies under test to the radiation were compared and some conclusions were drawn. Due to the wide range of applications of the FBK SiPMs, some parameters were assessed considering some particular use cases, such as X-ray spectroscopy and calorimetry.

In the first chapter, a brief introduction of the physics of semiconductors will be provided, showing their main characteristics and the equations gov-

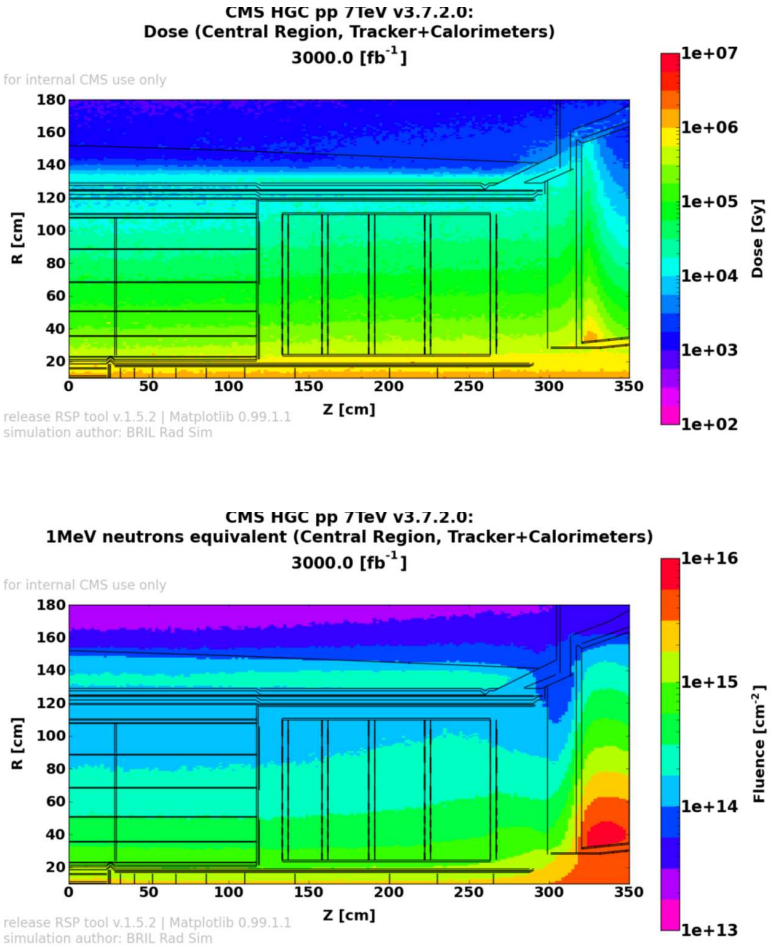

Figure 2: Total dose and 1 MeV neutron equivalent hadron fluence accumulated in the ECAL Barrel region for an integrated luminosity of 3000 fb^{-1} as predicted by FLUKA for the CMS detector in the Phase-2 configuration[10].

erning them, first from a general point of view, then with a focus on the ones relevant for SiPMs.

In the second chapter, an overview of the main radiation damage mechanisms will be shown, where the several damage types will be analysed and a theoretical representation will be provided together with a brief state of the art description, from both a macroscopic and a microscopic point of view.

In the third chapter, an irradiation test at high flucences with protons at the Laboratori Nazionali del Sud (LNS, INFN) in Catania (Italy) will be described, the main results obtained on several SiPM technologies will be assessed and some preliminary conclusion will be drawn.

In the fourth chapter, an irradiation test at lower fluences at the Trento Proton Therapy Center will be described, with a particular focus on the accuracy of the current measurements taken online shortly after each irradiation step, to reduce annealing effects and obtain information about the effective damage mechanisms.

The fifth chapter will deal with an X-ray irradiation campaign at TIFPA (INFN) laboratories in Trento. The effects of the ionization radiation will be assessed and a comparison with the effect of the non-ionizing radiation will be provided.

Lastly, the main results will be summarized and conclusions will be drawn.

Chapter 1

Silicon photo-multipliers

In the first part of this chapter, the main features of the physics of semiconductors and their application to silicon sensors are described. This might help to better understand the mechanisms regulating the functioning of silicon sensors with a focus on Silicon Photomultipliers. Then, Silicon Photomultipliers with their physics properties and parameters are introduced, with a focus on the FBK SiPMs, which represent the leading figures of this thesis.

1.1 Phisics of Semiconductors

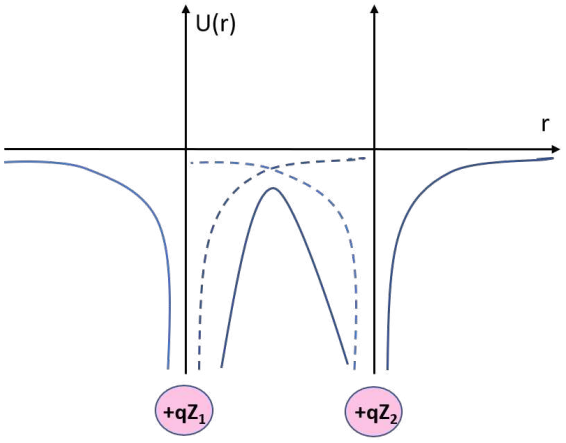

Figure 1.1: Potential energy of two atoms in a crystal as a function of the distance

Given two atoms in a crystal at a certain distance, their potential energy U(r) appears as in Fig.1.1, where a superposition of the energies from the two

charges is visible along the r-axis. On the borders, which can be defined as the surface of a crystal, we can always see a potential barrier which prevents the electron charges to escape the crystal, although they are free to move inside. From the quantum mechanics and the many-body theory in solid state physics we know that a many-body system with several atoms will result in a molecular system with energy orbitals[1] given by a composition of the orbitals of the constituent atoms. The simplest form of molecular orbitals is represented by the "*Linear combinations of atomic orbitals (LCAO)*", where the molecular orbitals are the result of a linear combination of the atomic orbitals of the single atoms. In the specific case of a two-atoms system, the final equation of the orbital states are:

$$\Psi = c_a \Psi_a + c_b \Psi_b \tag{1.1}$$

$$\Psi^* = c_a \Psi_a - c_b \Psi_b \tag{1.2}$$

where Ψ and Ψ^* are the bonding[2] and anti-bonding[3] states, representing the new molecular orbitals. In Fig.1.2 a molecular system with two identical atoms is visible. The E_s level represents the energy level of the s orbital in the atoms, the E_Ψ and $E_{\Psi *}$ represent the bonding and anti-bonding energy states, respectively.

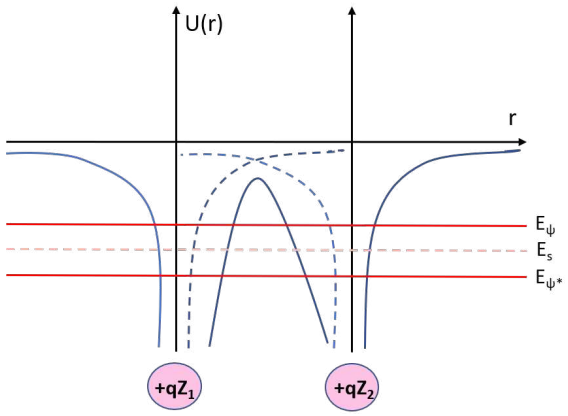

Figure 1.2: Two-atoms system with molecular orbitals

In a more complex layout made by several atoms, the potential takes a periodic pattern with the same period as the one of the crystal lattice,

[1] probability function form the shell model describing the behaviour of single or composite fermions inside an atom, a molecule or a nucleous

[2] in-phase interaction of the atomic orbitals

[3] out-of-phase interaction of the atomic orbitals

resulting in multiple orbital molecular states. If we consider an ideal system composed of n IV-group atoms ($2s^2 2p^2$), the final energy states scheme are shown in Fig.1.3 where three stages can be observed (from right to left):

- *Free atoms orbitals*: the atoms are placed at a distance larger than the lattice spacing of the crystal, thus their orbitals are free
- *Bonding configuration*: the two atoms are placed at the lattice spacing distance and their orbitals start to merge
- *Bonding/Antibonding states*; the molecular orbitals are at their final stable state, producing bonding and anti-bonding states at different energy levels

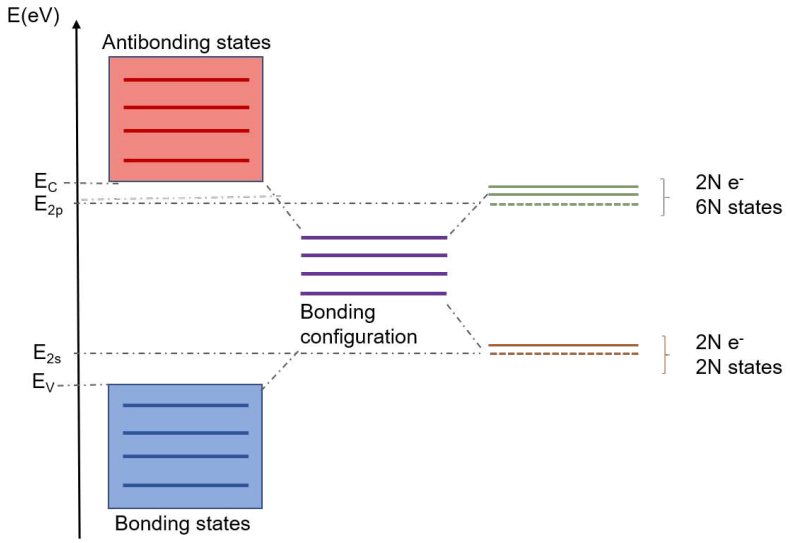

Figure 1.3: Molecular orbitals formation form atomic orbitals

A different prospective of the whole process is visible in Fig.1.4, where the energy of the orbital levels is plotted as a function of the lattice spacing d. At high d the free atom orbitals are the only possible configuration while reducing the lattice spacing, the merging process starts to form bonding and anti-bonding states, resulting in two energy bands: *conduction band (CB)* and *valence band (VB)*. The energy range between the conduction and the valence band is called *Energy gap (E_g)* and it will be one of the key parameters for the rest of this work, as we will see in the next chapters. The energy gap is nominally defined as:

$$E_g = E_c - E_v \tag{1.3}$$

where E_c is the minimum energy of the conduction band and E_v is the maximum energy of the valence band.

Knowing the lattice spacing of a crystal, from the plot in Fig.1.4 we can derive some of the properties of that crystal, as for example the Tin (Sn), which has a lattice spacing of 6.25 $\mathring{A}$ and lies inside the single band region without a band split. Another example can be the Silicon (Si) which, with a lattice spacing of 5.34 $\mathring{A}$, is located exactly inside the double bands region, with an energy gap of 1.12 eV at room temperature. This latter crystal belong to the group of the so-called **Semiconductors**, which means that the energy gap is small enough to allow the electrons to move from the VB to the CB after acquiring some energy from the lattice vibrations at room temperature, as we will discuss in detail in the following sections.

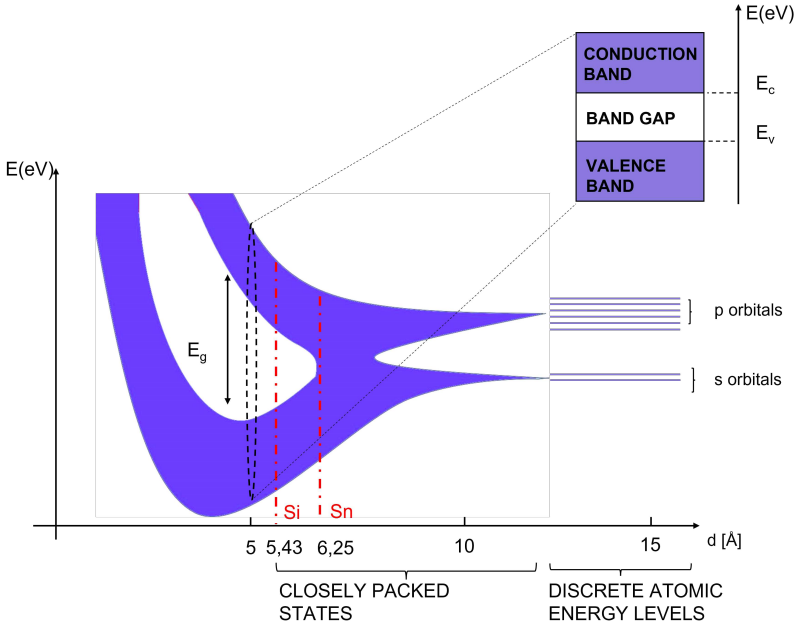

Figure 1.4: Schematic of the energy bands creation from atomic orbitals.

In absence of a strong electric field, at $T = 0\ K$ a semiconductor has a completely empty conduction band, thus it is not able to conduct. At $T > 0\ K$, due to the thermal generation, there is a non-negligible probability to find electrons in the conduction band, depending on the size of the energy gap. When an electron rises in the conduction band, it leaves behind in the valence band an empty space, that we can assume as a positive charge. It is the so-called *hole*.

The density of the states g(E) in the CB and VB can be estimated as:

$$g_{CB}(E) = \frac{4\pi}{h^3}(2m_n^*)^{3/2}(E - E_C)^{1/2} \tag{1.4}$$

$$g_{VB}(E) = \frac{4\pi}{h^3}(2m_p^*)^{3/2}(E_v - E)^{1/2} \tag{1.5}$$

where h is the *Planck constant*, m_n^* and m_p^* are the so-called *Effective Masses* of the charge carriers in the conduction and valence band respectively, due to the interaction of the carrier with the periodic potential in the crystal. Indeed, the N_{CB} and N_{VB} functions, which have a very similar equation, can be slightly different in the shape due to the effective mass value, which can be different in the two cases.

The probability of CB energetic states to be filled by the electrons is defined by the *Fermi function*:

$$f(E) = \frac{1}{1 + e^{\frac{E-E_F}{kT}}} \tag{1.6}$$

where k is the Boltzmann constant, T is the temperature and E_F is the so-called *Fermi level* representing the energy level where f(E) takes the value 1/2, which means that the probability of finding an occupied energetic states at the Fermi level is 50% at any given time. f(E) is generally a step function at T=0 when the probability of having an occupied state is 0 in CB and 1 in VB, from the definition of semiconductor.

The density of the filled energy levels in BC and VB can be estimated as:

$$\rho_n(E) = g_{CB} \times f(E) \tag{1.7}$$

$$\rho_p(E) = g_{VB} \times (1 - f(E)) \tag{1.8}$$

which means that the number of carriers in CB and VB respectively is given by the integral of the density functions:

$$n = \int_{E_C}^{\infty} \rho_n(E)dE = \frac{2}{h^3}(2\pi m_n^* kT)^{3/2} e^{-\frac{E_C - E_F}{kT}} = N_C(T)e^{-\frac{E_C - E_F}{kT}} \tag{1.9}$$

$$p = \int_{-\infty}^{E_V} \rho_p(E)dE = \frac{2}{h^3}(2\pi m_n^* kT)^{3/2} e^{-\frac{E_F - E_V}{kT}} = N_V(T)e^{-\frac{E_F - E_V}{kT}} \tag{1.10}$$

where N_C and N_V are the so-called *effective densities of the states*.

A visual summary of the equations observed in this section is shown in Fig.1.5 where the density of the states and the carriers densities are visible for both conduction and valence bands and the number of carriers in the two bands is graphically derived.

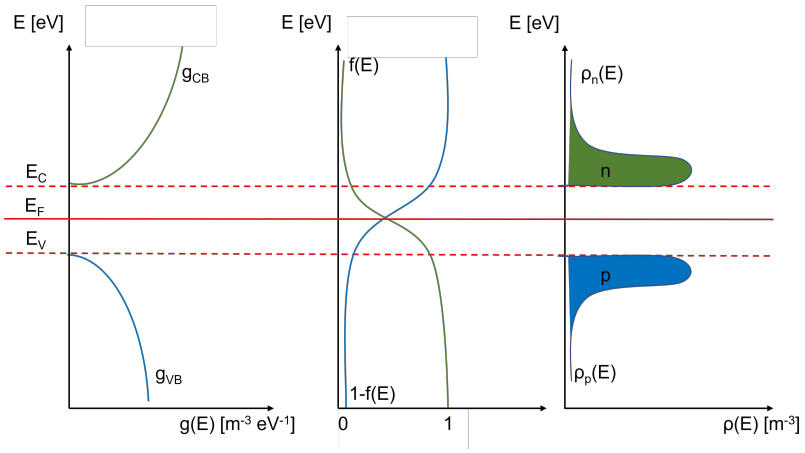

Figure 1.5: Density of states and carrier densities in the conduction and valence band.

1.1.1 Intrinsic semiconductors

An intrinsic semiconductor is define as a pure semiconductor material where no impurities are intentionally added. In this case, the generation and the recombination of the carriers in CB and VB are perfectly balanced, thus the number of carriers are the same in the two bands:

$$n = p = n_i \tag{1.11}$$

where, because of the balance between generation and recombination, n_i is not dependent on the time but it is only dependent on the semiconductor type and its temperature conditions.

From the Eq.1.11, what follows is the so-called *Law of mass action*:

$$n_i^2(T) = n(T)p(T) \tag{1.12}$$

from which, including the Eq.1.10, the n_i value can be extracted:

$$n_i^2(T) = N_C(T)N_V(T)e^{-\frac{E_g}{kT}} \tag{1.13}$$

Eq.1.13 tells us that the density of carriers due to the only thermal generation, increases as the energy gap decreases. Thus, as an example it can be stated that n_i in Silicon is much higher than in Germanium.

1.1.2 Doped semiconductors

The main issue with intrinsic semiconductors is that the number of carriers in the two bands n and p are very small at the thermal equilibrium. This

can be solved inserting external atoms into the pure semiconductor which, through an ionization process, introduce impurities into the material to alter the carriers concentrations. This process is called *doping* and the resulting material are called *doped semiconductors*.

Two types of materials are needed to release an additional amount of carriers in the two bands: *donor impurities* and *acceptor impurities*.

To better understand how these impurities work into a semiconductor, an example of donor impurities can be helpful: inserting an Arsenic (As) atom into a Silicon structure, what happens is visible in Fig.1.6, where an electron from the As atom is left outside the covalent bonds. This electron is bonded to the As nucleus and it introduces a new energy level, that we can call here E_D. The difference between the conduction band energy level E_C and the As electron level E_D is the so-called **activation energy** E_a, which represents the energy required to bring the electron up in the conduction band. A semiconductor doped with donor impurities is called *n-type*, because it increases the carrier concentration in the conduction band n.

A specular situation happens for acceptor impurities which, introduce new vacancies into the semiconductor (as for example of Boron in Fig.1.7). They also create a new energy level E_A close to the covalence band. Once the vacancies have been introduced by the new doping atoms, electrons from the valence band in the Si can jump towards the vacancies in the new energy level and in the valence band several new vacancies will be free to move into the material. In this case, the activation energy will be the difference between E_A and E_C. Semiconductors doped with acceptor impurities are called *p-type*.

It must be pointed out that not all the atoms introducing impurities are useful to improve the number of carriers in the two bands. In fact, when introducing new energy levels in the middle of the energy gap, electrons will need a large amount of energy to reach the conduction band, making the electric activation of the silicon very difficult, at room temperature at least.

In semiconductors at equilibrium, the Low of mass action is valid regardless of whether the material is doped or not.

In a doped semiconductor, the local and global neutrality principle are valid at equilibrium, which means that if we name ρ the charge density, $\rho(x) = 0$ in each point.

From this condition and Eq.1.13 we can extract the equation of the majority carriers in the case of n-type or p-type semiconductor:

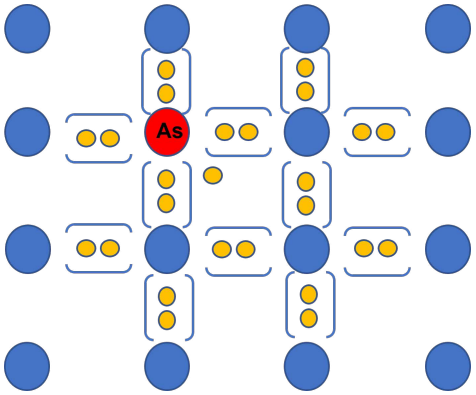

Figure 1.6: Bond scheme of Silicon doped with Arsenic as donor impurity.

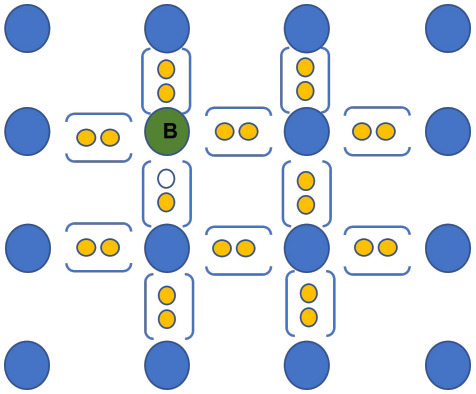

Figure 1.7: Bond scheme of Silicon doped with Boron as acceptor impurity.

$$n_{n0} = \frac{N_D^+(T)}{2}\left[1+\sqrt{1+\left(\frac{2n_i(T)}{N_D^+(T)}\right)^2}\right] \tag{1.14}$$

$$p_{p0} = \frac{N_A^-(T)}{2}\left[1+\sqrt{1+\left(\frac{2n_i(T)}{N_A^-(T)}\right)^2}\right] \tag{1.15}$$

From Fig.1.8 we can see that until a certain temperature T', the semiconductor can be considered as extrinsic, whereas above T', the semiconductor can be assumed as intrinsic. This is true for both the n-type and p-type semiconductors. T' values for Silicon is above 500 K, thus we will assume the density of the majority carriers as the density of the doping atoms, at least at thermal equilibrium ($\simeq$ 300 K).

When an electric field is applied to a semiconductor, the charge carriers start to move inside the semiconductor with a drift velocity:

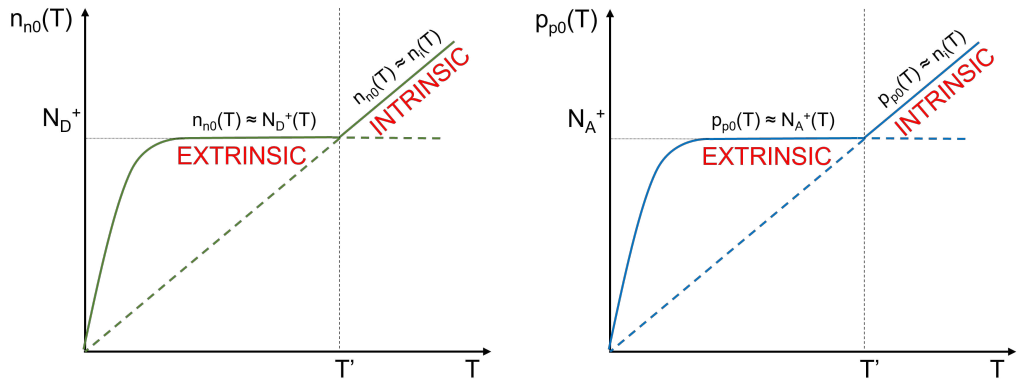

Figure 1.8: Density function of majority carriers in n-type and p-type materials as a function of the temperature

$$\vec{v}_{drift,n} = -\frac{q \times \tau}{m_n^*}\vec{E} = -\mu_n \vec{E} \tag{1.16}$$

$$\vec{v}_{drift,p} = +\frac{q \times \tau}{m_p^*}\vec{E} = +\mu_p \vec{E} \tag{1.17}$$

where q is the electron elementary charge, τ is the time between a collision with the crystal atoms and the other, m^* is the effective mass and μ is the so-called *mobility*, with $\mu_n > \mu_p$ due to the effective mass of the electrons which is smaller than the one of the holes.

The motion of the carriers when subjected to an electric field originates a drift current J_{drift} which is the sum of the contribution of the electrons in conduction band and the holes in valence band:

$$J_{drift} = qn\mu_n E + qp\mu_p E = q(\mu_n n + \mu_p p)E = \sigma E = \frac{1}{\rho}E \tag{1.18}$$

where σ is the so-called *conductivity* and it is the sum of two contributions: σ_n and σ_p, whereas ρ is the so-called *resistivity* and it is the inverse of the conductivity.

When a the carrier concentration is not uniform in the semiconductor, a gradient concentration may occur and this would create a new current that we will call *diffusion current* J_{diff}. This is the result of the effort by the semiconductor to restore a certain uniformity in the concentration. Their equations can be written as:

$$J_{diff,n} = +qD_n \frac{\partial n(x)}{\partial x} \tag{1.19}$$

$$J_{diff,p} = -qD_p \frac{\partial p(x)}{\partial x} \tag{1.20}$$

where the factor $D_{n,p}$ is the diffusion coefficient.

Thus, the total current that we can find inside a semiconductor is the sum of both drift and diffusion contributions:

$$J_n = q\mu_n nE + qD_n \frac{\partial n(x)}{\partial x} \tag{1.21}$$

$$J_p = q\mu_p pE - qD_p \frac{\partial p(x)}{\partial x} \tag{1.22}$$

The diffusion coefficient and the mobility are related through the so-called *Einstein relation*:

$$D_n = \frac{kT}{q}\mu_n \tag{1.23}$$

$$D_p = \frac{kT}{q}\mu_p \tag{1.24}$$

Although the global neutrality is always guaranteed, the local neutrality is not when semiconductors are no longer at equilibrium. The variation of $\rho(x)$ with the electric potential when an electric field is applied is expressed by the *Poisson equation*:

$$\frac{\partial^2 \phi(x)}{\partial x^2} = \frac{\rho(x)}{\epsilon_s} \tag{1.25}$$

where ϵ_s is the *dielectric constant*[4].

The non-local neutrality of the charge means that the charge distributions change in space and time in both CB and VB. The variation of the charge in space and time leads us to define the continuity equations, for electrons and holes:

[4]The dielectric constant, also known as *permittivity* is a measure of the electric polarizability of a dielectric [11] and it is represented by the product of the relative permittivity ϵ_r and the vacuum permittivity ϵ_0

$$\frac{\partial n(x,t)}{\partial t} = +\frac{1}{q}\frac{\partial}{\partial x}J_n(x,t) - U_n \tag{1.26}$$

$$\frac{\partial p(x,t)}{\partial t} = -\frac{1}{q}\frac{\partial}{\partial x}J_p(x,t) - U_p \tag{1.27}$$

where the U_n and U_p factors are the difference between the generation and recombination rates. At equilibrium $U_n = U_n = 0$, while this is no longer true out of equilibrium. Indeed, we could write:

$$U_n = \frac{n_p^{'}}{\tau_n} \tag{1.28}$$

$$U_p = \frac{p_n^{'}}{\tau_p} \tag{1.29}$$

where $n_p^{'}$ and $p_n^{'}$ are the concentrations of the minority carriers at non-equilibrium, while $\tau_{n,p}$ are the lifetime of the carriers.

When a p-type and a n-type semiconductor comes into contact, they give rise to the simplest semiconductor device: a *diode*. The interface between the two semiconductors is called *p-n junction*. Once the two parts come very close together, there is a diffusion process between them, thus the charge carriers start to migrate from a high-concentration to a low-concentration region. As a result an electric field is generated, thus a diffusion current J_{diff}, as discussed in the previous paragraphs. The region at the interface turns into a neutral region, the so-called *depletion region*, due to the recombination of electrons and holes. Electrons, moving from the n side to the p side of the junction as a consequence of the concentration gradient, leave behind a positive charge. Similarly, the holes leave behind a negative charge. These so-called *space charge regions* are placed at the borders of the junction and they generate another electric field, thus another current (drift current J_{drift}) which balances the diffusion phenomenon, as visible in Fig1.9. The results of these two opposite effects is a zero total current flowing through the junction at the equilibrium. In Fig.1.10 a section of a junction can be observed.

At equilibrium, we can conclude that the two electric fields (drift and diffusion) are equal in module but opposite in direction, thus they balance each other resulting in a zero net current flowing through the junction. This internal equilibrium is broken when an external bias is supplied to the junction.

In case of an external bias, two cases may occur:

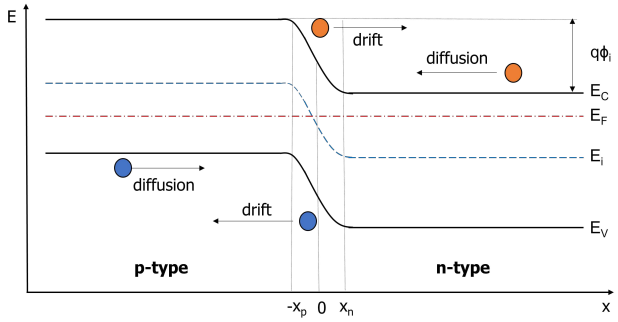

Figure 1.9: Bands diagram of a junction at equilibrium, where the drift and diffusion currents can be observed for electrons and holes.

- Forward bias: a positive bias ($V_a > 0$) is applied, with direction opposite to the built-in potential (ϕ_i) and different magnitude. This increases the diffusion current, generating a non-zero net current. The result is a decrease of the potential barrier in the bands diagram, as visible in Fig.1.11, where the two bands are visibly lower. Therefore, the flow of the diffusion current turns out to be encouraged by a forward bias. The minority carriers inside the junction under the effect of a forward electric field are distributed according the equations:

$$n_p(-x_p) = n_{p_0}(-x_p)e^{\frac{V_a}{V_T}} \tag{1.30}$$

$$p_n(x_n) = p_{n_0}(x_n)e^{-\frac{V_a}{V_T}} \tag{1.31}$$

  which are valid under the assumption that the sides of the junction are much longer than the diffusion length of the minority carriers (L_p, L_n). V_T is the so-called *thermal voltage*, that is a measure of the effect of the boundary on the spatial distribution of the carriers, at fixed temperature.

- Reverse bias: a negative bias ($V_a < 0$) is applied to the junction, resulting in a change of direction of the current, which is be mainly a drift diffusion through the depletion region. Indeed, the n part of the junction is connected to a positive terminal, as well as the p part is connected to a negative terminal. Hence, the majority carriers are attracted toward the terminals and they move away form the junction. Thus, they leave opposite charged-carriers behind, giving rise to a weak drift current flowing through the junction due to minority carriers, the so-called *reverse saturation current*. In Fig.1.12, a bands diagram of the junction under a reverse bias voltage is shown, where an increase

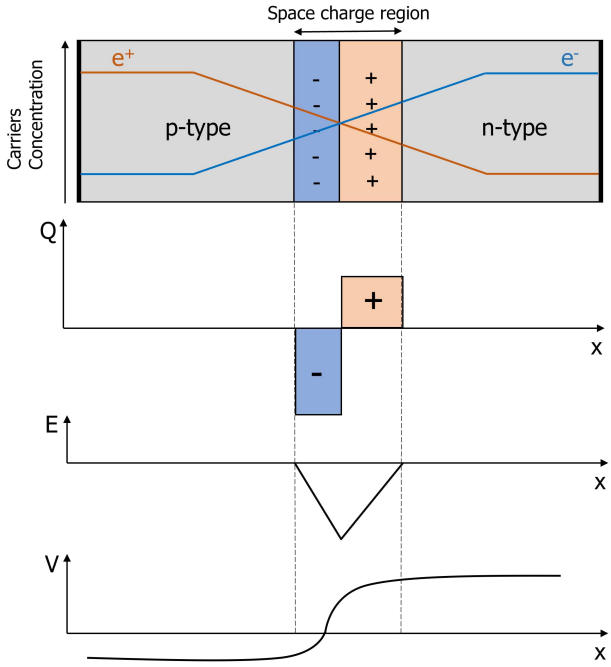

Figure 1.10: Trend of the main parameters in a junction as a function of the space: charge, electric field and voltage

of the barrier can be noticed. The reverse saturation current is not dependent on the bias voltage, indeed it can not increase as a function of the reverse bias, due to the fact that it is thermally generated. Hence, the only effect of the reverse bias on these charge carriers can be to accelerate them towards the p and n sides. This is one of the crucial features of the reverse polarization of a junction. In fact, increasing the reverse bias, the effect on the junction is to accelerate the minority carriers in the depletion region, resulting in an increase of the kinetic energy of the carriers. When reverse bias is close to a certain voltage value (the so-called *breakdown voltage* V_{bd}, the carriers can acquire enough energy to be able to knock off electrons from the silicon atoms in the crystal, through an *impact ionization* process. This phenomenon is called *avalanche* and it can increase the reverse current to very high values. Below the breakdown voltage the avalanche multiplication is limited, thus the multiplication factor takes a finite value, whereas when biased above the breakdown voltage, the avalanche multiplication diverges. Diodes working in such conditions, operate in the so-called *Geiger Mode*.

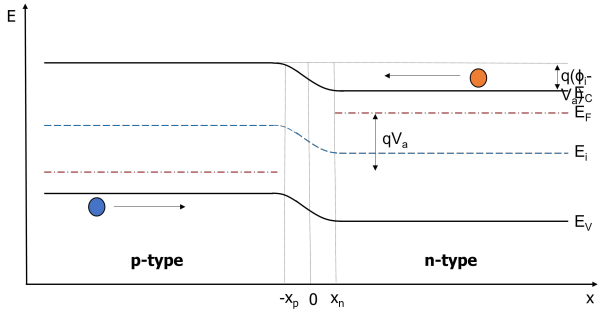

Figure 1.11: Bands diagram of the junction under a forward external bias.

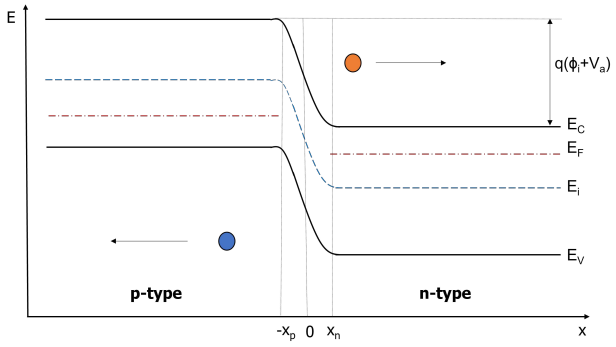

Figure 1.12: Bands diagram of the junction under a reverse external bias.

Overall, the current flowing through a *pn* junction under a forward or reverse bias is given by the *Schottky equation*:

$$I(V_a) = I_0(e^{\frac{V_a}{V_T}} - 1) \tag{1.32}$$

I_0 in the Eq.1.32 is the reverse saturation current:

$$I_0 = qn_i^2\left(\frac{D_n}{L_n N_D} + \frac{D_p}{L_p N_A}\right) \tag{1.33}$$

When in avalanche breakdown, the reverse current $I = MI_0$ is amplified of a factor M:

$$M = \frac{1}{1 - \left(\frac{V_a}{V_{bd}}\right)^n} \tag{1.34}$$

The trend of the current flowing through a junction as function of the polarization voltage can be observed in Fig.1.13, where the three main operating regions are reported.

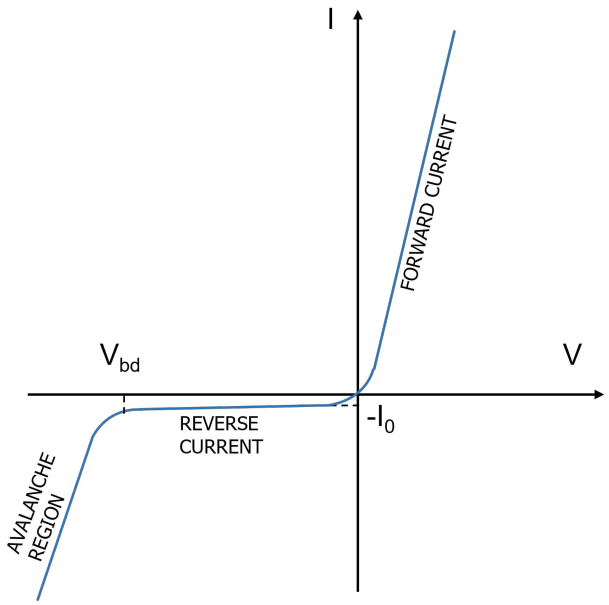

Figure 1.13: I-V plot of a diode where its main operating regions are clearly visible.

1.2 SPADs

A Single Photon Avalanche Diode (SPAD) is a photo-diode, which operates in Geiger mode when biased above the breakdown voltage. A graphical representation of a SPAD is shown in Fig.1.14, where the different regions are visible: substrate, depletion region, high-field region, surface oxyde.

When a SPAD is reverse-biased over the breakdown voltage (Geiger mode), an electric voltage is generated across the depletion region and the depletion region becomes larger as the bias voltage increases. When a photon passes through the depletion region of a SPAD and it is completely absorbed, it creates an electron-hole (e^--h) pair. The high electric field (usually in the order of 10^5 V/cm) accelerates these charged carriers, which obtain sufficient energy to remove an electron from a Silicon atom, through a process called *impact ionization*. From the ionization process, a new (e^--h) pair is created. Then, these secondary charges are accelerated by the electric field, generating new charge pairs, starting a self-sustained avalanche, producing a macroscopic current, detectable by a front-end circuit. Then, the avalanche has to be quenched by active or passive external circuits. The active quenching mechanism uses an integrated circuit with a fast discriminator which detects the avalanche of carriers inside the device. While the bias voltage is reduced below the breakdown voltage, the discriminator provides in output a digital

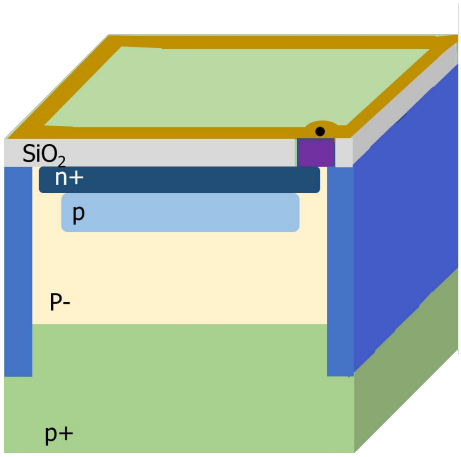

Figure 1.14: SPAD with n-on-p substrate representation with its doping profile.

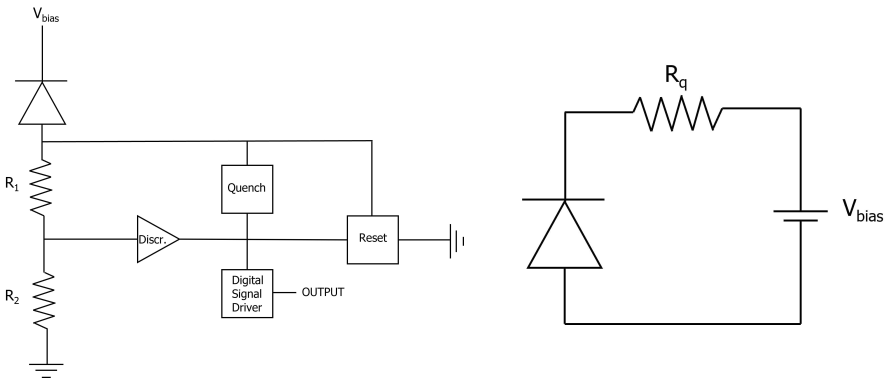

Figure 1.15: Active (left) and passive (right) equivalent circuit schematic view.

pulse for timing applications. After the avalanche has been quenched, the initial bias of the SPAD has to be restored. The passive quenching mechanism uses a simple quenching resistor placed in series with the diode to stop the avalanche and restore the initial conditions, lowering the bias voltage close to the breakdown voltage, through a voltage drop on the resistor, which needs to have a reasonably high value. A schematic view of a circuit for the active and passive quenching mechanisms in a SPAD is visible in Fig.1.15.

The main advantage of using a passive quenching circuit is the more compact structure and the higher fill factor.

The complete electrical equivalent circuit of a SPAD with an integrted passive quenching circuit can be observed in Fig.1.16, including a RC series

circuit with a bias source, a resistor R_s and a diode capacitance C_d. The switch is open at equilibrium, thus no current flows through R_s and the diode capacitance is charged by the bias voltage V_{bias}. When an avalanche triggers the SPAD, the switch gets closed and the diode capacitance discharges through R_s. Capacitance C_d is a parasitic quenching capacitance, which results in a fast current peak at the beginning of the signal when the voltage over the diode drops to the initial conditions [12]. Thus, a SPAD can be approximated to a RC circuit. For this reason, the initial conditions after an avalanche can be restored exponentially with a proper time constant. In particular, the discharge time constant is given by:

$$\tau_d = (R_s||R_q)(C_d + C_q) \simeq R_s(C_d + Cq) \tag{1.35}$$

where the assumption that R_s value is much lower than the quenching resistor R_q was made, which is reasonable considering that R_q has to be high enough to properly quench the avalanche.

Instead, the recharge time constant is given by:

$$\tau_r = R_q(C_d + D_q) \tag{1.36}$$

The gain of a SPAD is the average number of carriers produced during the avalanche and it can be estimated as:

$$G = \frac{Q_{SPAD}}{q} = V_{ov}\frac{(C_d + C_q)}{q} \tag{1.37}$$

where V_{ov} is the over-voltage bias and q sis the elementary electron charge.

1.3 Silicon Photomultiplier

A Silicon Photomultiplier (SiPM) is an array of several passively quenched SPADs, called microcells, operating in Geiger mode, connected in parallel to a common anode and cathode(see Fig.1.17).

SiPM output current is proportional to the number of SPADs fired and, potentially, to the number of impinging photons. An example of output waveform can be observed in Fig.1.18.

The output waveform has two components: a *fast component* due to a fast voltage variation across the parasitic capacitance of the quenching resistance, and a *slow component* due to the SPAD bias recovery, with a current flowing through the quenching resistor. The time constant of this exponential decay is proportional to the quenching resistor and to the cell capacitance, thus it is proportional to the microcell size. Each SPAD within a SiPM is independent

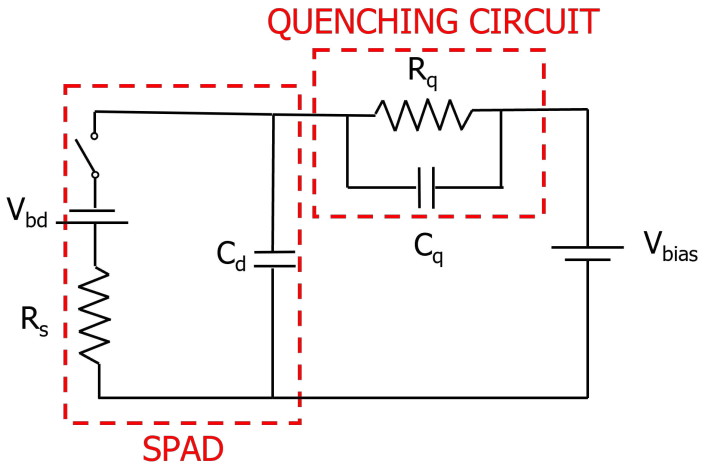

Figure 1.16: SPAD electrical equivalent circuit representation including the parasitic capacitance.

form each other, and the amount of charge collected when fired is the same for every microcell. It has to be pointed out that the charge response of a SiPM to a light input is linear with the number of photons only under the assumption that the number of photons is much lower than the number of SiPM microcells. Otherwise, it can happen that most of the microcells are fired, thus some absorbed photons cannot trigger other avalanches anymore. In this conditions, the SiPM response to the light input is no longer linear. We can call this condition as *saturation*. We can model the number of fired cells, thus the number of the detected photo-electrons, assuming a binomial distribution[14]:

$$N_{p.e.} = N_{cell}\left(1 - e^{-\frac{N_{ph/s} \times t_w \times PDE}{N_{cell}}}\right) \tag{1.38}$$

$$\tag{1.39}$$

where N_{cell} is the total number of microcells, $N_{ph/s}$ is the flux of incident photons, t_{int} is the integration time window, PDE is the so-called *Photon Detection Efficiency*, which takes into account the SPAD efficiency in detecting photons and generate an avalanche as we will discuss later in detail.

1.3.1 Characterization of SiPMs

The performance of a SiPM can be assessed through some key parameters, for example the ability to detect light, the noise and the radiation tolerance.

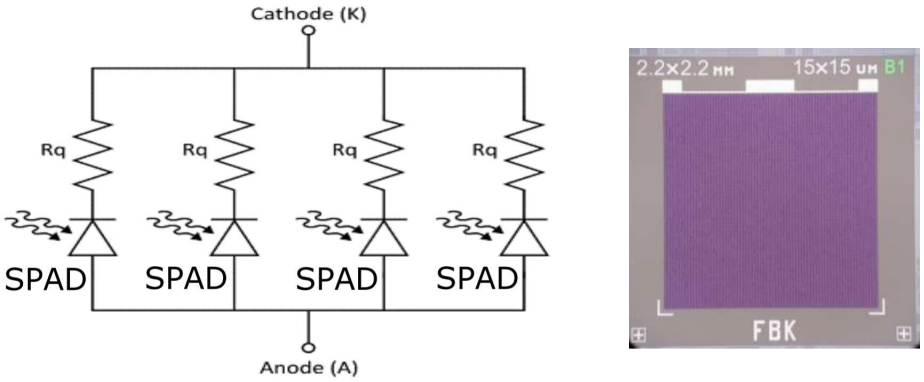

Figure 1.17: SiPM schematic representation as an electric circuit with several SPADs connected in parallel (left) and real picture of a FBK SiPM [13] (right).

All these properties are strongly dependent on the SiPM fabrication process, the silicon substrate, the internal electric field and other design features. In the following, the most relevant ones will be examined in detail.

Reverse Current

One of the first measures usually performed on a SiPM is the reverse current as a function of the bias voltage. In Fig.4.10, a typical reverse I-V curve is showed. Here the main components of the reverse current can be observed. In particular, the breakdown voltage marks the border between the *leakage current* and the *dark current*. The leakage current is considered as the not-multiplied current below the breakdown voltage[12], while the dark current is the multiplication current above the breakdown[15].

Noise

Even in absence of incident photons, we could see a SiPM output signal because of its noise, which has three main contributions:

- **Dark Count Rate (DCR)**: or *Primary noise*, consisting in noise events following an avalanche triggered by thermally generated carriers or by carriers from tunneling in the high-field region. In particular, the thermally generated events follow a Shockley-Read-Hall (SRH) generation-recombination mechanism: carriers are localized in the region between the valence and conduction bands in specific energy states (traps), and the carriers can escape from these traps exchanging

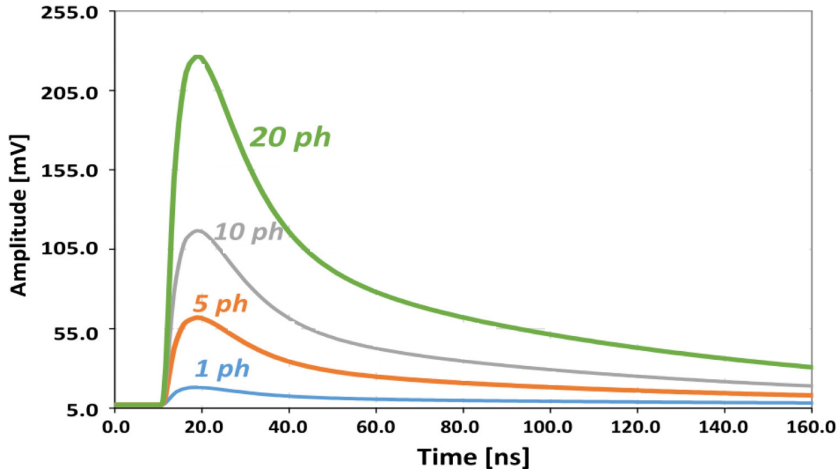

Figure 1.18: Signals from a 3×3 mm^2 SiPM with different number of triggered cells[12].

thermal energy with the crystal through phonons. Thus, this effect is particularly significant at high temperatures. This generation mechanism is strongly dependent on the deep levels concentration inside the epitaxial layer, their activation energy, the thickness of the depleted region and the electric field in the avalanche region[12]. The generation rate of dark count events in the depleted region is given by[16]:

$$G = \frac{n_i}{2 \cdot cosh\left(\frac{E_0 - E_i}{kT}\right)} N_t \sigma v_{th} = \frac{n_i}{\tau_{g0}} \tag{1.40}$$

where n_i is the intrinsic concentration of carriers, E_0 is the Fermi level of the intrinsic material, E_i is the energy level of the generic trap i, N_t is the trapping center concentration, σ is the cross section of the capture process in the traps, v_{th} is the thermal velocity of the carriers and τ_{g0} is the generation lifetime of the carriers in the depletion region. When an electric field is applied to the SiPM, the capture and emission rate of the carriers into the traps is crucially affected by the tunneling and Pool-Frenkel effects introduced by the electric field. Thus, the SRH statistic described in Eq.1.40 becomes[16]:

$$G = \frac{(1 + \Gamma) n_i}{\tau_{g0}} \tag{1.41}$$

where Γ is a field-dependent factor[17]. This is the so-called *field-enhanced SRH* mechanism.

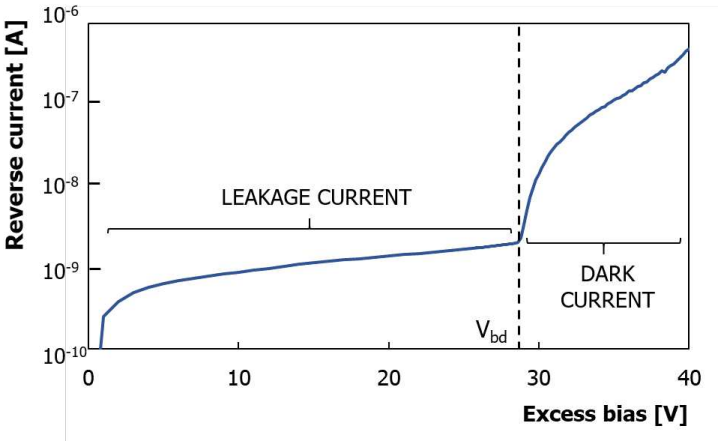

Figure 1.19: Reverse current as a function of the bias voltage, for a 1×1 mm^2 SiPM with 35 μm cell pitch.

At room temperature, in the high-field region, the field-enhanced SRH mechanism is dominant. The band-to-band tunneling effect becomes instead relevant at low temperatures, thus it mainly concerns the SiPMs for cryogenic applications. However, as the tunneling generation becomes dominant with decreasing temperature, the DCR dependence on the temperature tends to reduce[18]. To partially solve this issue, new SiPM designs include an engineered electric field, improving the DCR dependence on the temperature. In Fig.1.20 a graphical comparison between the DCR dependence on the temperature in case of a standard and a low electric field profile can be observed. The dependence on both the band-to-band tunneling and the SRH generation mechanisms are clearly distinguishable.

At room temperature, in the drift region, the SRH generation is the dominant mechanism. Carriers from the drift region reach the high-field region where they can start an avalanche. Then, there are two undepleted regions, one is on top at the interface with the oxyde and the other is the substrate on the bottom. In these regions, the dominant mechanism is the diffusion, which means that the minority charges can diffuse thoward the depleted region and trigger an avalanche[16]. In Fig.1.21, the main generation mechanisms are showed and their spatial localization within the SPAD structure.

- **Cross-talk**: together with the Afterpulsing, it is referred as *correlated noise*, consisting into secondary avalanches due to secondary photons

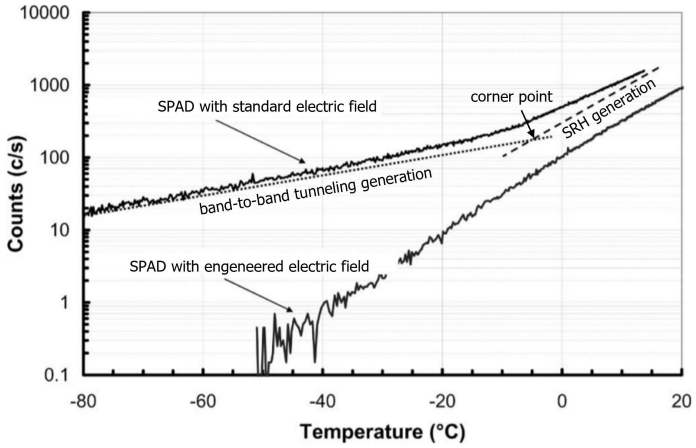

Figure 1.20: Example of DCR plotted as a function of the temperature for a 50-µm SPAD with standard and "engineered" electric field profile[18]

firing cells next to the one of the primary event. It is estimated that the number of secondary photons isotropically emitted during an avalanche is around 3×10^{-5} per avalanche carrier crossing the junction[19, 20]. The resulting output signal is a sum of the primary event and the secondary ones, thus with n secondary events, it will have an amplitude n times higher than the amplitude of a single event.

The cross-talk (CT) can be *direct* (DiCT) (*prompt*), which means that secondary photons trigger an avalanche in a neighbouring cell creating $e^- - h$ pairs directly in its active region, or *delayed* (DeCT), which means that the secondary photons generate e^--h pairs in the bulk of a neighbouring cell. If these carriers diffuse toward the active region, there they can trigger an avalanche with a typical delay of several microseconds or nanoseconds[12].

The probability to have a cross-talk event depends on four factors: the presence of a neighbouring cell, the number of photons emitted during the primary avalanche, the probability that a photon is absorbed in the neighbouring cell and the triggering probability of the photo-generated carriers. The number of emitted photons and the triggering probability are voltage dependent, thus the cross-talk is strictly dependent on the excess bias.

A graphical representation of the cross-talk processes in two neighbouring microcells is represented in Fig.1.22.

The use of deep tranches at the cell borders can help to mitigate the

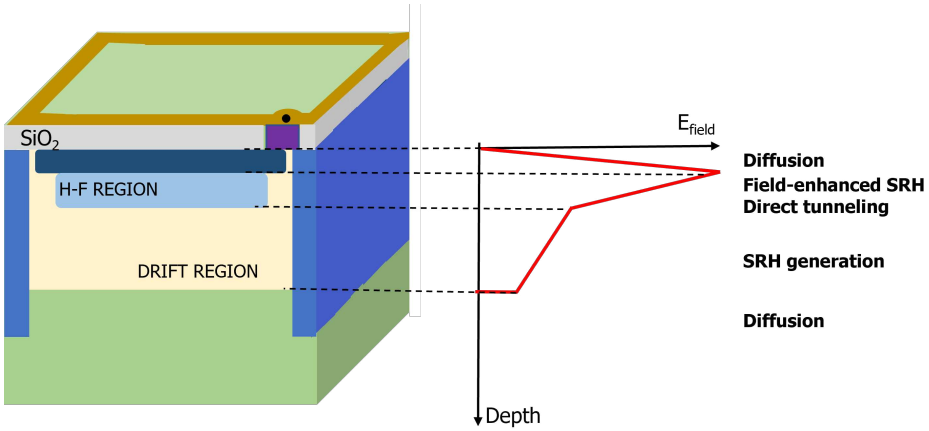

Figure 1.21: Representation of the DCR sources location inside the microcell.

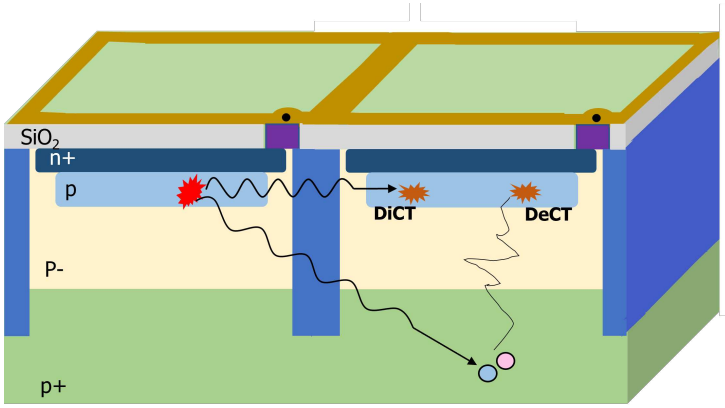

Figure 1.22: Cross-Talk graphical representation in two neighbouring SPADs.

effect of the cross-talk in the SiPM.

The optical cross-talk is usually estimated through the ratio of the count rate at the second photon level and the count rate at the single photon level:

$$CT = \frac{DCR_{1.5p.e.}}{DCR_{0.5p.e.}} \tag{1.42}$$

- **Afterpulsing**: during the avalanche, some of the carriers may be trapped and then released by the several traps within the high field region. Afterpulsing can also be due to secondary photons, re-absorbed in the same microcell. Afterpulsing events happening when the microcell is fully recharged are indistinguishable from the primary dark count

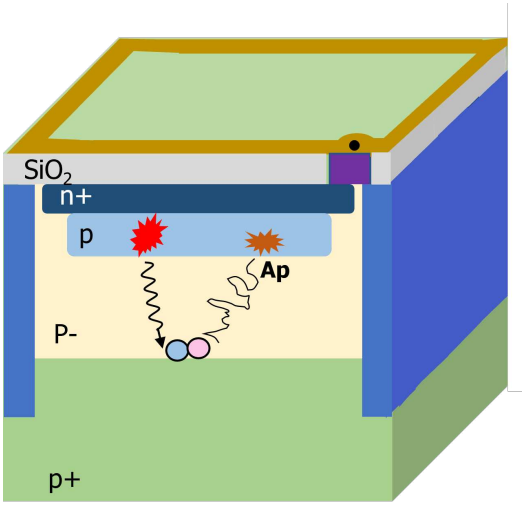

Figure 1.23: Afterpulsing graphical representation in a SPAD.

events. Only when happening during the microcell recharge, they can be distinguished because of their smaller amplitude. They are usually isolated considering that they follow an exponential decay law rather than a poissonian statistics as the dark events.

The main difference between the delayed cross-talk and the afterpulsing is that, this latter happens in the same cell as the primary avalanche, thus neighbouring cells are not involved.

- **Non-linearity (Saturation)**: when a microcell is fired, it remains busy until it is quenched and the bias is restored. This means that during this time (microcell *dead time*), the microcell cannot detect photons.

  As mentioned above in the text, SiPM response to a light input is not linear if the number of incident photons is not much lower than the total number of SPADs. This condition gets worse when noise events happen. Indeed, in this case the microcell dead time increases and the SPAD is kept busy for a longer time.

Fig.1.24 shows a typical signal of a SiPM detected in dark conditions and a schematic view of the events distribution along a pulse-amplitude vs. inter-time plot are visible. As described in [12], this is a very efficient way to discriminate primary events, DeCT, DiCT and afterpulsing through a waveform analysis.

In order to produce such pulse-amplitude vs. inter-time plot, the signal is filtered by a DLED filter[21], which isolates the fast component of the signal

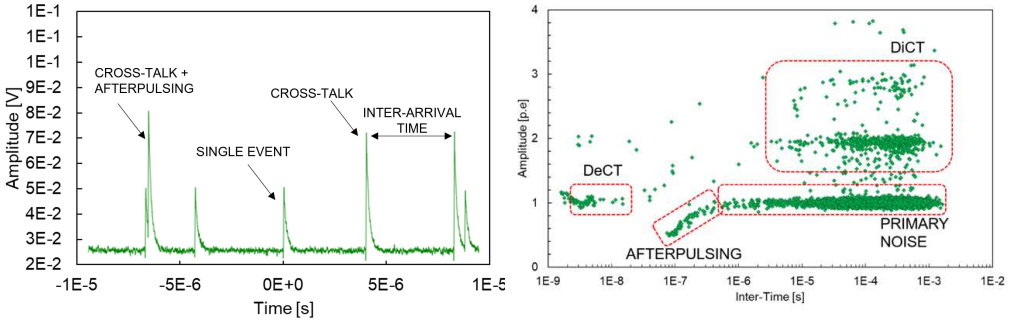

Figure 1.24: Typical noise measure output signals (left) and a schematic view of the main SiPM noise components in an Amplitude vs. inter-arrival time plot: primary noise (DCR), DiCT, DeCT and Afterpulsing (right).

and deletes the slow recharge tail to extract its amplitude. After collecting these parameters, values are plotted as in Fig.1.24 where, depending on the amplitude value, a primary dark event (A=1 p.e.) can be distinguished from a DiCT, which takes higher amplitude values (A_{CT} >1 p.e.). Dark Count Rate (DCR) is estimated from an exponential fit on the events inter-times, considering only the highest inter-times in the plot. DeCT events can be easily recognized from the inter-arrival time distribution, since they typically have a time delay of few ns from the primary event, but they are usually recorded at a minimum inter-arrival time of 1 ns, due to intrinsic limits of this method. Thus, DeCT arriving with t_i <1 ns are recorded as DiCT events. Lastly, the afterpulsing is clearly visible due to its tail at low inter-arrival times.

All the correlated noise components increase the charge collected by a SiPM with respect to the primary photogenerated charge. The cross-talk events increase it by the amount of a single cell triggered by secondary photons, whereas the afterpulsing increases it by a variable quantity depending on the delay of the signal. The contribution of the correlated noise to the total charge collected by a SiPM in quantified by the *Excess Charge Factor* (ECF), which is defined as:

$$ECF = \frac{< Q_{out} >}{< Q_{DCR} >} = \frac{I_{dark} - I_{leak}}{I_{DCR}} = \frac{I_{dark} - I_{leak}}{q \times G \times DCR} \tag{1.43}$$

where Q_{out} is the average charge collected by the SiPM, the I_{dark} is the SiPM output current in dark conditions and G is the SiPM gain.

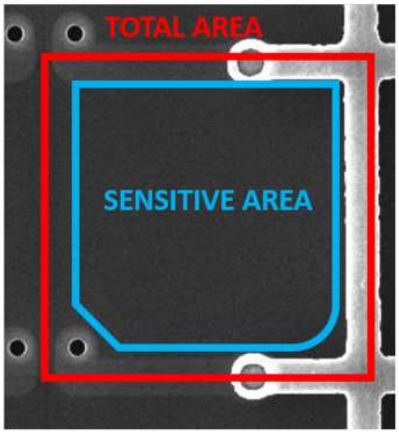

Figure 1.25: Real picture of a SPAD, where the active and the geometrical areas are clearly distinguishable.

Photon Detection Efficiency

Photon Detection Efficiency (PDE) represents the probability of a photon to be absorbed and trigger a self-sustaining avalanche into a SiPM cell, providing an output signal. It can be estimated as:

$$PDE = \frac{N_L - N_D}{N_{ph}} \tag{1.44}$$

where N_L is the number of detected events in light conditions in a certain time window, N_D is the number of events detected in dark conditions in the same time window, and N_{ph} is the total number of incident photons.

PDE is the combination of several factors:

$$PDE(V, \lambda) = FF \times QE(\lambda) \times T_p(V, \lambda) \tag{1.45}$$

where FF is the *Fill Factor*, which is the ratio between the active area and the total geometrical area of the SPAD, QE is the *Quantum Efficiency*, which represents the probability for a photon with a certain wavelength λ to be absorbed into the active volume of the SPAD. T_p is the so-called *Triggering Probability*, which represents the probability for an e^--h pair to trigger a self-sustaining avalanche within a SPAD biased to a certain voltage V.

The FF factor is a geometrical factor, thus it is theoretically independent on the bias voltage applied to the junction. As visible in Fig.1.25, the active area is defined by a doping implant in the microcell which marks the high electric field region of the p-n junction. Fig.1.26 shows a TCAD simulation of the distribution of the electric field within a SPAD, where the electric

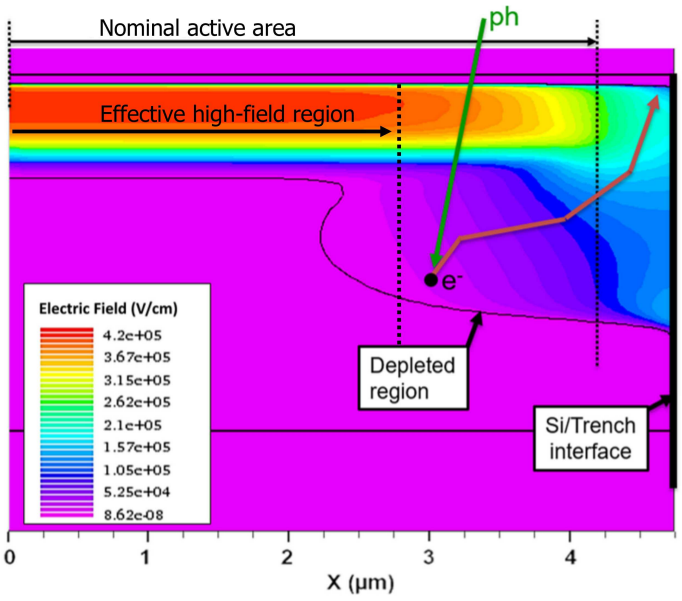

Figure 1.26: TCAD simulation of a SPAD showing the electris field distribution into the microcell. The difference between the nominal and effective active area is also visible[22].

field appears fairly smoothed on the edges. Thus, the effective active area of the cell is smaller than the nominal one estimated from the layout, which instead takes into account a uniform electric field. This is the so-called *Border effect*[23].

In Fig.1.27, the triggering probability is simulated and plotted as a function of the depth, for electrons and holes[24]. The dependence of the combined triggering probability P_P on the probability of triggering an avalanche of the electrons P_e and the holes P_h is given by the equation:

$$P_P(x,V) = \Big(P_e(x,V) + P_h(x,V) - P_e(x,V)P_h(x,V)\Big) \tag{1.46}$$

where all the variables are strictly dependent on the depth and the bias voltage (thus, the electric field). In particular, the variation of triggering probabilities of the two carriers with the depth is given by:

$$\frac{dP_e(x)}{dx} = (1 - P_e(x))\alpha_e[P_e(x) + P_h(x) - P_(x)P_h(x)] \tag{1.47}$$

$$\frac{dP_h(x)}{dx} = (1 - P_h(x))\alpha_h[P_e(x) + P_h(x) - P_(x)P_h(x)] \tag{1.48}$$

where α_e and α_h represent the impact-ionization-coefficients of electrons and holes in silicon, respectively At the borders of the depletion region (x=d_P,

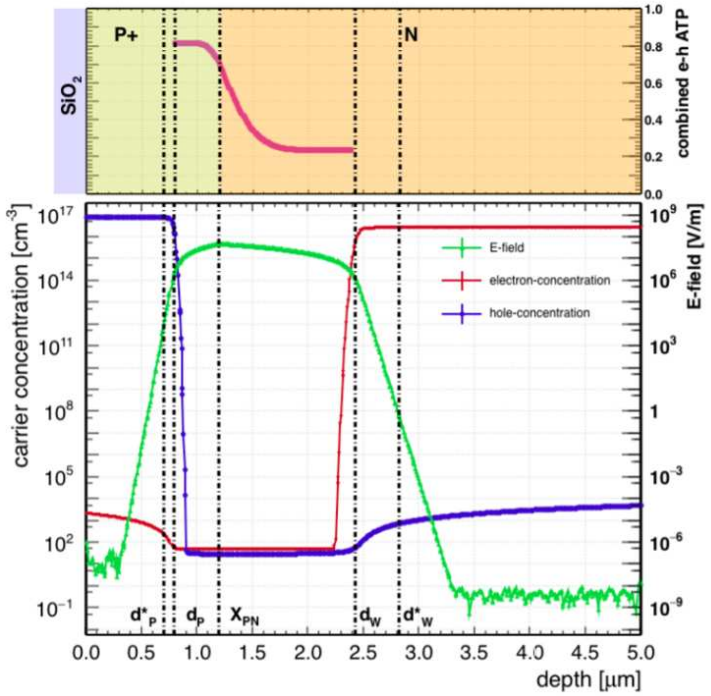

Figure 1.27: Top: combined triggering e$^-$-h probability as a function of the width. Bottom: Single carrier concentration and electric field as a function of the width. Here the borders of the depletion region are clearly identified, with also the edges of the effective photon collection region d_P^* and d_W^*, while x_{PN} represents the highest electric field value[27].

x=d_W]), P_e and P_h are dominant respectively[25, 26]. In the middle of the depletion region (x∈[d_P,d_W]), the probability of an electron to trigger an avalanche is higher than the holes, due to the higher impact-ionization-coefficient α. If the photon is absorbed outside the depletion region, the generated carriers drift (or diffuse) through the depletion region, where they may start an avalanche.

Breakdown Voltage

The breakdown voltage V_{bd} of a SPAD or a SiPM is the minimum voltage value required by the electric field to create a self-sustaining avalanche within a SPAD.

The breakdown voltage is strictly dependent on the electric field inside the microcell, thus on its doping profile. It is also dependent on the temperature due to variations in carrier mobility and ionization rates[28],

When not specified, the default method to estimate the breakdown voltage in this work will consider the voltage value corresponding to the maximum of the second logarithmic derivative of the reverse I-V curve.

Gain

The Gain of a microcell can be defined as the charge produced for each triggered avalanche. The microcell gain does not take into account the correlated noise. In fact, it represents the charge produced by one primary event in one triggered microcell. The SiPM gain is usually the same for each microcell, and it typically ranges between 10^5 and 10^9[29, 30]. It is defined as:

$$G = \frac{Q_{cell}}{q} = \frac{(V - V_{bd})(C_d + C_q)}{q} \tag{1.49}$$

where Q_{cell} is the collected charge from the avalanche to the cell electrode, q is the electron elementary charge, C_d and C_q were described above and visible in Fig.1.16. The dependence on the breakdown voltage is a factor especially in unstable thermal conditions, due to the breakdown voltage dependence on the temperature. Indeed, at fixed bias, the gain can be affected by temperature variations, thus breakdown voltage changes must be considered to get an accurate measure of the gain.

From the SiPM gain, another parameter can be derived: the *Current Gain*, which is given by:

$$G_c = G \times ECF \tag{1.50}$$

As a first approximation, the current gain identifies the overall charge produced by one triggered microcell, taking into account all the correlated avalanches produced per each primary event.

ENF

Excess Noise Factor (ENF) takes into account all the uncertainties connected to all the SiPM parameters estimated through statistical methods.

For instance, in the Gain section above, we introduced an hypothetical correlation between the number of detected photons and the collected charge. This holds true under the assumption to neglect the correlated noise which may affect the output charge. This effect is usually taken into consideration in the ENF, as well as other similar effects related to other parameters.

SiPM main parameters are usually estimated assuming the events having a certain probability distribution. In the analysis of the performance of a SiPM, noise and non-linearity factors must be taken into account. In particular, non-linearity has been already discussed in Sec.1.3.

Under the assumption of a random variable M with a Poissonian statistic in input, the ENF can be defined as[31]:

$$ENF = 1 + \frac{\sigma_M^2}{\mu_M^2} \tag{1.51}$$

where σ_M^2 and μ_M represent the variance and the mean of the random variable, respectively. Through Eq.1.51, the ENF components related to each Poissonian-like parameter can be estimated.

In SiPMs when coupled to scintillators to perform energy measurements, the total ENF, taking into account all the possible excess noise factors, can be calculated as[31]:

$$ENF_{SiPM} = ENF_{PDE} \cdot ENF_{DCR} \cdot ENF_{gain} \cdot ENF_{Corr} \cdot ENF_{n-lin} \tag{1.52}$$

The several contributions are given by:

- ENF_{PDE} is the excess noise related to the conversion of the photons in photo-electrons and then in Geiger counts[31], considered as random processes. Assuming a Poissonian photons distribution, it is given by:

$$END_{PDE} = \frac{1}{PDE} \tag{1.53}$$

- ENF_{DCR} is obtained assuming dark electron generation as a Poissonian process:

$$ENF_{DCR} = 1 + \frac{DCR \times t_{int}}{N_{ph} \times PDE} \tag{1.54}$$

  where t is the integration time window of the signal and N_{ph} is the number of photons incident in the same integration window

- ENF_{gain} is due to the output number of electrons produced in the multiplication process but it usually takes negligible values.

- ENF_{Corr} is the excess noise contribution form the correlation noise:

$$ENF_{Corr} = \frac{1}{1 - (1 - P_{corr})} \tag{1.55}$$

  where P_{corr} is the probability of having a correlation noise event

- ENF_{n-lin} is the ENF contribution form the non linearity of a SiPM. Assuming the SiPM microcells having a certain recovery time τ and an exponential pixel recovery, the ENF_{n-lin} factor can be estimated as:

$$ENF_{n-lin} = \frac{\left(1 + \frac{\mu_{ph} \times PDE}{N_{cells}} \frac{\tau}{t_{int}}\right)^2}{1 + \frac{\mu_{ph} \times PDE}{2 \times N_{cells}} \frac{\tau}{t_{int}}} \tag{1.56}$$

Activation Energy

The activation energy E_a of the noise in a SiPMs is given by the DCR or current dependence on the temperature. The several DCR generation mechanisms discussed in detail above show an exponential dependence on 1/T, thus their dependence on the temperature can be described by an Arrhenius-like trend:

$$G(T) \sim DCR(T) \sim e^{-\frac{E_a}{kT}} \tag{1.57}$$

where E_a is the activation energy of a specific generation process. As already mentioned, the DCR has several generation mechanisms, thus several activation energies to extract, depending on the temperature range. Fig.1.28 provides a graphical representation of three generation processes in three temperature ranges: diffusion, SRH and tunneling. In the diffusion region, the activation energy corresponds to the value of the band-gap energy (E_a = 1.21 eV in Silicon). In the SRH region, the activation energy is in the order of half of the bend-gap energy (E_a = 0.56 eV in Silicon). While in the previous regions the relation between a specific DCR generation mechanism and the temperature was well-defined, in the tunneling region the process dependence on the temperature is strictly related to the electric field design.

Emission Microscopy

Emission Microscopy (EMMI) is a technique to obtain an image of the secondary photons produced during the avalanches in the SiPM microcells.

In literature, several explanation to this phenomenon were suggested: from radiative transitions of the carriers due to local heating[32], to microplasmas (localized regions with a large carrier density)[33], or Bremsstrahlung radiation[34]. EMMI is based on imaging of "hot carrier luminescence" (HCL), which is due to accelerated carriers suddenly losing their energy in high electric field regions. In SPADs and SiPMs the emission of secondary photons happens during the avalanche multiplication process.

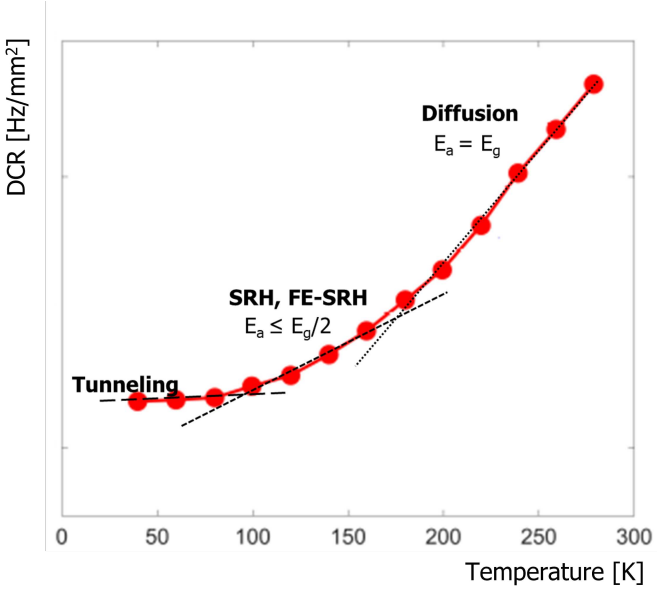

Figure 1.28: Activation energy along the three main DCR generation process in a p-on-n SiPM: Tunneling, Diffusion and Shockley-Read-Hall (SRH) with and without field enhancement.

The measurement setup consists of a scientif-grade cooled camera placed on a SiPM which takes a picture of the device biased over the breakdown voltage in dark conditions. The main purpose of this measure is to observe the emission spots and assess the uniformity of their distribution inside the SPAD or, more widely, over the SiPM area.

1.4 FBK SiPM technologies

FBK starts the production of SiPMs in 2005[35]. The first SiPM prototype consisted in a $1 \times 1\ mm^2$ structure with a n-on-p junction[36]. The cell size was 40 μm, the breakdown voltage was about 30 V, the PDE peak ($\sim 14\%$) was at around 420 nm, the DCR was of the order of 2-3 MHz at 3 V excess bias and the gain was 10^6 at the same excess bias.

FBK SiPM performance has improved over this time, to make SiPMs the detectors of choice for many applications: from high-energy physics, to PET or automotive LiDAR.

In the following some of the most promising FBK technologies are analyzed in detail.

1.4.1 NUV technology

NUV technology is what is called "p-on-n junction" which has its peak in the PDE spectrum at around 420 nm, thus in the NUV-blue region of the visible spectrum. Developed in FBK for the first time in 2012, it was designed as a n-doped substrate below a p-doped shallow implant with a 40 μm cell pitch and a 30% PDE at 420 nm at 4 V excess bias[37, 38]. The substrate was then improved to reduce the delayed noise. Fig.1.29 shows the doping profile of a typical NUV standard technology: there are two implants, a shallow (SI) and a deep (DI) ones, providing a $p^+/n/n^-/n^+$ structure. The p^+/n junction generates, when depleted, the high-field region, where the electric field reaches its peak and avalanche carrier multiplication takes place. In this doping configuration, carriers from photons in the blue region of the light spectrum are photo-generated close to the surface, due to the short wavelength of the photons. Thus, the electrons triggers the avalanche and they are responsible for the fast increase of the PDE with the over-voltage, due to their higher ionization coefficient, which results in an high triggering probability. Holes can trigger the avalanche drifting from below to the high-field region.

1.4.2 RGB technology

RGB technology consists in a n-on-p structure, with a p-doped substrate , as visible in Fig.1.29. The peculiarity of this technology is the PDE peak at around 525 nm, thus in the visible part of the light spectrum. This is due to the fact that electrons, coming from below, have to drift toward the high-field region to trigger an avalanche. On the other hand, holes may trigger an avalanche coming from above to the high-field region and, since they present a lower ionization coefficient, this result in a lower triggering probability than a NUV technology (see Fig.1.30).

RGB technology, as well as the NUV technology, has undergone some improvements over the years, with the introduction of the RGB-HD, RGB-UHD and RGB-HD-LF technologies. These upgrades will not be mentioned here, since a detailed discussion can be found in the NUV technology section.

Another improvement of the RGB-HD tachnology consists into the RGB-HDEnhanced border technology, which is developed introducing an implant ring to increase the electric field on the borders of the microcell. As a consequence, this allows to obtain an actual fill factor value close to the nominal one and to reduce possible border effects.

1.4.3 VUV technology

Vacuum Ultraviolet (VUV) technology stems from the need to detect light at very small wavelengths, especially for scientific experiments using liquid Xenon as a scintillator. The standard NUV and RGB technologies showed a very low PDE under 300 nm, thus a new technology was introduced in 2018. The main issue with the standard technologies lies in their surface design. Indeed, differently form the visible light, VUV photons have a very short penetration depth into the Silicon . This results in a complete absorption of the VUV photons in the neutral region close to the surface, thus in a very low PDE. The main innovation of the VUV is the modification of the Anti-Reflective Coating (ARC) on top of the active area, to avoid the absorption of VUV in the dielectric layers, preserving a good passivation quality, which led to a PDE value higher than 20% at 175 nm[39].

1.4.4 NIR technology

Near Infra-Red (NIR) SiPM technology arises from the need to detect photons with large wavelengths. Indeed, if for the VUV photons the main issue was the early absorption in the neutral region close to the surface, in the NIR technology the main problem is the high penetration depth of the photons, which makes their detection very challenging. Indeed, they are usually absorbed in the substrate and their chance of triggering an avalanche is extremely low. The solution was found in an increase of the epitaxial layer, i.e. the sensitive layer of the SiPM as a first approximation, and as a consequence an increase of the quantum efficiency of the SiPM. A deeper trench among the microcells was also introduced to implement proper isolation of microcells. The main limiting factor of this new approach is represented by the uncollected charge on the microcell borders under the junction due to the presence of a depleted region starting from the deep trenches and generated by the charge induced by the oxide charge. Thus, the carriers drift toward the borders rather than vertically. Nevertheless, many experiments need to use SiPMs with small cell pitch due to their faster cell recharge and low noise. In this case the border effects have a much higher impact on the performance of the SiPM[39].

Overall, the NIR technology produced very positive results in detecting NIR photons, showing a PDE of 18% at 850 nm and 12% at 900 nm[**?**].

1.4.5 HD technology

One of the most important improvements to the SiPM design over the years was the high-density (HD) technology which is based on the introduction of deep trenches between neighbouring cells to reduce the correlated noise[40]. While in the NUV technology the electrical separation between adjacent cells was obtained through n-stop, it had no effect in optical isolation. In the HD technologies, FBK employed a deep trench isolation to electrically and optically separate the cells. On the other hand, the trench may create an edge breakdown, thus it must be spaced a few microns form the n implant. Thanks to the deep trenches and the higher fill factor, it was possible to obtain smaller cell sizes, increasing the number of microcells per unit of area of the SiPM, thus increasing its dynamic range.

1.4.6 UHD technology

A further improvement in the reduction of the SPADs cell size is the ultra-high-field (UHD) technology. This enables the SiPM to have a smaller dead border for each SPAD and an higher dynamic range (about 45000 cells per mm^2), due to the smaller cell size up to 5 μm [41]. The increase of the dynamic range results in an increase of the PDE. These results were achieved through a design improvement: cells with circular active area were introduced, while contact size and resistor width were reduced and distance of active area from trench was further reduced compared to the standard HD.

1.4.7 NUV-HD-cryo (LF) technology

As discussed in the DCR paragraph, at very low temperature, the DCR in a SiPM looses its strong dependence on the temperature, in particular when the tunneling generation mechanism dominates over the other generation processes. We already mentioned the possibility to engineer the electric field to overcome this issue at low temperature. From the attempt to engineer the electric field for this purpose, the NUV-HD-cryo technology was introduced by FBK in 2017[42]. The most innovative design improvement of the NUV-HD-cryo technology consisted in a lower electric field peak at breakdown, obtained through some modifications of the junction.

1.4.8 NUV-HD-RH

Among the NUV-HD technologies, one of the latest releases in FBK is the NUV-HD-RH, specifically designed to improve SiPMs radiation hardness,

using a lower electric field to enhance the dependence of the DCR on the temperature, a higher fill factor resulting in a higher PDE and small cells (12.5-15-20 μm so far) to obtain a lower correlated noise, a lower power consumption, a smaller cell occupancy and low saturation effects.

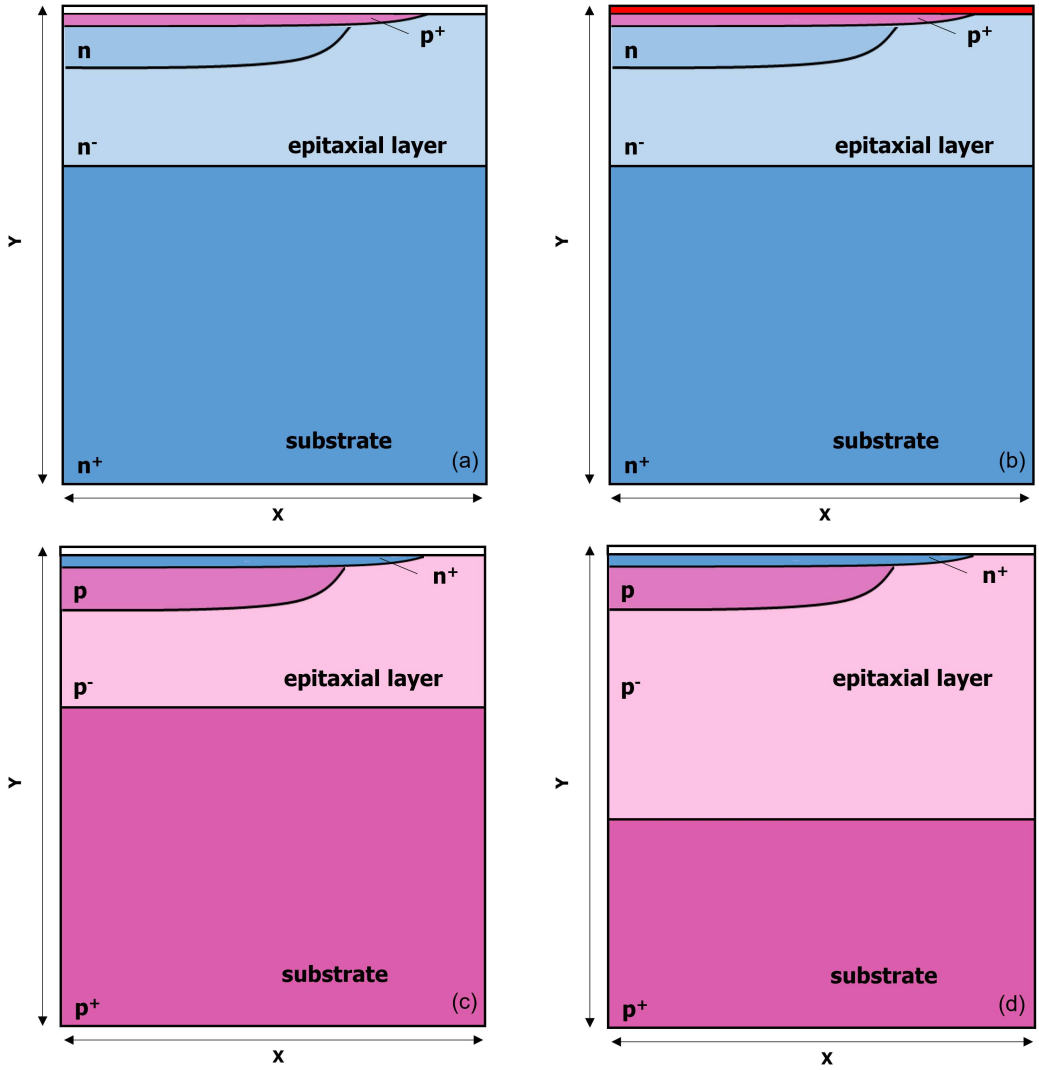

Figure 1.29: NUV(a), VUV(b), RGB(c) and NIR(d) technologies doping profile sections.

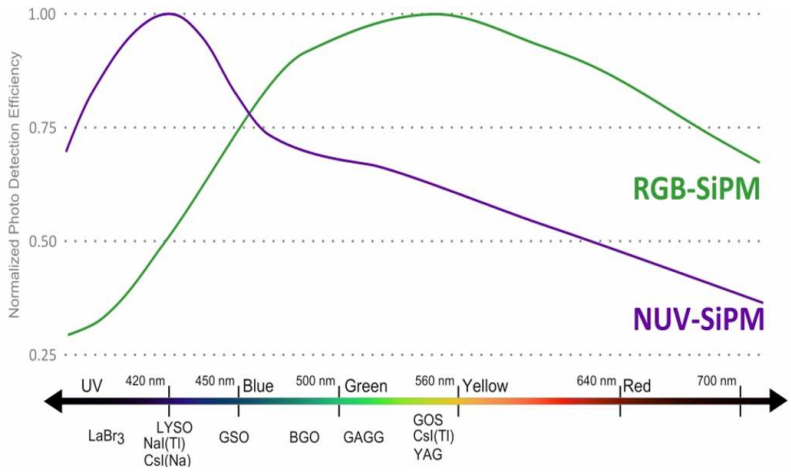

Figure 1.30: PDE plot for NUV and RGB technologies. NUV (blue line) has a fast increase and an higher peak, while RGB (orange line) presents a late increase and lower peak, due to the lower ionization factors of the holes, which are the main responsible for the avalanche triggering in the RGB technology.

Chapter 2

Radiation Damage

2.1 SiPM in HEP

The first detector to explore the use of SiPMs in a physics experiment was the CALICE Analog Hadron Calorimeter (AHCAL) experiment which included 7608 photon sensors. The high resolution was one of their main assets especially in calorimetry, since bn each channel could be monitored individually. In Fig.2.1 an example of a AHCAL SiPM response to a low-intensity light is shown[43], where each peak corresponds to a fired microcell, i.e. to a single detectoede photon (neglecting for the moment the correlated noise), as a result of the sensor resolution.

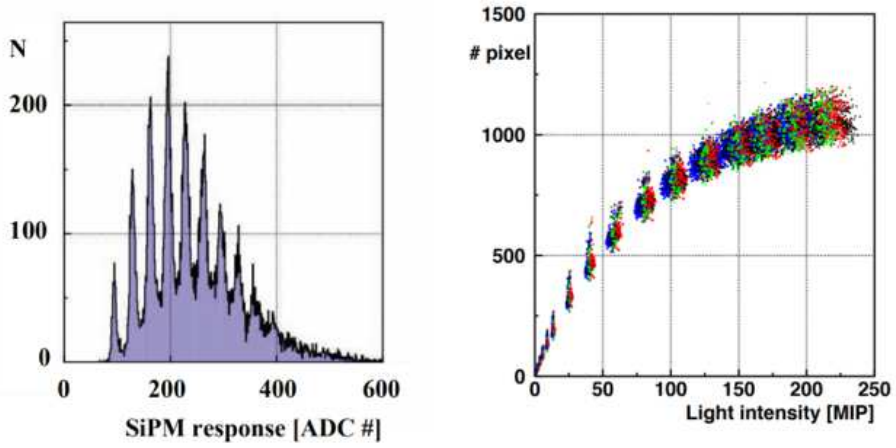

Figure 2.1: AHCAL SiPM spectrum for low-intensity light (left) where each peak corresponds to a fired pixel. Number of fired pixel as a function of the intensity light (right).

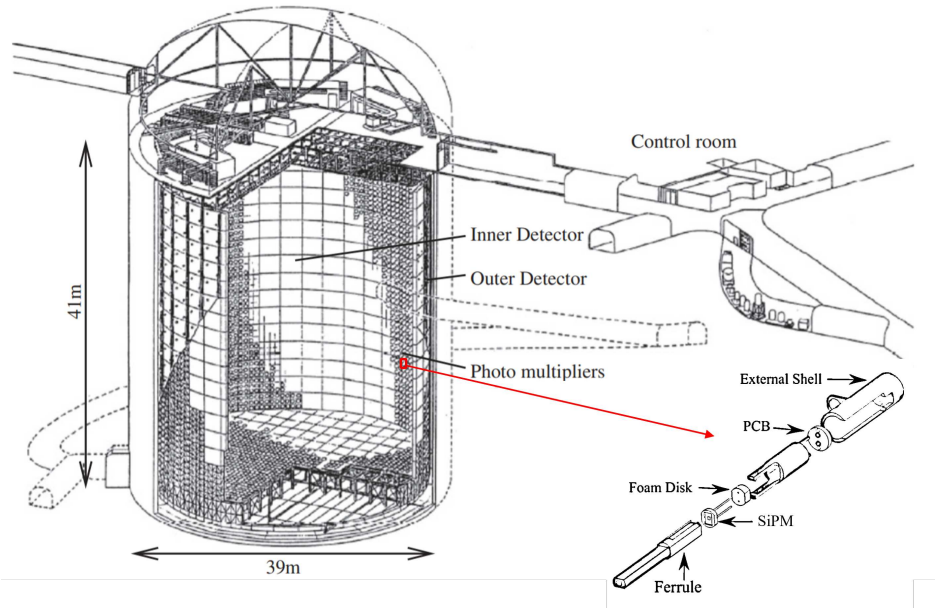

Figure 2.2: Super-Kamiokande Detector. Inner and the outer detectors are optically separated by SiPMs which set the boundary between the two detectors[44, 45].

In 2010, T2K was the first particle physics experiment to use SiPMs on a large scale with 56000 sensors in total (Fig.2.2). In both experiments, SiPMs were used to read out scintillation light from plastic scintillators. Light was collected through wavelength-shifting fibers into the scintillators and then it was guided toward the SiPMs, connected to an ASIC-based front-end electronics[45]. A zoomed view of this latter architecture in the T2K experiment is visible in Fig.2.2.

The previous examples can be used as starting point to understand the importance of using SiPMs-based detectors to detect particles. On the other hand, this is not always feasible, due to the high radiation tolerance required for such experiments. Indeed, radiation damage represents the main limit to the use of SiPMs in several applications, from space to High-Energy Physics (HEP).

This work is focused on the test of the radiation tolerance of several FBK SiPM technologies, focusing on the investigation on the main damage mechanisms in such detectors.

Although radiation damage of silicon sensors is one of the most important topics in HEP, only a few literature about radiation damage deals with SiPMs. For this reason, almost all the models and literature mentioned in this chapter will be referred to a generic silicon sensor and then adapted to

SiPMs at the measurement stage.

2.2 Radiation-Matter Interaction

When radiation comes into contact with matter, several effects may arise from the interaction. Depending on the target, but mainly on the characteristics of the incident particles, the radiation may be absorbed, scattered or can pass through the target with no interaction at all. The radiation-matter interaction is usually described in terms of particle-matter interaction. Thus, for a complete understanding of the main interaction effects, it can be useful to describe the main interaction mechanisms of different particles.

2.2.1 Proton-Matter Interaction

Inelastic Coulomb Scattering with electrons

When a proton comes into contact with an atom, one of the main interaction mechanisms is given by the Coulomb interaction between the incident proton and the electrons of the target atom. During the interaction, the energy loss from the proton is exchanged with the atomic electrons . The energy loss per unit of distance along the proton path is given by the so-called *Bethe Formula*:

$$-\frac{dE}{dx} = 4\pi\frac{N_A Z\rho}{A} r_e^2 m_e c^2 \frac{z^2}{\beta^2}\left(ln\frac{2m_e c^2\beta^2\gamma^2}{I} - \beta^2 - \frac{\delta(\gamma)}{2}\right) \tag{2.1}$$

where N_A is the Avogadro number, ρ is the density of the material, m_e is the electron mass, r_e is the classical electron radius, I is the *ionization potential* that is the minimum energy required to extract an electron form its atomic structure, β is the ratio between the velocity of the particle and the one of the light in vacuum, γ is a factor know as *Lorentz factor*:

$$\gamma = \frac{1}{\sqrt{1-\beta^2}} \tag{2.2}$$

Lorentz factor takes into account the variation of the physical quantities of an object like velocity, time or length when this object is moving. Lastly, the $\delta(\gamma)$ in eq.2.1 is a factor considering the density effects in the case of high γ, thus when the velocity of the particle is close to c.

Eq.2.1 is valid only for heavy charged particles, thus it cannot be applied to electrons. The main reasons for this is that its derivation assumes that

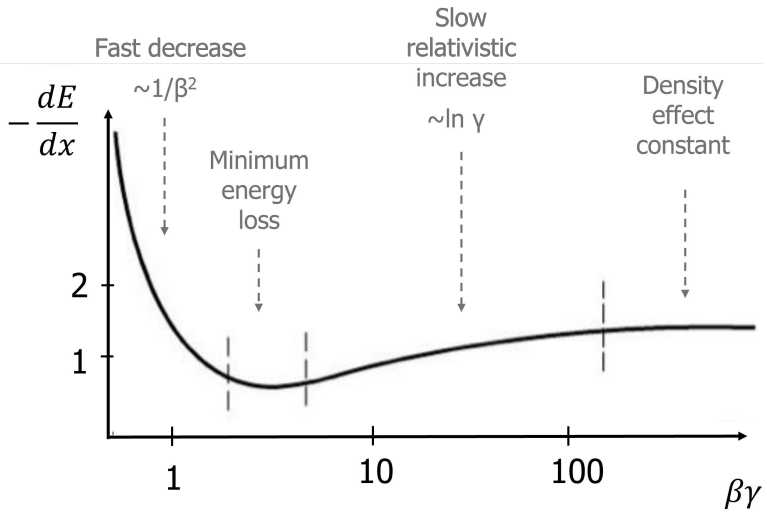

Figure 2.3: Bethe-Bloch function as a function of the particle momentum. Four different trends can be distinguished along the curve, each due to a particular effect and each related to specific parameters of the Bethe formula.

the incident particle is basically undeflected. During the interactions, the incident particle acquires a transverse component of momentum per collision approximately equal to that given to an electron in the absorber. Thus, assuming the incident particle having a mass M >> m_e, this momentum can be neglected, while if the incident particle is an electron, the transverse velocity corresponding to this momentum will not be negligible anymore. Furthermore, when two identical particles interact with each other, additional quantum effects must be taken into account.

Eq.2.1 tells us some interesting things about the ionization mechanism from a heavy charged particle, as visible in Fig.2.3:

- The energy loss is dependent on the material properties through the factor Z/A, where Z is the atomic number and A is the mass number. Since Z/A corresponds to approximately 1/2 for each element except the hydrogen, this factor can be assumed as a constant. Thus, the energy loss can be assumed independent on the material

- The minimum energy loss value is strictly dependent on the factor I, thus on the material properties. The particles at their minimum energy loss value are called MIP (Minimum Ionizing Particles)

- The energy loss is proportional to the charge of the particle z. Thus, an α-particle looses more energy than a proton in the same conditions

- the incident particle mass is included only in the $\beta\gamma$ factor, thus when plotted as a function of $\beta\gamma$ as in Fig.2.3, the trend of the energy loss curve is independent on the particle mass

Elastic Coulomb Scattering

When a charged particle interacts with the Coulomb field of a nucleus, this results in a deflection of the motion of the particle from the initial path. Assuming the nucleus heavier than the incident particle, the center of mass of the system can be considered at the nucleus. The cross-section for the scattering of the incident particle at an angle θ in a range dθ (Rutherford Scattering) is defined as the ratio between the number of particles scattered into the solid angle dΩ per unit of time and the total intensity of incident particles:

$$\frac{d\sigma}{d\Omega} = \frac{1}{4\pi\epsilon_0}\left(\frac{Ze}{2mc^2}\right)^2 csc^4(\theta/2) \tag{2.3}$$

where m is the rest mass of the particle, e is the elementary mass, θ is the scattering angle and Z is the charge number of the target material.

If the energy exchanged during the interaction is higher than the energy required to remove the target atom from its position (minimum defect energy), the atom can be displaced during the process. This can be a single event or the incident proton after a first interaction might still have enough energy for further interactions. The defect density created by a single proton can be estimated as[46]:

$$\rho_d = N\sigma n \tag{2.4}$$

where N is the atomic density (atoms/cm^3), n is the number of defect generated by a single event and σ is the event cross section.

Non-elastic Nuclear Interaction

The non-elastic interactions between the proton and the nucleus of a target material are the dominant effect at high energies. When the incident proton collides with the target nucleus, this latter experiences a spallation process which causes its break-up. The result is the generation of several nucleons which are emitted in the same direction of the incident proton, leaving the residual nucleus in an excited state.

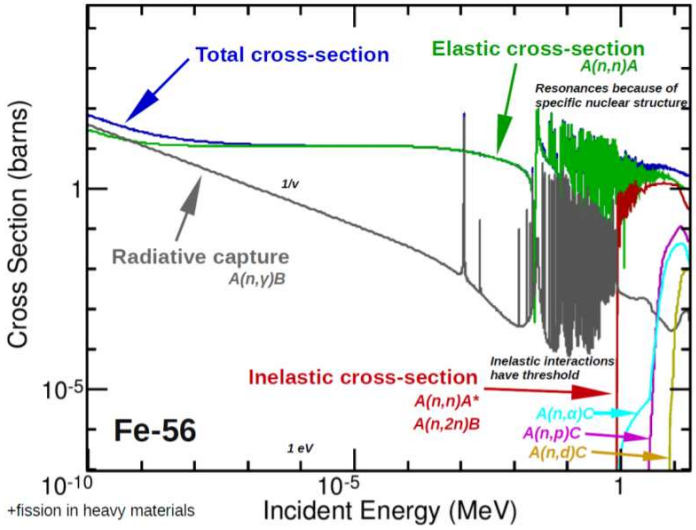

Figure 2.4: Cross section of neutrons in Fe^{56}[47].

2.2.2 Neutron-Matter Interaction

Neutrons show a slightly different behavior than protons, due to the fact that they does not have an electric charge. In particular, depending on their energy, they interact differently with the target nucleus. A graphic overview of the different cross sections of the neutrons as a function of the incident particle energy in Fe^{56} is visible in Fig.2.4.

$E_n >$ 10 MeV

Neutrons with energy above 10 MeV colliding with a nucleus from a high Z atom, give rise to an inelastic scattering which makes the target nucleus unstable. As all the inelastic processes, the kinetic energy is not conserved. Thus, part of the energy of the incident neutron will be transferred to the nucleus as excitation energy. As a result of this excitation process, the nucleus will eventually emit one or more gamma rays.

$E_n <$ 10 MeV

Neutrons with energy lower than 10 MeV colliding with a nucleus, usually create elastic scattering events. In this kind of process, the kinetic energy is conserved. Thus, the neutron trajectory will be deflected and the energy lost by the neutron will be gained by the target nucleus which is displaced out of its position. If the target nucleus is heavy, the neutron energy loss results

small and its velocity remains unaffected by the impact, whereas if the target nucleus is light there is a high energy transfer and the neutron slows down.

$E_n < 0.5$ eV

Neutrons with energy lower than 0.5 eV are defined as *slow*. During their interaction with a nucleus, they are thermalized and captured by the nucleus itself, resulting in a compound nuclear structure which is usually highly unstable and radioactive[47]. The cross section for this interaction is inversely proportional to the velocity of the neutron, thus the slower the neutron, the larger the capture cross section. Hence, thermal neutrons are more likely subjected to the capture process. As the compound nucleus is unstable, the capture is usually followed by a gamma or beta emission.

2.3 Radiation damage in Silicon

Radiation damage in Silicon has two main effects, depending on the area where it takes place: surface damage, due to ionizing radiation and bulk damage, due to non-ionizing radiation. They have different damage mechanisms and effects on the macroscopic performance of the sensors. For this reason they are explained in detail in two proper sections.

2.3.1 Surface Damage

Surface damage in Silicon is caused by the creation of traps and fixed oxide charges at the interface between Silicon and dielectrics (mainly Silicon dioxide)[48]. These are mainly due to ionization events by charged particles and photons. The damage mechanism includes the creation of electron-hole pairs into the oxide ($\sim$ 18 eV are required to create an electron-hole pair in SiO_2) through the ionizing energy loss(IEL) of X-rays or ionizing radiation. A fraction of the pairs produced during the ionization process recombine. When a positive bias is applied, for example in a MOS device, the remaining electrons and holes take different paths: electrons drift toward the gate due to their high mobility and holes move toward the Si/SiO_2 interface where interface traps are mainly due to the depassivation of dangling bonds[49], hopping on the localized states into the SiO_2 bulk. During their migration toward the interface, holes can be trapped by defects inside the SiO_2 producing a fixed positive charge N_{ox}. Once holes are placed at the interface, their positive charge induces a negative charge in Silicon, generating interface traps in the Si bandgap. When an electric field is applied, traps at interface act as

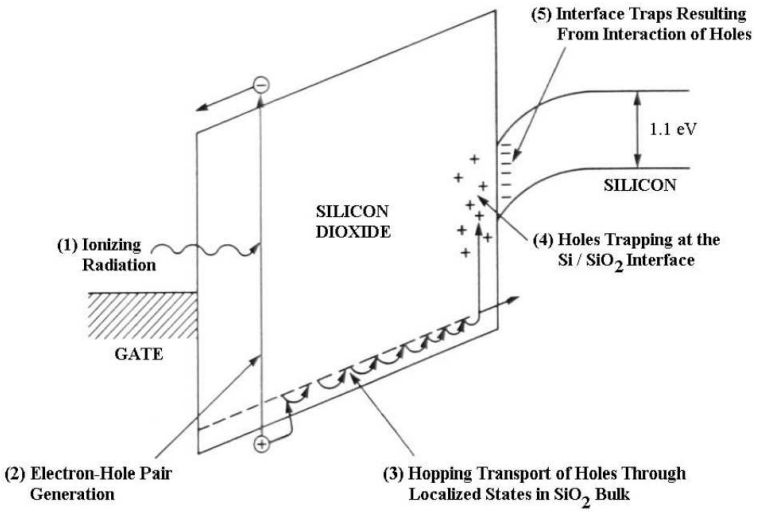

Figure 2.5: Schematic view of the effect of the ionization radiation on a MOS device positively biased[48].

generation centers for a surface current, that in this work will be named as *leakage current* I_{leak}, at least when dealing with SiPMs. The positive charge trapped at the interface can be subjected to a slow annealing process due to tunnel and thermal effects. Annealing can take place not only at the end of the irradiation, but also during irradiation, depending on the temperature, the electric field in the oxide, and the dose rate used for the irradiation[48]. In Fig.2.5 a graphical example of the effect of the ionization radiation on a MOS sensor is visible.

2.3.2 Bulk Damage

Bulk damage in Silicon is caused by the displacement of the Silicon atoms called Primary Knock-on Atoms (PKA) out of their primary site inside the lattice, creating a *vacancy*. This process causes the formation of a point defect and the displaced atom is called *interstitial*. Bulk damage is mainly produced by hadrons or highly energetic leptons and represents the major source of radiation damage in Silicon. When the particle is extremely energetic, it can still have enough energy after generating the first vacancy-interstitial (V-I), called *Frenkel pair*, to create others along its path, giving rise to a PKA cascade. Multiple defects agglomeration are called *clusters*.

The displacement of the PKA can happen only under the assumption that the energy transferred from the incident particle is larger than the minimum energy required to remove an atom from the Silicon lattice (displacement

threshold energy). Assuming a non-relativistic approach, the energy transferred during a collision is given by[50]:

$$E_{R,max} = 4E_p \frac{m_p m_{Si}}{(m_p + m_{Si})^2} \tag{2.5}$$

where E_p is the kinetic energy of the recoil atom under the hypothesis of an elastic scattering. Assuming a displacement threshold energy of 25 eV and a minimum energy required to create a cluster of 5 keV[50], the minimum energy required to a neutron to generate a Frenkel pair and a cluster is 185 eV and 35 keV, respectively. In the case of electrons, these energy values get very high. Indeed, electrons are required to have approximately 255 eV and 8 MeV to generate a Frenkel pair and a cluster, respectively. Using Eq.2.5, electrons from ^{60}Co can provide a maximum energy of 1 MeV during the collision, thus it can be safely assumed that electrons only create point defects.

A rate of atomic displacements can be defined as:

$$\frac{R_d}{N} = \int_0^{E_{max}} \phi(E_i) D(E_i) dE_i \tag{2.6}$$

where N is the material density of atoms (atoms/cm^3), ϕ is the energy dependent flux distribution and D(E) is the displacement cross section (also known as *Displacement damage function[50]*).

The displacement cross section is given by the sum of the number of atomic displacements $\nu(T)$ (also known as Lindhard partition function, where T is the recoil energy of the displaced atom created by a particle with energy E_i undergoing the reaction ν) produced by PKAs with energies E from T_{min} to T_{max}:

$$D(E_i) = \int_{T_{min}}^{T_{max}} \sigma_\nu(E_i, T) \nu(T) dT \tag{2.7}$$

where σ_ν is the cross section corresponding to ν-th reaction channel. To estimate $\nu(T)$, the Kinchin-Pease Model was developed in 1955[51]. It assumes different values for the number of atomic displacement function within the integration interval:

$$\nu(T) = \begin{cases} 0 & for \quad T < E_d \\ 1 & for \quad E_d < T < 2E_d \\ \frac{T}{2E_d} & for \quad 2E_d < T < E_c \\ \frac{E_c}{2E_d} & for \quad T \geq E_c \end{cases} \tag{2.8}$$

where E_c is the energy required to create a cluster of defects.

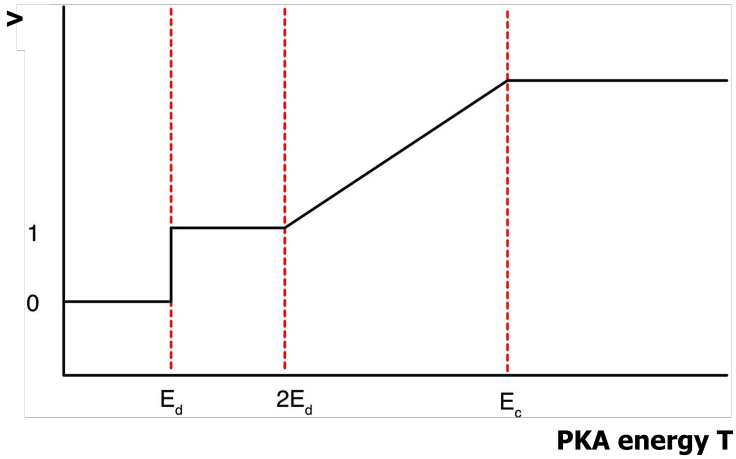

Figure 2.6: Number of displaced atoms ν as a function of the PKA energy.

NIEL scaling hypothesis

The Non Ionizing Energy Loss (NIEL) scaling hypothesis was introduced to compare the displacement damage of several particles. Indeed, defects are due to the interaction between the particles and the material lattice atoms. As different particles result in different interactions, the resulting damage will change depending on the particle under consideration. Fig.2.7 shows the curves of the displacement damage function D(E) as a function of the particle energy for different particle types. From this figure, we can observe how differently the several particles interact with Silicon atoms. Protons damage function is partially dominated by Coulomb interaction at lower energies, whereas nuclear interactions start to prevail at around 60 MeV. Neutrons damage function is not influenced at all by Coulomb interaction, indeed it results smaller than the proton one, at least up to the GeVs, when the two curves approach to fairly common values. Pions are affected by delta resonance up to a few hundred of MeV, then their only damage contribution is provided by nuclear interactions, thus the curve approaches to about 2/3 of that of protons [50].

To compare the displacement damage of the several particles it is useful to introduce a new quantity, the so-called *Impact factor* κ, which represents the rate of atomic displacement already introduced above, normalized at the rate of atomic displacements of a 1 MeV neutron:

$$\kappa = \frac{\int D(E)\phi(E)dE}{D(E_n = 1MeV)\int \phi(E)dE} \tag{2.9}$$

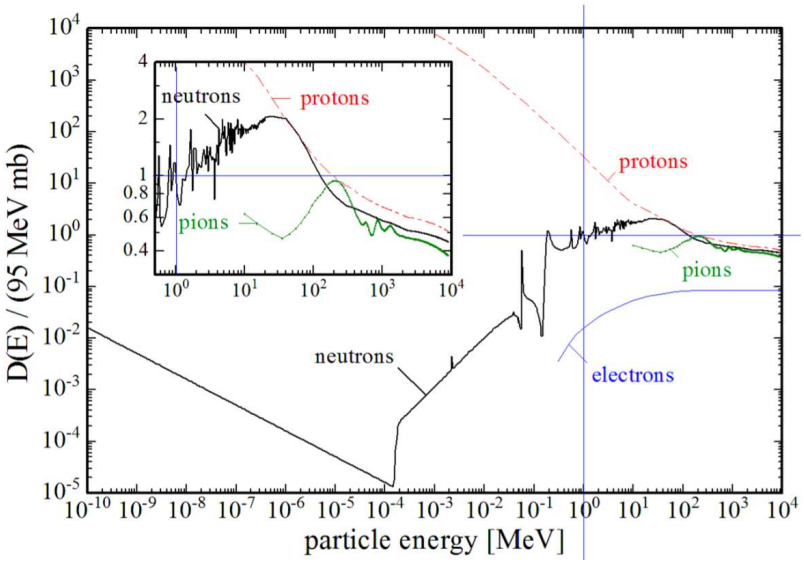

Figure 2.7: Displacement damage function in Silicon for different particles[52], normalized to 95 MeVmb which represents the equivalent damage of a 1 MeV neutron.

where D($E_n = 1$ MeV) is set at 95 MeV[50]. In Fig.2.8 a simulation of the vacancies distribution inside a 1×1 μm^2 region for different types of incident particles can be observed.

From Eq.2.9 follows that the fluence of equivalent neutrons can be estimated as:

$$\phi_n = \kappa\phi \tag{2.10}$$

Basically, the impact factor is helpful to convert the fluence of a certain class of particles at different energies to the fluence of 1 MeV equivalent neutrons required to operate the same displacement damage on the target material.

E_p [MeV]	κ
60	1.7
74	1.5
148	1.1

Table 2.1: Impact factors of proton at several energies of interest for this work.

In Tab.2.1, the impact factors of protons at the energy of interest of this work are listed.

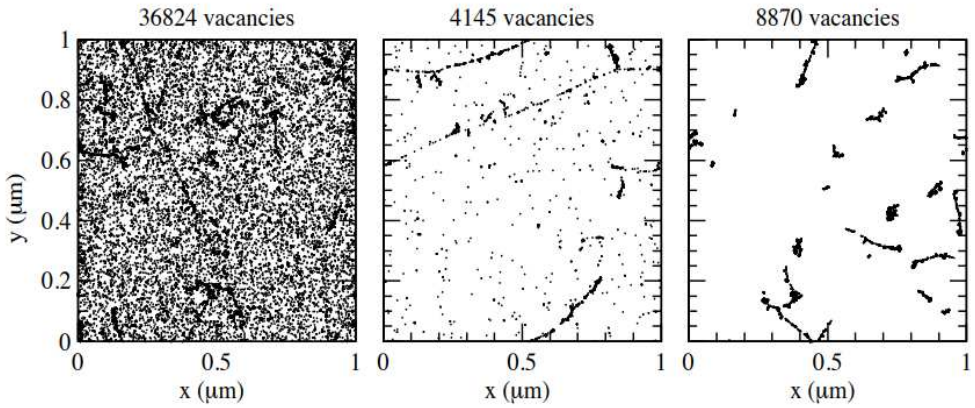

Figure 2.8: Distribution of vacancy defects over 1 μmm depth, after irradiation at fluence $\phi = 10^{14}$ cm^{-2} with different features of the incident particles: 10 MeV protons (left), 24 GeV/c protons (middle) and 1 MeV neutrons (right) [53].

2.3.3 Defects

Displacement damage in the bulk of the Silicon is responsible for the defects generation, in the form of *point-like defects* or more complex structures called *clusters*. A cluster is a complex structure of point-like defects that forms at the very end of the displacement cascade. Their nature and structure is still under investigation.

Point Defects

Point defects can be assumed having single vacancies or interstitials, divacancies or di-interstitials combined with impurities. They can be produced by radiation but also by fabrication process or doping. [54]. It can be useful to make a classification based on the generic electrical properties of the defects inside a semiconductor:

- **Acceptors, Donors, Amphoteric**: *Acceptors* are defects which becomes negatively charged when occupied by an electron and the Fermi level is located above the defect level, otherwise they are neutral (-/$\circ$). *Donors* are defects which become positively charged when occupied by a hole and become neutral when occupied by electrons ($\circ$/+). Conversely, donors are positively charged when the Fermi level is located below the defect level, otherwise they are neutral. Defects can have more than one level in the band gap. Indeed, *Amphoteric* defects have

both acceptor and donor levels. For a graphical overview of these charge states, see Fig.2.9 [50].

The ionization energy required to emit an electron in the CB or a hole in the VB is given by the module of the difference between the energy of the band and the trap energy level E_t.

- **Shallow and deep levels**: defects are usually called *shallow* if they are ionized at room temperature, otherwise they are called *deep*. The shallowness condition is strongly dependent on the Fermi energy level position and the doping concentration of the material.

- **Contribution to the space charge**: shallow defects very close to the CB can be easily ionized and charged at room temperature. This can change the effective doping concentration (N_{eff}). From the trend of the Fermi-Dirac distribution function in Fig.1.5, it can be observed that the energy levels in the upper region of the band gap are usually not occupied by electrons whereas the levels in the lower region can be occupied by electrons with an higher probability. Conversely, upper energy levels are usually occupied by holes. For this reason, defects contribute to the charge occupation of the traps in different ways. For instance, acceptors in the upper part of the energy gap close to the CB like the VO_i are mostly neutral unless they are filled by electrons. The same happens for a donor in the lower region close to the VB, like C_iO_i. These two examples of defects does not have any consequence on the effective doping concentration.

Cluster Defects

Clusters consist mainly in large agglomerations of vacancies and interstitials arranged in complex structures in a volume of about (15-20 nm)^3 with 10^5-10^6 atoms[55]. They were originally studied through the impact on the bulk damage of heavy hadrons and particles which are not supposed to form clusters like γ-rays or electrons[50]. Defects inside clusters seem to behave like the point defects, which means that they follow the electrical properties listed above.

SRH statistic

The main practical consequence of the radiation damage is the introduction of energy levels (E_t) inside the band gap.

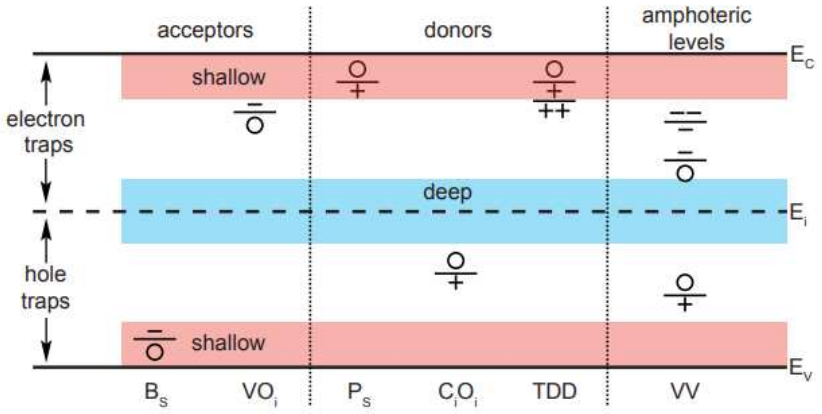

Figure 2.9: Possible charge states of acceptors, donors and amphoteric defects within the band gap: B_s (acceptor in lower half), VO_i (acceptor in upper half of the band gap), P_s (donor in upper half), C_iO_i (donor in lower half), TDD (thermal double donor), VV (amphoteric divacancy). Figure taken from[54].

Similarly to what already observed in Eq.1.7 and 1.8, if the Fermi level is known, the occupation of the traps into the band gap by the charge carriers can be estimated. For a concentration of traps N_t, the fraction of electrons and holes which occupy an energy level E_t within the band gap is:

$$n_t = N_t \frac{1}{1 + exp\Big(+ \frac{E_t - E_F}{k_B T}\Big)} = N_t F(E_t) \tag{2.11}$$

$$p_t = N_t \frac{1}{1 + exp\Big(- \frac{E_t - E_F}{k_B T}\Big)} = N_t (1 - F(E_t)) \tag{2.12}$$

where F(E_t) is the Fermi-Dirac distribution function, which is the probability that an energy state E_t is occupied by an electron. The *totality conditions* $N_t = n_t + p_t$ tells us that when a trap is not occupied by an electron, it is assumed as occupied by a hole, and vice versa. This is considered as a statistical process according to SRH theory, with four rate contributions:

(a) Electrons emission in the conduction band with rate

$$r_a = e_n n_t \tag{2.13}$$

(b) Electrons capture into non-occupied states

$$r_b = c_n p_t n \tag{2.14}$$

(c) Holes capture into states occupied by electrons (equivalent to emission of electrons in valence band)

$$r_c = c_p n_t p \tag{2.15}$$

(d) Holes emission into valence band

$$r_d = e_p p_t \tag{2.16}$$

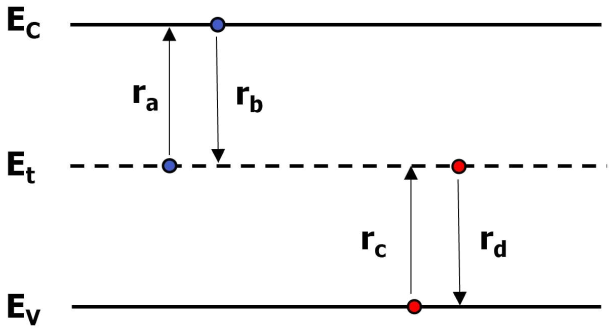

Figure 2.10: Emission and capture process of electrons and holes from the energy level E_t.

where $e_{n,p}$ and $c_{n,p}$ are called *emission rate* and *capture rate*, respectively. Electrons emission rate r_a is proportional to the energy levels occupied by electrons, while the rate of capture of electrons r_b is proportional to the energy levels occupied by holes and also to the concentration of electrons in CB. The exchange of electrons through capture and emission at the energy level E_t leads to the differential equation:

$$\frac{dn_t}{dt} = -r_a + r_b - r_c + r_d \tag{2.17}$$

$$= -e_n n_t + c_n p_t n - c_p n_t p + e_p p_t \tag{2.18}$$

The concentration of free electrons in CB and free holes in VB are supposed to be constant, according to the *principle of detailed balance*[50]. Thus, the exchange of carriers to the CB and VB must have the same rate ($r_a = r_b$), which, using Eqs.2.13 and 2.14, in the case of electrons leads to:

$$e_n n_t = c_n p_t n \tag{2.19}$$

Taking into account Eqs.1.9, 1.10 and 1.13, the expression for the emission rate can be derived:

$$e_{n,p} = c_{n,p} n_i exp\left(\pm \frac{E_t - E_i}{k_B T} \right) \tag{2.20}$$

$$= c_{n,p} N_{C,V} exp\left(\pm \frac{E_t - E_{C,V}}{k_B T} \right) \tag{2.21}$$

The change in energy during a carrier emission from a trap can be considered as a process at constant temperature and pression, thus as an exchange of Gibbs energy, described by the equation:

$$\Delta E_{n,p} = \Delta H_{n,p} - T \Delta X_{n,p} \tag{2.22}$$

where H and S represent the *enthalpy* $H_{n,p}$ and the *entropy* $X_{n,p}$ of the reaction, respectively. Introducing these new quantities:

$$E_C - E_t = \Delta H_n - k_B T ln(X_n) \tag{2.23}$$

$$E_t - E_V = \Delta H_p - k_B T ln(X_p) \tag{2.24}$$

Eq.2.21 can thus be expressed as:

$$e_{n,p} = c_{n,p} N_{C,V} X_{n,p} exp\left(- \frac{\Delta H_{n,p}}{k_B T} \right) \tag{2.25}$$

A capture coefficients can be introduced as a measure of the distance required to a carrier to be captured by a center and it is related to the *capture cross section* by the expression[54]:

$$X_{n,p} c_{n,p} = \sigma_{n,p} v_{th,n,p} \tag{2.26}$$

where v_{th} is the *thermal velocity* near the edges of the CB and VB, given by the equation:

$$v_{th} = \sqrt{\frac{3 k_b T}{m^*}} \tag{2.27}$$

where m^* is the effective mass.

Under the assumption that $\sigma_{n,p}$ is independent on the temperature which leads us to neglect the variation of entropy, ΔH becomes a new quantity that represents a key parameter for SiPMs: the *Activation energy* E_a.

Finally, Eq.2.26 can be inserted into the emission rate expression to get the final expression of the emission rate:

$$e_{n,p} = \sigma_{n,p} v_{th,n,p} N_{C,V} exp\left(- \frac{E_a}{k_B T} \right) \tag{2.28}$$

Defects under reverse bias

In reverse bias condition, defects inside a Silicon p-n junction based sensor without internal amplification generate a current given by:

$$I_{bulk}(T) = V_{depl} q_0 \Big(\sum_{accept} e_n(T) n_t(T) + \sum_{don} e_p(T) p_t(T) \Big) \tag{2.29}$$

where V_{delp} represents the volume of the depletion region and q_0 is the elementary charge. In these conditions there are two cases depending on the charge properties of the defect:

- **Acceptor-like defect** ($e_p = 0$):

$$I_{bulk}(T) = V_{depl} q_0 e_n(T) n_t(T) \tag{2.30}$$

- **Donor-like defect** ($e_n = 0$):

$$I_{bulk}(T) = V_{depl} q_0 e_p(T) p_t(T) \tag{2.31}$$

For highly-irradiated devices, the current increase so high that $n \approx p \approx 0$ is no longer valid, thus the capture of free carriers in the depletion region has to be considered.

Therefore, the occupation of defects by electrons and holes can be estimated as:

$$n_t = N_t \frac{c_n n + e_p}{e_n + e_p + c_n n + c_p p} \tag{2.32}$$

$$p_t = N_t \frac{c_p p + e_n}{e_p + e_n + c_p p + c_n n} \tag{2.33}$$

For low irradiated devices, the free charge carriers in the space charge can be neglected (n $\approx$ p $\approx$ 0). Thus, the occupation of defects equations can be simplified as follows:

$$n_t = N_t \frac{e_p}{e_n + e_p} \tag{2.34}$$

$$p_t = N_t \frac{+e_n}{e_p + e_n} \tag{2.35}$$

Introducing these equations into Eq.2.30 and 2.31, a new expression for the bulk current can be observed:

$$I_{bulk}(T) = q_0 V_{depl} N_t \frac{e_n e_p}{e_n + e_p} \tag{2.36}$$

It is also possible to calculate the generation rate of the electron-hole pairs from defect states:

$$G_t = e_n n_t = e_p p_t = N_t n_i \frac{c_n c_p}{c_n exp\left(\frac{E_t - E_i}{k_B T}\right) + c_p \left(\frac{E_t - E_i}{k_B T}\right)} \tag{2.37}$$

Only defects centers with energy E_t close to the intrinsic Fermi level E_i can be assumed to contribute to the generation rate. In these cases, we can assume $c_n = c_p$, thus the generation rate results in a simplified form:

$$G_t = \frac{N_t n_i c_n}{2cosh\left(\frac{E_t - E_i}{k_B T}\right)} \tag{2.38}$$

The new expression of G_t provides a further expression of the bulk current:

$$I_{bulk}(T) = \sum_{traps} q_0 G_t V_{depl} \tag{2.39}$$

which holds only under the assumption of E_t close to E_i.

Defects under forward bias

When a forward bias is applied to the sensor, a large amount of charge carriers move through the junction. This unbalances the emission and capture rates. Indeed, capture rate gets much higher than emission one, setting a new condition:

$$c_n n >> e_n \quad and \quad c_p p >> e_p$$

When introducing this condition in Eq.2.18, the occupation of defect levels results simplified:

$$n_t = N_t \frac{1}{1 + \frac{c_p p}{c_n n}} \tag{2.40}$$

$$p_t = N_t \frac{1}{1 + \frac{c_n n}{c_p p}} \tag{2.41}$$

From Eq.2.41 we can conclude that defects will be filled by electrons when the condition $c_n > c_p$, while they will be filled by holes when $c_p > c_n$.

2.3.4 Annealing

Annealing is one of the key features of Silicon sensors, especially when highly irradiated, thus damaged by radiation. Indeed, annealing enable the sensor to partially recover over a certain time interval or under certain temperature ranges. Annealing mechanism consists into two stages:

- **Migration**: defects begin to move under certain temperature conditions. They migrate through the material until they are trapped into *sink*[50] (e.g. surface, dislocations) or they associate with other defects to make a complex defect structure.

- **Dissociation**: A complex structure dissociate into its components when the phonon energy of the lattice is higher than the binding energy which keeps them together. Then, the single components are subjected to the migration process.

In general, defects annealing test can be performed in two ways: *isochronal annealing*, which consists in the variation of the temperature in a fixed time interval or *isothermal annealing*, consisting into the observation of the annealing evolution in a long time interval at fixed temperature.

The impact of the annealing process on the sensors can be outlined into three main processes:

(a) **Bulk current decrease**: before discussing this point, it would be better to introduce the *damage parameter* α which represents the proportional factor between the increase of the bulk current and the irradiation fluence

$$\frac{\Delta I}{V_{depl}} = \frac{I(\phi) - I(\phi_0)}{V_{depl}} = \alpha\phi \tag{2.42}$$

where $I(\phi)$ is the current of the irradiated sample, $I(\phi_0)$ is the current of the non irradiated sample and V_{depl} is the depleted volume.

Annealing produces a decrease of the bulk current in terms of a decrease of the α coefficient in time (see Fig.2.11) through the equation[50]:

$$\alpha(t) = \alpha_0 + \alpha_I exp\Big(-\frac{t}{\tau_I}\Big) - \beta ln\Big(\frac{t}{t_0}\Big) \tag{2.43}$$

where $\alpha_I \approx 1.25{\times}10^{-17}$ A/cm, $\beta \approx 3{\times}10^{-18}$ A/cm and $t_0 = 1$ min, while α_0 and τ_I are dependent on the temperature.

(b) **Space charge**: shallow traps ($\Delta E << k_B T$) are ionized at equilibrium and can contribute to the space charge in the depletion region [56], while deep traps ($\Delta E >> k_B T$) are not and their thermal activation is low at equilibrium, as well as the filling of the traps due to the low density free carriers. Deep traps close to the borders of the depletion region can switch between the depleted and charged states, getting empty or filled (thus charged) respectively. This leads to a non-uniform

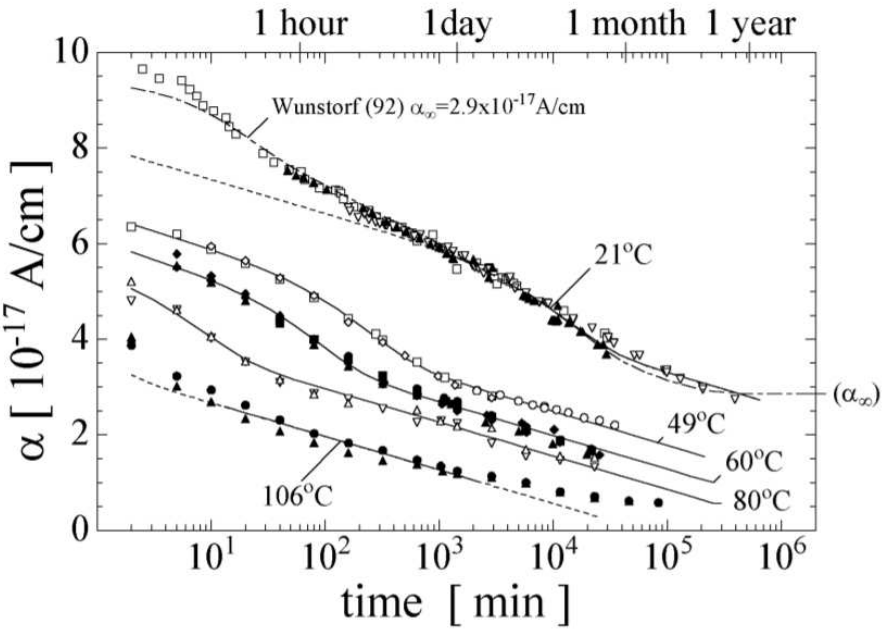

Figure 2.11: Current related damage rate α as a function of the annealing time at different temperatures[50].

charge distribution of deep levels which, in case of fully-depleted irradiated sensors (fluence higher than 10^{14} cm^{-2}), can produce some peaks in the electric field near the two neutral regions[57].

After a certain annealing time interval, space charge can be subjected to *reverse annealing*, consisting into the variation of the effective doping concentration ΔN_{eff}, defined as function of fluence and time:

$$\Delta N_{eff}(\phi, t(T_a)) = N_{eff}(\phi_0) - N_{eff}(\phi, t(T_a)) \tag{2.44}$$

where T_a represents the annealing temperature.

The variation of effective doping concentration can be modeled according to the *Hamburg model*, consisting into three main contributions (see Fig.2.12):

$$\Delta N_{eff}(\phi, t(T_a)) = N_C(\phi, t(T_a)) + N_A(\phi, t(T_a)) + N_Y(\phi, t(T_a)) \tag{2.45}$$

where each term contributes to a damage process:

– $N_C(\phi, t(T_a))$: called **stable damage**, consisting in a *donor removal* term (dependent exponentially on the annealing tempera-

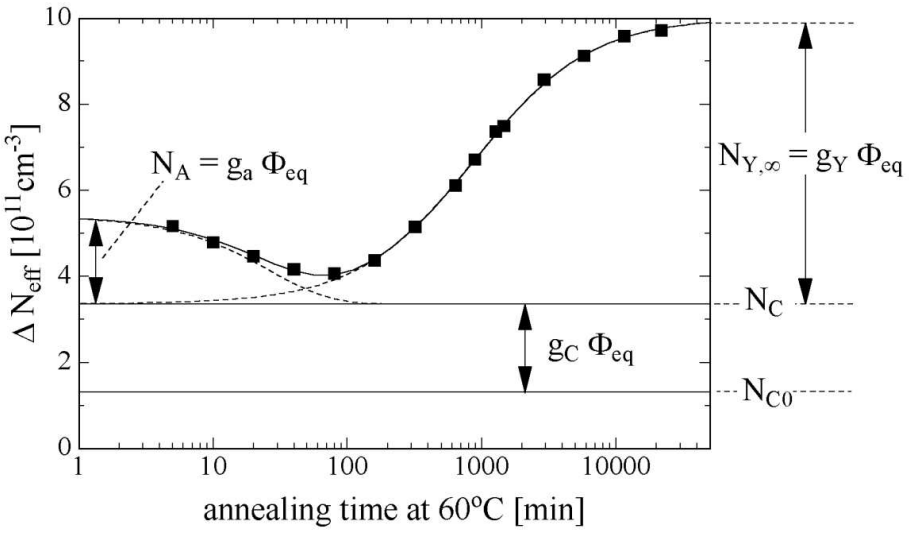

Figure 2.12: Annealing behavior of radiation induced changes in the effective doping concentration at 60° for an example of type WE-25kΩcm irradiated with a fluence of 1.4×10^{13} cm-2[50].

ture) added to a *stable acceptors* term proportional to the fluence:

$$N_C = N_{C,0}(1 - exp(-c\phi)) + g_c\phi \tag{2.46}$$

– $N_A(\phi, t(T_a))$: called **short term annealing** contribution, taking into account the increase of N_{eff} as a consequence of the variation of the full depletion voltage V_{depl}, which leads the type inverted detectors with negative N_{eff} to become less negative and the not type inverted detectors with positive N_{eff} to become more positive. This effect is usually attributed to an annealing of acceptors[50]. This contribution is given by the equation:

$$N_A = \phi \sum_i g_{a,i} exp\Big(-\frac{t}{\tau_{a,i}}\Big) \tag{2.47}$$

– $N_Y(\phi, t(T_a))$: called **reverse annealing**, representing an opposite effect to the beneficial annealing. It is given by the equation:

$$N_Y = N_{Y,\text{inf}}\Big(1 - \frac{1}{1 + t/\tau_Y}\Big) \tag{2.48}$$

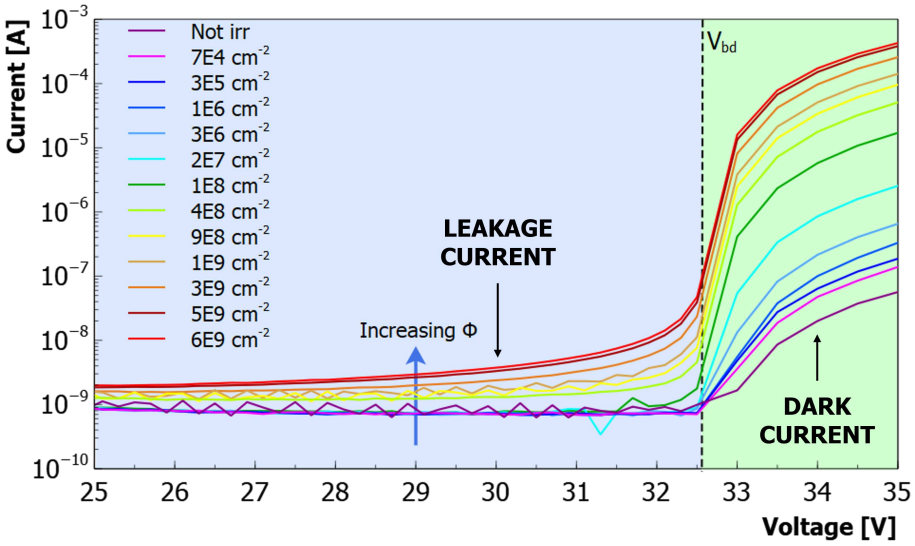

Figure 2.13: Example of reverse current-voltage plot of an FBK SiPM irradiated at several fluences with protons, thus experiencing both surface and bulk damage, as visible from the increase of the current above (green) and below (blue) the breakdown voltage.

2.4 Radiation damage in SiPMs

One of the main differences between SiPMs (or SPADs) and other kinds of fully-depleted Silicon sensors (tipically used in HEP applications) is the presence of an internal gain, due to the avalanche multiplication generated by the high electric field.

The main macroscopic effect of the radiation damage on SiPMs is the increase of the current below and above the breakdown called *leakage current* (I_{leak}) and *bulk current* (I_{dark}), depending on the region where defects are produced. Fig.2.13 the current-voltage plot of a NUV-HD-cryo FBK SiPM with a 45 μm cell pitch measured at approximately 20°C is shown, where the pre and post breakdown regions are clearly visible.

Another effect of the radiation on SiPMs is the loosing of the single-photon resolution, which usually happens when irradiated at around $\phi = 10^9 - 10^{10}\ n_{eq}/cm^{-2}$, where the photo-electron peaks are no longer resolved, at least at room temperature[49]. When cooled, the rate of dark events due to damage drops, thus below certain temperature values SiPMs sill can resolve single photons even if heavily damaged. The loosing of the single-photon resolution makes the estimation of the functional SiPMs parameters very challenging, thus new measure approaches need to be explored.

2.4.1 Surface damage in SiPMs

Electrons and photons with energies under the threshold for the creation of defects into the bulk (∼300keV) generate only defects in the oxide on the surface of the SiPM (∼18 eV).

From current-voltage measurements the electrical parameters of SiPMs can be extracted: quenching resistance R_q and pixel capacitance C_{pix}. Their product $\tau_{RC} = C_{pix}R_q$ represents the recharge time constant of the single pixel. R_q and C_{pix} are not supposed to suffer of the surface damage, thus they are expect to remain constant with irradiation[49].

Due to the increase of the surface-generation current at the interface between silicon and oxide, leakage current tend to increase significantly (∼3 orders of magnitude) above 20 MGy[49], whereas the dark count rate (DCR) is only slightly affected by this effect, leading to an increase of maximum an order of magnitude. The reason for the difference between the increase of the current and the DCR is that the surface current does not get multiplied by an avalanche because it does not reach the high-field region of the microcells, at least in the majority of cases (the role of the surface-generated current in determining the increase of the DCR depends also on the type and characteristics of the SiPM technology being considered).

2.4.2 Bulk damage in SiPMs

The main macroscopic effect of the radiation damage on the bulk of a SiPM consists in the increase of the dark current I_{dark}, which is caused by the increase of the DCR. If the DCR increases to very high levels (approximately above 10 MHz at ∼20°C) it is difficult to measure directly the main parameters of the device by waveform analysis, as it becomes very to separate individual pulses because of pile-up. Indeed, the increase of the noise affects the single-photon counting resolution which gradually decreases as the damage increase. From literature we can state that at fluences in the order of 10^9-10^{10} cm^{-2}, all SiPMs lose single photon resolution when operating at room temperature[49]. This leads to the need to develop alternative measure approaches to fully characterize the SiPMs.

γ-rays and electrons

γ-rays effects on the SiPMs are described in detail in[58]. When exposed to γ-rays, both the surface and the bulk of SiPMs are affected by the radiation damage. In [58], MPPC (SiPM produced by HPK) were irradiated with ^{60}Co at several doses up to 240 Gy, showing an increase of the current and the

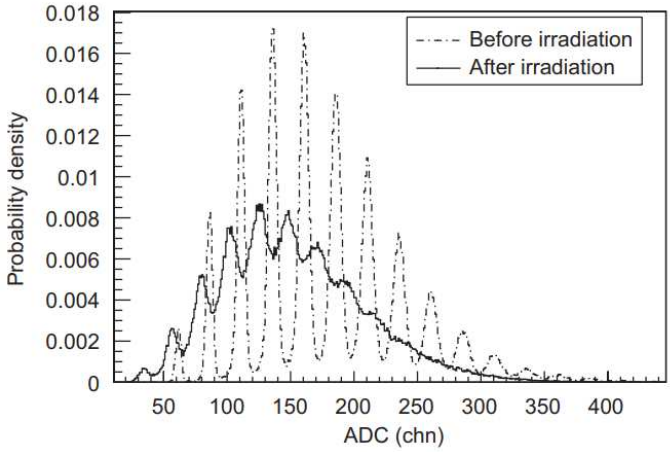

Figure 2.14: Single-photon spectra before and after irradiation with 14 MeV electrons at ϕ=3.1 $\times$ 10^{11} cm^{-2}.

DCR, while the cross-talk and the gain appear not to be affected by the radiation damage.

The effect of the electrons on the SiPMs is described in [59], where SiPMs are irradiated with 14 MeV electrons up to 3.8 $\times$ 10^{11} cm^{-2}. Fig.2.14 shows the single photoelectron spectra before and after irradiation. As visible from the figure, single photo-peaks are still visible after irradiation, although a pedestal is also visible in the current, as a consequence of the surface damage[59] that causes an increase of the leakage current and, thus, of the electronic noise in the baseline of the waveforms obtained with the front-end. At 3.8 $\times$ 10^{11} cm^{-2}, single peaks are no longer visible and saturation effects start to affect the dynamic range of the SiPMS and, as a consequence, the PDE and the gain, as will be described in detail in the next paragraph.

Hadrons

While γ-rays and electrons does not seem to affect the electrical parameters of the SiPMs (breakdown voltage (V_{bd}), quenching resistance (R_q), capacitance (C)), this no longer holds when dealing with hadrons, depending on their irradiation fluence. Indeed, for hadron fluences lower than 10^{12} cm^{-2} no significant changes are expected in breakdown voltage, quenching resistance, capacitance, PDE and gain, while noise is supposed to suffer of radiation damage even at low fluence. At fluence higher than 10^{12} cm^{-2}, radiation is expected to affect even other parameters[49].

Quenching resistance was observed to change with both fluence above 10^{12} cm^{-2} and temperature, as described in [60]. Breakdown voltage variations

with fluence were analyzed in [28], where a shift was observed at fluence levels in the range $6 \times 10^{12} - 2 \times 10^{14}\ cm^{-2}$ up to 4V. The shift value can change depending on the SiPM layout and doping profile but SiPMs with thinner multiplication regions appear less sensitive to breakdown voltage shifts[49].

Reverse current increases with fluence, before and after the breakdown voltage and independently on the cell size. Therefore, the DCR increases with fluence because of its relation with the dark current. The DCR can be estimated by the reverse dark current through the relation:

$$DCR = \frac{I_{dark}}{q \times ECF \times G} = \frac{I_{dark}}{qG_c} \tag{2.49}$$

Thus, DCR increase can be estimated from the dark current assuming that the current gain does not change with fluence. This condition is not always true and needs to be verified, at least at high fluences where the correlated noise can experience damage effects. For very high DCR, SIPM can suffer a saturation effect, which means that the cells are not fully recovered from the previous discharge and can not be triggered once again. This leads to a signal reduction, a smaller gain and a reduction of the PDE. As far as PDE is concerned, a direct measure with pulse-counting method is not always straightforward when SiPMs are damaged and noise gets very high, thus usuallly alternative approaches need to be developed. An example could be a direct measure of the current Responsivity in response to light signals.

Chapter 3

Proton irradiation tests at LNS

Several irradiation campaigns were carried out in order to investigate the effects of the radiation on the SiPMs performance, exploring different particles such as protons and X-rays. Several FBK SiPMs were irradiated during the tests, produced with different technologies. This might be useful to compare the effects of different kinds of radiation and to better understand the main damage mechanisms happening during the interaction. In particular, protons can produce IEL and NIEL damage, for this reason their effects on the performance of the SiPMs should be found at the interface between the silicon and the oxide, and into the bulk. In particular, in this chapter we will investigate the NIEL damage through the irradiation of several FBK technologies at Laboratori Nazionali del Sud (LNS) in Catania.

3.1 Superconducting Cyclotron

The K800 Superconducting Cyclotron (SC) started operating in late 1994 to carry out the first nuclear physics experiment in July 1995[61]. The three sector isochronous Superconducting Cyclotron has a very compact structure with a pole radius of 90 cm, a total external radius of 190.3 cm and a height of 286 cm. It is equipped with two pairs of superconducting coils and a RF system operating in the range from 15 to 48 MHz [62] with seven magnetic channels and two bars of magnetic compensation. It can provide all ions in a range 10-80 MeV. In Fig.3.1 a view of the medial plane of the cyclotron can be observed. The current injection method is based on an ECR (Electron Cyclotron Resonance) source, producing ions with a very high charge states before being accelerated. Once ions are extracted, they are brought to the acceleration chamber of the Superconducting Cyclotron[63]. Positive ions are produced in the ECR source and injected along the acceleration chamber

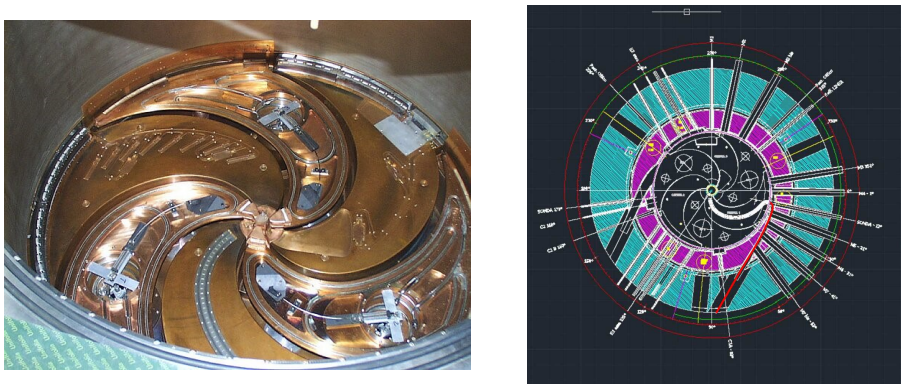

Figure 3.1: Medial plane of the cyclotron in real picture (left) and in simulation with details of the acceleration chamber and extraction line (red line)[64] (right).

covering spiral orbits with a frequency depending on the charge state, the magnetic field and their mass. When the energy of the beam reaches its maximum value, the particles are in the orbit with the maximum radius, they are extracted and brought to the experimental room through the extraction line (see Fig.3.1).

3.2 Experimental setup

The irradiation setup is shown in Fig.4.8 where a picture of the SiPM located on custom supports as naked dies and stacked together can be observed. Along the protons trajectory, a collimator with a 2.7 mm diameter was placed, followed by the stack of SiPM dies, a ionization chamber (IC, 50mm diameter) and a plastic scintillator (SCI, 3 mm thickness) at the end. The output photons were measured by photo-multiplier tubes (PMTs) to obtain the actual number of the protons passing through the dies.

Ten different FBK SiPM technologies (e.g. RGB-HD, NUV-HD[18], RGB-UHD[**?**]) were tested at eight different fluence values with 62 MeV protons in August 2019 from about 1.7×10^8 n_{eq}/cm^2 to 1.7×10^{14} n_{eq}/cm^2. The SiPMs were irradiated as naked dies. In particular, they were 3×3 mm^2 or 4×4 mm^2 test structures containing smaller SiPMs, mainly 1×1 mm^2 SiPMs. One chip per each technology type was irradiated at one of the selected proton fluences, to be able to characterize after irradiation the same type of SPM with different doses in the FBK laboratories, in dark and light environments. The dies were arranged in identical stacks (Fig.3.3). One stack at a time was inserted in the proton beam line by means of a motor-

ized linear stage and then irradiated. Each stack (ten in total) contained 10 SiPM dies, placed one in front of the other. Each chip was placed on a wafer dicing tape inserted in a 3D-printed plastic frame and all the samples in the stack were supposed to receive, simultaneously, almost the same irradiation dose. Eight stacks were irradiated with a different dose, a ninth stack was assembled but left outside the irradiation room, to be used as a reference for the estimation of the non-irradiated performance of the SiPMs.

The manual positioning of the dies inside the frames exposes the SiPMs to a small position uncertainty, estimated in less than ± 0.5 mm. This contributes to an uncertainty factor in the effective dose into the different stacks. The stacked-chip setup also exposes the beam to a moderate energy between two subsequent SiPMs into the same stack. The energy difference between the proton beam at the first and the last SiPM, estimated through Montecarlo simulations, was about 11 MeV, as shown in Fig.3.4 [65] and summarized in Tab.3.1. Each SiPM was simulated like a material with Z=14, with a 2330 mg/cm^3 density and a 600 μm thickness, while the support setup was considered negligible.

The choice to irradiate ten SiPMs inside the same stack required an analysis of the impact of each SiPM layer on the incident beam. From Fig.3.5 the simulation of the beam spread passing through the SiPM layers at different points can be observed, with a fit of each curve to extract the parameter of interest. In this case, the standard deviation of the beam provides an indication of the widening of the beam and enable us to quantify such a variation. In detail, the beam had a gaussian profile with a 1 mm FWHM in diameter, widening up to 1.5 mm between the first and the last SiPM in the stack. The SiPM dies had a variable dimension, between 3×4 mm^2 and 4.14×4.14 mm^2, thus the irradiation resulted non-uniform over the whole structure and the single 1×1 mm^2 SiPMs included in the die. Because of this non-uniformity, a specific fluence was calculated integrating the curve of the beam profile over the area of each SiPM, considering the same value of the center in each structure. A graphical representation of the non-uniformity of the beam spot on the SiPMs is visible in Fig.3.6, which shows the NUV-HD-RH technology test structure including six SiPMs with different cell pitch and layout features. From the figure an overlap of the layout image of the structure, the beam spot and a picture of the EMMI image (considering the secondary emission of photons) can be observed and a difference of fluence on the several SiPMs can be directly spotted.

The number of protons impinging on each SiPM was estimated through an ionization chamber (IC) and compared with the simulations. The IC current was integrated over the exposure time and then converted into the number of protons through the IC-SCI (scintillators) calibration and then

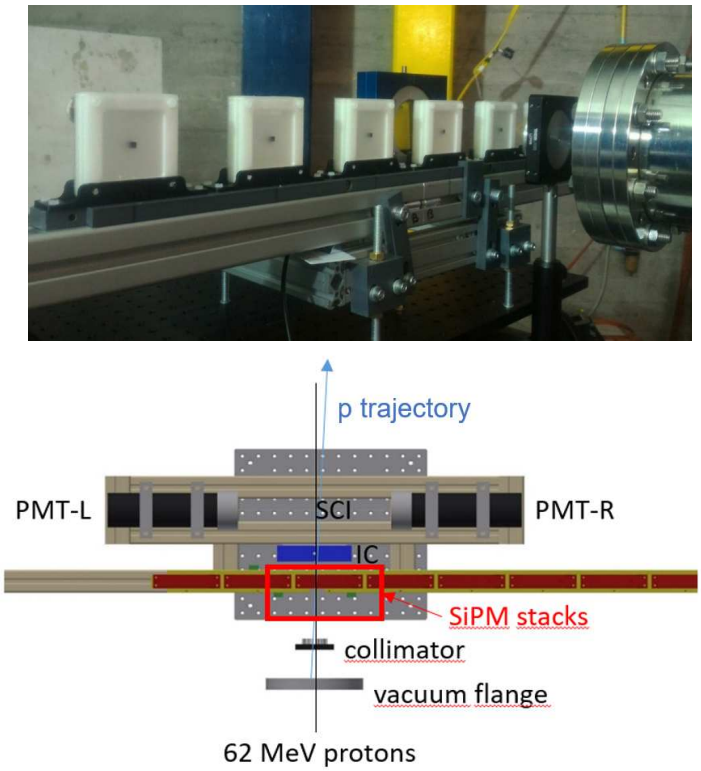

Figure 3.2: Picture and schematic representation of irradiation setup. Along the protons trajectory we placed a collimator, followed by the stack of the SiPM dies, an ionization chamber and two scintillators to measure the effective number of the protons passing through the dies. As showed in the picture, we were able to shift laterally the stack of the chip being irradiated to change the one hit by the ion beam.

corrected for a factor 0.97, corresponding to the loss of the protons while passing through the scintillators. This was estimated through Monte Carlo simulations. The resulting number of protons was multiplied by a different correction factor for each SiPM into the stack called "transmission factor t_{SiPM}" (see Tab.3.1), to take into account the losses caused by the widening of the proton beam along the stack and the different exposure of the 1×1 mm^2 SiPM structures with respect to the center of the beam (as shown in Fig.3.6).

As mentioned above, several FBK technologies were irradiated with different features and cell sizes. Among these technologies, only a few of them were characterized in terms of current, noise and PDE. In this sense, the most promising ones were investigated in detail: the NUV-HD, the RGB-

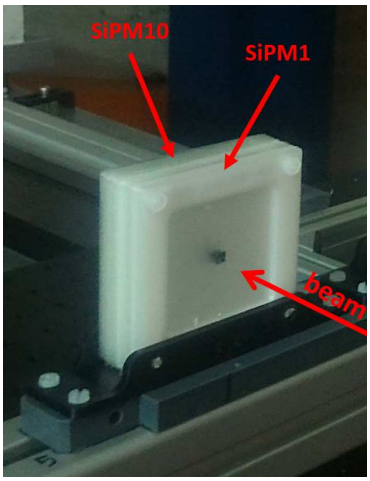

Figure 3.3: Picture of the stack containing the SiPMs during the irradiation.

	σ_x [mm]	E [MeV]	σ_E [MeV]	t_{SiPM}
$SiPM_1$	0.71	61.75	0.05	0.89
$SiPM_4$	0.72	58.20	0.20	0.87
$SiPM_7$	0.72	54.47	0.28	0.83
$SiPM_{10}$	0.75	50.53	0.35	0.81

Table 3.1: Summary of the results of ATIMA software[66] simulation of the beam spread, energy spread and transmission factor at $SiPM_1$, $SiPM_4$, $SiPM_7$ and $SiPM_{10}$.

HD, the NUV-HD-RH and the RGB-UHD-LF technologies. In Tab.3.2 the main features of the technologies considered are shown, with the depletion volume calculated through a TCAD simulation.

3.3 Characterization after irradiation

After irradiation the dies were left annealing for one month at room temperature (20÷25°C) and then mounted on PCB packages and characterized. In some cases the standard methods of characterization of the SiPMs have required some modifications, mainly due to their high nose levels. Moreover, other quantities to estimate the radiation damage have been introduced based on the main literature in the field of the silicon sensors. Most of these were developed for silicon sensors with no internal amplification, thus in some cases it has been necessary to modify these quantities in order to take into account SiPMs specific features, such as the gain and the avalanche trigger-

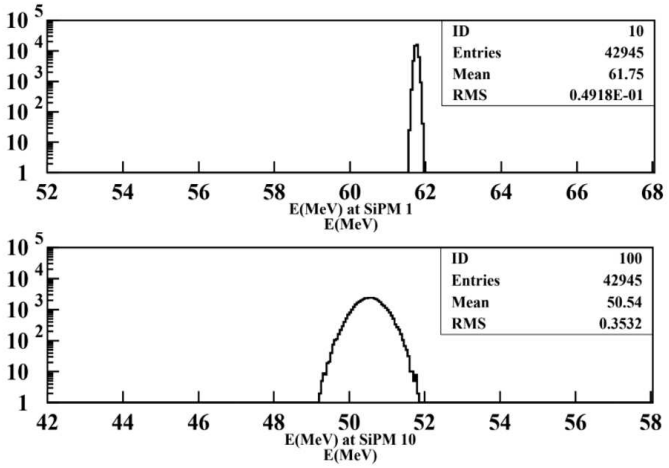

Figure 3.4: Simulated proton energy loss distributions at the first (upper) and the last (lower) SiPM in the stack.

ing probability. This latter is a very important parameter in Geiger mode detectors, it represents the probability of a generated electron or hole to start a self-sustaining avalanche current, thus a detectable output pulse.

All the measurements described in this section were performed at the FBK laboratories in Trento.

3.3.1 Reverse Current

Current measurements were performed on the naked structures at room temperature ($\sim 20°C$). In Fig.3.7 the current curves as a function of the reverse bias are plotted at the several fluence levels in dark conditions for the NUV-HD, RGB-HD, NUV-HD-RH and RGB-UHD technologies. An significant increase of the leakage current (pre-breakdown current) and the dark current (post-breakdown current) with the fluence can be noticed. In the plot of the RGB-HD SiPM an anomaly can be observed: the non-irradiated curve appears to be slightly higher than the irradiated ones up to 10^{10} n_{eq}/cm^2 in the pre-breakdown region. This anomaly is likely due to the intrinsic variability between one SiPM and another in terms of noise, because of the manufacturing process. In fact, this is the consequence of the choice of not to test the SiPMs before irradiation, considering instead a new set of SiPMs as the non-irradiated samples, although they were taken from the same production run.

To better quantify the worsening of the performance we introduced a new parameter "r" defined as the ratio between the current after irradiation ϕ (at

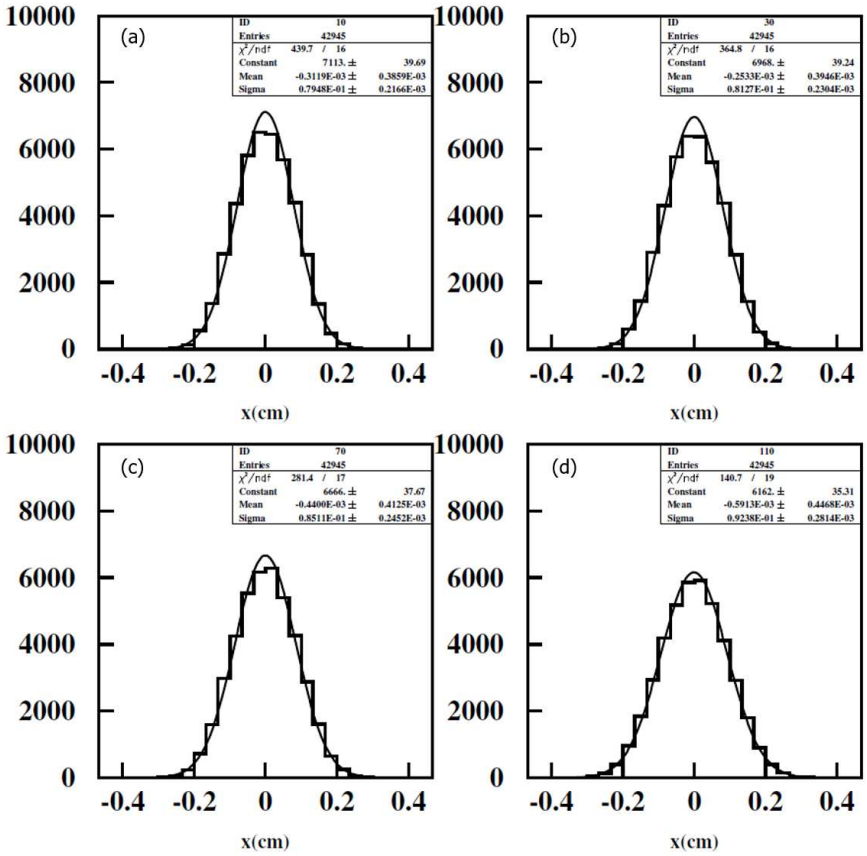

Figure 3.5: Beam spread passing through the SiPM layers (at SiPM1(a), SiPM4(b), SiPM7(c) and SiPM10(d)) with a fit to estimate and compare the sigma of the curves.

a specific fluence) and before irradiation ϕ_0. This parameter represents the relative increase of the current after the specific irradiation, without taking into account the gain and the correlated noise of the SiPM which, instead, are assumed as constant:

$$r = \frac{I_\phi(V_{ex})}{I_{\phi_0}(V_{ex})} \tag{3.1}$$

where V_{ex} is the excess bias, i.e. the difference between the applied reverse bias and the breakdown voltage. Here, the breakdown voltage is assumed not changing with irradiation, at all the fluences considered in this work, as will be discussed in the dedicated section later in the text. Thus, as a first approximation, the current ratio **r** provides information about the evolution of the damage with the fluence.

In Fig.3.8 the parameter r is plotted as a function of the fluence at 5 V of

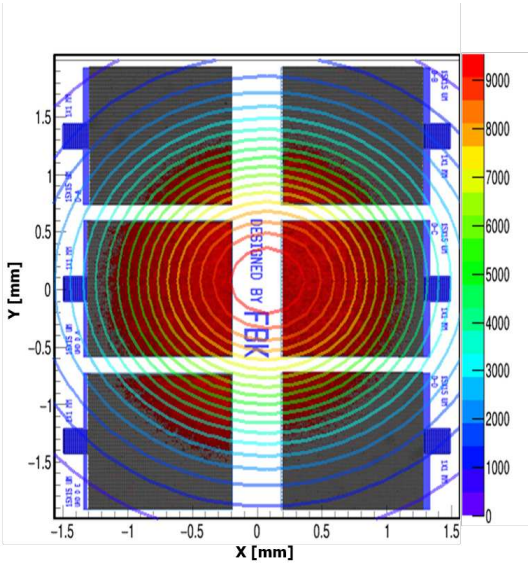

Figure 3.6: Example of superposition of: i) contour lines, representing the estimated irradiation intensity (i.e. beam profile from simulations), ii) emission microscopy (EMMI) intensity, measured with SiPMs biased above the breakdown voltage after irradiation (red color), iii) layout of one irradiated $3 \times 4\ mm^2$ die, which contains different $1 \times 1\ mm^2$ SiPMs.

excess bias and at 5 V below the breakdown voltage for all the technologies considered in this work. In particular, it can be observed that the increase of the leakage current becomes relevant starting at 10^{11} n_{eq/cm^2} in all the technologies, then it increases almost linearly. The NUV-HD SiPM with 40 μm cell pitch seems the one suffering the most from the radiation, likely due to the larger cell size, even though there does not seem to be a trend between the damage and the increase of the leakage current in the other SiPMs under test. Looking at the increase of the current ratio at 5V after the breakdown voltage, a linear trend between 10^9 n_{eq}/cm^2 and 10^{11} n_{eq}/cm^2 can be observed, whereas the trend is different at higher fluences. There seems to be a saturation effect starting at about 10^{12} n_{eq}/cm^2. From the figure we can see an increment up to three and four orders of magnitude in post-breakdown bias region at 10^{13} n_{eq}/cm^2.

Another method to assess the effect of the radiation in a SiPM can be the *damage parameter* α:

$$\alpha = \frac{\Delta I(V_{ex})}{\Phi V} \tag{3.2}$$

where ΔI is the increase of the dark current, Φ is the irradiation fluence

Technology	cell size [μm]	FF [%]	V_{bd} [V]	PDE_{pk} [nm]	V [m^3]
RGB-HD	20	66	28.5	535	3×10^{-7}
RGB-HD	25	72	28.5	535	7×10^{-7}
RGB-HD	30	78	28.5	535	5×10^{-7}
NUV-HD	30	78	28.8	420	7×10^{-7}
NUV-HD	35	80	28.8	420	1×10^{-6}
NUV-HD	40	81	28.8	420	1×10^{-6}
NUV-HD-RH	15	51	32.2	400	6×10^{-7}
RGB-UHD LF	10	68	34.4	535	7×10^{-8}
RGB-UHD LF	12.5	74	34.4	535	1×10^{-7}

Table 3.2: Summary of the key features of the tested SiPMs technologies, at $+20°C$.

and V is the depletion volume inside the detector. This equation assumes a linear correlation between current increase in the detector and fluence, without saturation or second order effects, thus assuming the defects generation into the bulk as not-correlated to each other. The value of α is supposed to be constant at different fluences, assuming there are no charge multiplication mechanisms. In the case of sensors with an internal amplification like the SiPMs, the parameter α cannot be directly compared with the one of the sensors without an internal gain. This is because the current includes the internal gain of the micro-cells and also because there are field enhancement effects in the deep levels, created by the proton irradiation. Thus, as a first approach, we have at least to divide α by the micro-cell gain. Here we used the current gain (G_c), representing the total number of carriers produced by a primary event and including also the effects of the correlated noise, as mentioned in the previous chapter.

In Fig.4.11 the damage parameter is plotted with and without the normalization by the current gain as a function of the cell dimension of the SiPMs, estimated at +20°C. The current gain was measured at 20°C on the not-irradiated SiPMs and used also for the irradiated samples, under the assumption of remaining constant with fluence, as will be proved in Sec.3.3.3. In the first plot there seems to be a trend with the cell dimension, likely due to the different current gain. The damage parameter normalized to the current gain does not show any specific trend between the damage parameter and the cell dimension. In fact, we only see one point lower than the others (i.e. 15μm cell). The differences in the obtained values of damage parameter might be statistical fluctuation in the damage or in the different effect

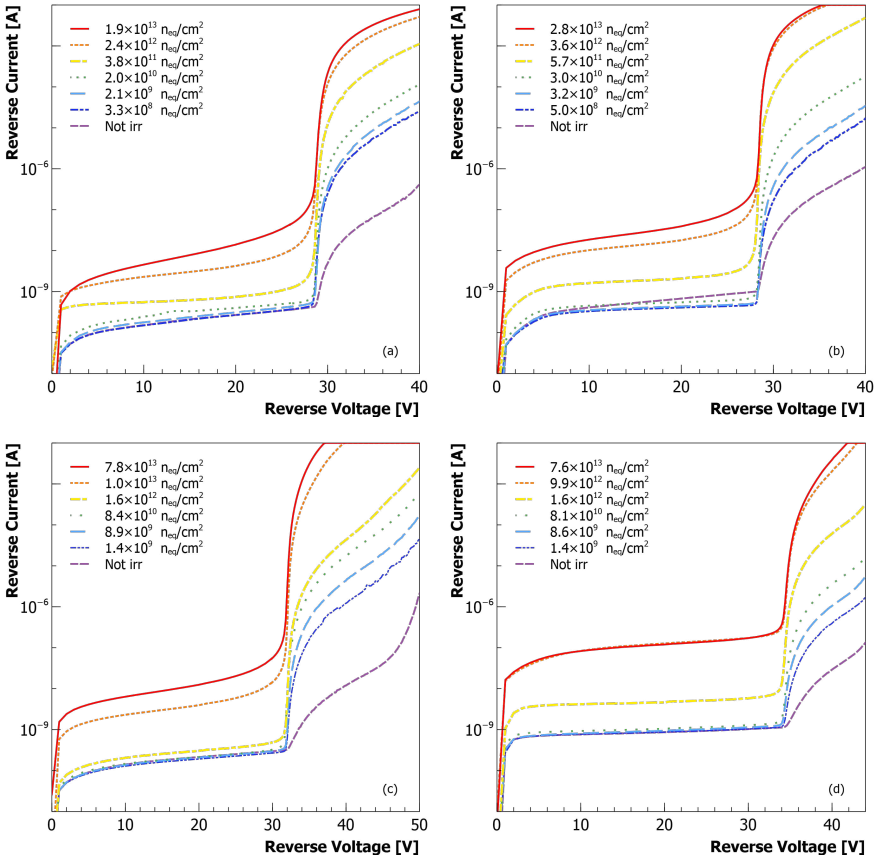

Figure 3.7: Current-voltage curve measured in dark conditions at room temperature $(20 \div 25)°C$ of NUV-HD SiPM with 35 μm cell pitch (a), RGB-HD SiPM with 25 μm cell pitch (b), NUV-HD-RH SiPM with 15 μm cell pitch (c) and RGB-UHD SiPM with 10 μm cell pitch (d) at different irradiation fluences.

of room temperature annealing. If compared to the ones typically obtained with fully-depleted silicon radiation sensors, e.g. [50], these results show a significant difference. In fact, the parameter α is typically at 5×10^{-17} Acm^{-2}, whereas in SiPMs, the parameter α divided by the current gain is about 2 order of magnitude higher. As mentioned before, the reason for such a higher value might be the high electric field in the multiplication region, which is necessary to work in Geiger-mode, resulting in a dark count rate enhancement (with respect to the pure Shockley-Read-Hall generation) through Poole-Frenkel effect and trap-assisted tunneling[67].

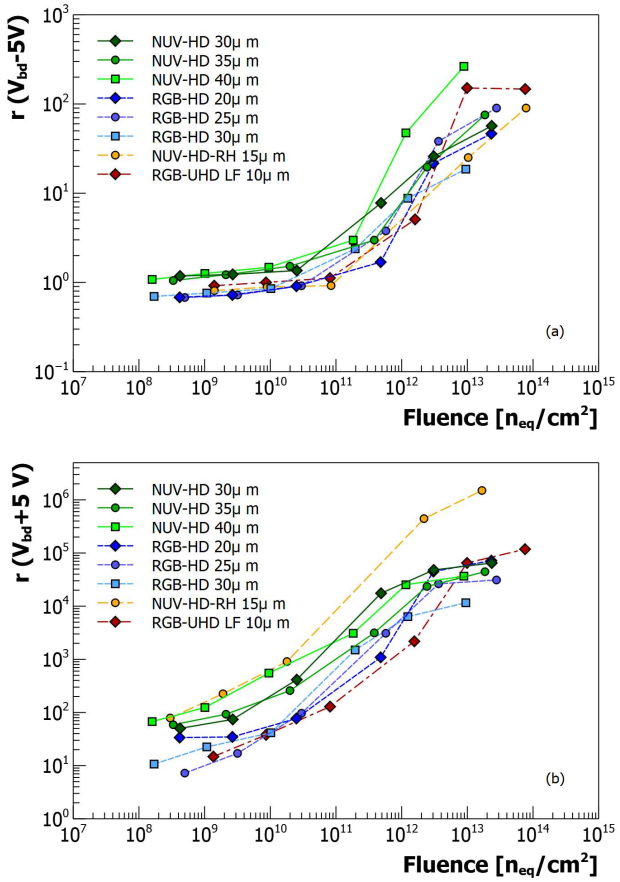

Figure 3.8: r parameter estimated at +20°C on the leakage current in pre-breakdown region at V_{OV}=-5 V and on the dark current at V_{OV}=5 V.

3.3.2 Breakdown Voltage

The breakdown voltage is one of the key parameters of a SiPM, it represents the reverse bias value where the multiplication factor diverges. The breakdown voltage is strictly dependent on the doping profile of the SiPM. Indeed, as visible in Tab.3.2, low field technologies compared to the standard technologies have an higher breakdown voltage.

V_{bd} of a SiPM is usually extracted from its reverse current-voltage curve. To do that, a clear separation between the features of the curve before and after the breakdown voltage is required. This is because the V_{bd} value can be altered when I_{leak} is comparable to I_{leak} at low over-voltage values (V_{bias}-V_{bd}), which could mean having a very high I_{leak} or a very low I_{dark}. In this case, it might be useful to expose the SiPM to a faint illumination and extract the V_{bd} under such conditions. A too intense illumination should be

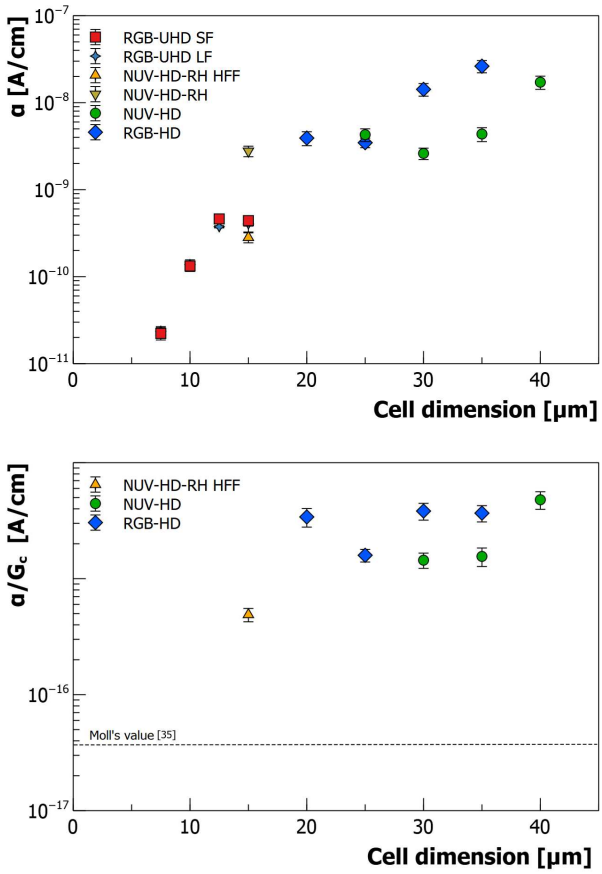

Figure 3.9: Damage parameter α plotted as a function of the cell dimension of the SiPMs, for SiPMs at $+20°C$, biased at 5 V excess bias voltage without any normalization (left) and normalized to the micro-cell gain (right).

avoided because part of the photo-generated carriers can be multiplied in the linear-multiplication regime (i.e. the one of the avalanche photodiode, APD, few volts below breakdown voltage), just before the breakdown, thus complicating the estimation of the breakdwon voltage, instead of simplifying it. Illumination should be high enough as to increase I_{dark} to distinguish it from $I_{leak)}$, which is assumed not affected by illumination.

In literature several methods can be found to estimate the breakdown voltage [68], [12], [6]. In this section several methods to estimate the breakdown voltage will be introduced and the results compared. The approaches which will be discussed below are based on the reverse I-V characteristic curve of the SiPM or the pulse-counting analysis. The methods are:

- the maximum of the First Logarithmic Derivative (FLD): V_{bd} is esti-

mated as the voltage corresponding to the maximum of the firstderivative of the Log(I) vs V curves, corresponding to the maximum slope point of the reverse current-voltage curve, with a logarithmic vertical axis

- the maximum of the Second Logarithmic Derivative (SLD): V_{bd} is estimated as the voltage corresponding to the maximum of the second derivative of the Log(I) vs V curves, corresponding to the inflection point of the reverse current-voltage curve, with a logarithmic vertical axis

- the minimum of the Inverse of the Logarithmic Derivative (ILD)[69]: V_{bd} is estimated from the minimum of the inverse of the first logarithmic derivative

- the maximum of the Normalized First Derivative (NFD)[70]: V_{bd} is estimated from the derivative of the "normalized current-voltage curve", which is the first derivative of the reverse current-voltage curve, normalized to the current value at each point

- in the waveform analysis (see Sec.1.3.1), breakdown voltage is estimated from a fit of the curve Amplitude vs. bias voltage, considering the point where the intercept crosses the bias axis (A)

- in the waveform analysis (see Sec.1.3.1), breakdown voltage is estimated from a fit of the first two points in the curve Gain vs. bias voltage, considering the point where the intercept crosses the bias axis (G_2)

- in the waveform analysis (see Sec.1.3.1), breakdown voltage is estimated from a fit of the curve Gain vs. bias voltage, considering the point where the intercept crosses the bias axis (G_{all})

The FLD and SLD methods are based on the fact that the gain of the SiPM micro-cells increases rapidly when the reverse bias is higher than the breakdown voltage, switching from a gain of a few thousands, in the linear multiplication regime, to a gain of a few hundreds thousand, in the Geiger regime, within a few hundred of mV. It should be pointed out that, because the gain in Geiger mode is proportional to the cell capacitance, thus to its area, the multiplied current I_{dark}, generated at the same level of DCR, is significantly higher for larger SiPM microcell sizes. As a consequence, these approaches might be less accurate for smaller cell sizes or when I_{leak} is particularly high compared to I_{dark} as discussed above.

The A, G_2 and G_{all} approaches are based on the measurements in pulse counting mode. In particular, with the pulse-amplitude method, we consider the peak amplitude of the SiPM single cell pulses, i.e. the signals generated when a single dark count triggers an avalanche, at different bias voltage values. The V_{bd} value represents the bias at which the linear extrapolation of the data intercepts the horizontal axis. In the G_{all} method, we employ a similar extrapolation based on the measured SiPM gain at different bias, while in the G_2 method the linear regression considers only the first two values of the gain measured at low excess bias. Regarding this latter approach, in some devices the gain-vs-bias curve might not be linear[12], thus it can be useful to take into account only the first two points of the curve, to avoid the part where the slope changes. In the case of non-irradiated SiPMs the SLD method[71], the A method and the G_2 methods are used. These usually results to be in good agreement but this might not be the case for irradiated samples.

In this work the reverse I-V characteristics curves were considered in both dark conditions and under moderate illumination. This latter condition was chosen because of the increase of I_{leak} due to the radiation damage which might lead to a incorrect distinction between pre and post breakdown current, resulting in a wrong estimation of the breakdown voltage, as discussed above. This might shift the V_{bd} estimated with SLD method to lower biases, but this is not supposed to happen with moderate light because of the significant increase of the current above the breakdown too. However, depending on the light intensity, SLD might be affected by the above mentioned increment of current in linear-multiplication regime.

A graphic comparison among the different methods for the NUV-HD SiPM with 35 μm cell pitch is provided in Fig.3.10, where the light and dark breakdown voltage estimations are shown as a function of the irradiation fluence at -20°C. In dark conditions, we can notice a spread among the methods consistent with the uncertainty bars. On the contrary, when using moderate light (420nm LED), smaller variation values were found. Indeed, the standard deviation among the several fluences for each method is much lower under illumination than in dark conditions. Among the approaches based on the derivatives, the standard deviation results smaller in the FLD method, while it is higher in the SLD case. Since the reverse I-V characteristic curves do not rise as steep as in the ideal case, the voltage at the second derivative of each curve differs from the one at the first derivative. For this reason, the SLD method always provides lower values than the others, whereas the methods based on the first derivative seem to be fairly similar. Due to the difficulty in estimating the amplitude and gain of the irradiated samples (as described in detail in the next section), the V_{bd} values obtained

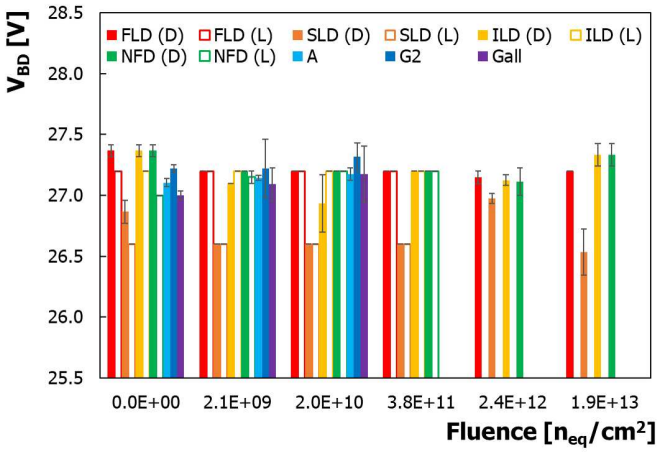

Figure 3.10: Example of estimated breakdown voltage values for the NUV-HD SiPM with 35μm cell pitch, obtained with the different estimation methods in dark (D) and light (L) conditions at -20°C. Error bars identify the spread of values obtained among repeated measurements.

with these approaches have some fluctuations, especially in the estimation from the gain. Specifically, in the NUV-HD SiPM with 35μm cell pitch, the pulsed-light method remains efficient only up to 10^{11} n_{eq}/cm^2.

Considering the uncertainties and the differences among the methods, it is not possible to observe a clear trend in the estimated breakdown voltage as a function of the fluence. We can therefore consider that the irradiation up to 10^{14} n_{eq}/cm^2 does not affect significantly the implants doping concentration in the p/n junction of the SPADs, i.e. in the high-filed region.

3.3.3 Current Gain

To study possible variations of the gain and the correlated noise, which are not measurable directly with the pulse-counting method in highly irradiated samples due to their high noise, we measured the "current gain" G_c. This is the product of two factors: the excess charge factor (ECF) and the micro-cell gain (G). To study the current gain of the irradiated SiPMs the average charge was measured, obtained as a response of the SiPM to a calibrated light pulse. A 420nm LED operating in pulse mode was used. Light was injected into an optic fiber, reaching the SiPM placed inside a thermostatic chamber, settled at -20°C. The SiPM was connected to a two-stage trans-impedance amplifier, with a 5000 V/A gain and a 30 input impedance. Thus, the signal was amplified in a first stage, then read out by a digitizing oscilloscope (Keysight, 10 GSa/s, 1GHz bandwidth). The signals from several LED

pulses were measured and averaged. A dark count signal was also recorded and then subtracted to the signal. The total charge (expressed in electrons) was derived from the formula:

$$< Q > (V_{ex}) = \frac{1}{q} \frac{< Q_L > (V_{ex}) - < Q_D > (V_{ex})}{G_{ampli}} \tag{3.3}$$

where $< Q_L > - < Q_D >$ is the integral of the net signal (dark signal subtracted) and G_{ampli} is the trans-impedance gain of the amplifier corresponding to 5000 V/A. The number of photons was estimated using the not-irradiated SiPM, by taking into account the detection efficiency and the Current Gain:

$$n_{ph} = \frac{< Q > (V_{ex})}{PDE(V_{ex}) \times G_c(V_{ex})} \tag{3.4}$$

The current flowing through the device in dark conditions can be simply obtained by multiplying the DCR by the "Current Gain" and the electron charge. The number of photons at the several fluence levels under consideration up to 10^{11} n_{eq}/cm^2 was observed not being subjected to variations. As a consequence, the product $PDE(V_{ex}) \times G_c(V_{ex})$ results constant until 10^{11} n_{eq}/cm^2 as well. PDE was verified not changing with irradiation dose up to 10^{10} n_{eq}/cm^2 at least, through a direct measurement (see Sec.3.3.5) and, although this might result inaccurate, it was assumed constant up to 10^{11} n_{eq}/cm^2, otherwise this would imply a compensation in the G_c and PDE variations. Thus, after estimating n_{ph}, the current gain of the irradiated SiPMs was estimated through the Eq.3.4 at different irradiation fluences up to 10^{11} n_{eq}/cm^2.

In Fig.3.11 the results of the Current Gain measured with the pulse counting method on the not-irradiated SiPMs are shown, compared to the Current Gain estimated by the average-signal method, described above, up to 10^{11} n_{eq}/cm^2. It can be observed that the results are in agreement inside the uncertainty range, indicating that overall the PDE and the Current Gain values of the SiPMs do not change significantly with irradiation, at least in the investigated fluence range.

3.3.4 Noise

A direct measurement of the DCR on irradiated SiPMs is not straightforward because of the difficulty in identifying single pulses, necessary to extract the amplitude and inter-arrival times needed for using the approach described in [18]. In this section two approaches to the DCR estimation will be described: the first is based on the increase of the dark current (D.C.

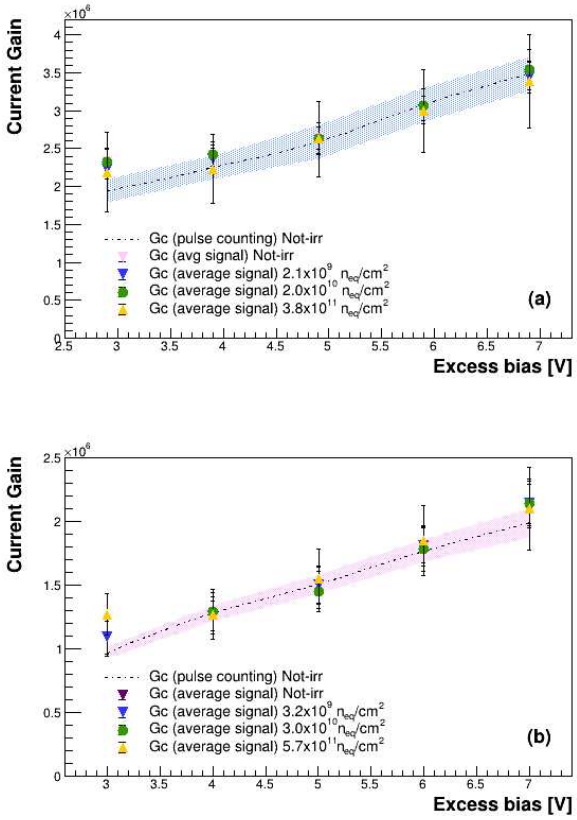

Figure 3.11: Current Gain measured directly with pulse counting method, compared to the Current Gain estimated by the average-signal method, for different SiPMs with different irradiation fluences, for the NUV-HD SiPM with 35μm cell pitch (a) and RGB-HD SiPM with 25μm cell pitch (b). The coloured error band in each graph refers to the one measured directly with pulse counting method, the error bars refer to the average signal method.

method) identified by the r parameter described above, the second is based on the pulse-identification analysis (P.I. method) where the amplitude and the inter-arrival time of the pulses are extracted and then analyzed[18].

In the D.C. method, the DCR can be estimated as:

$$DCR(V_{ex}) = \frac{I_{dark}(V_{ex})}{q \times G(V_{ex}) \times ECF(V_{ex})} = \frac{1}{q}\frac{I_{dark}(V_{ex})}{G_c(V_{ex})} \tag{3.5}$$

As shown by Eq.3.5, G_c can be used to estimate the primary, Poisson-distributed DCR from the reverse I-V measured on the SiPMs. In this case, the DCR and the ECF cannot be calculated independently, thus both the ECF and the Current Gain were supposed constant, as verified in the previous

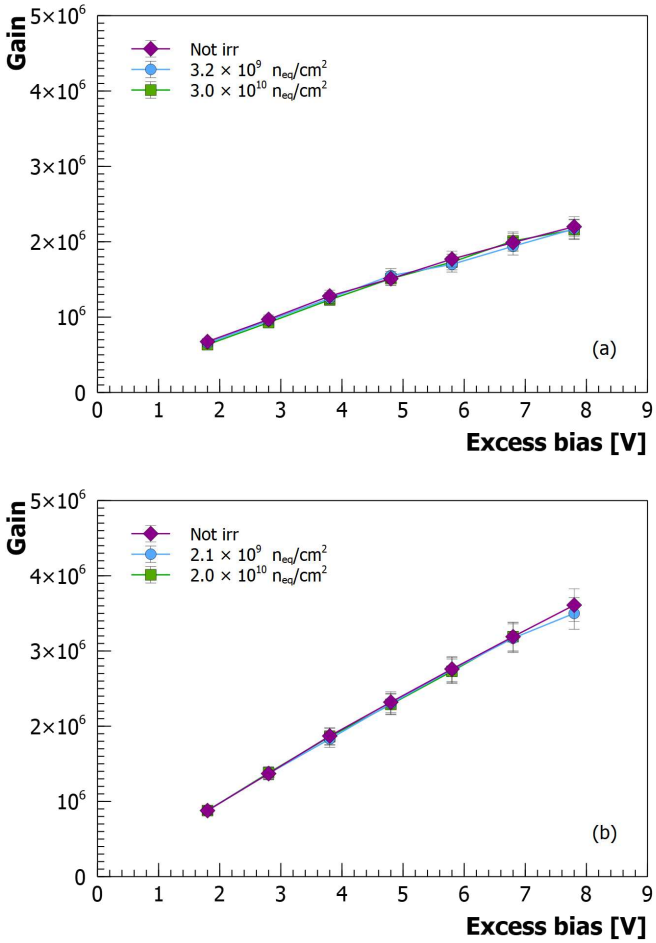

Figure 3.12: Gain of the RGB-HD SiPM with 25μm cell pitch (a) and NUV-HD SiPM with 35μm cell pitch (b) at two fluence levels.

section, at least up to 10^{11} n_{eq}/cm^2. This hypothesis is partially confirmed by the measure of the Gain of the SiPMS with the pulse-counting method, which remains constant for all the SiPM tested up to 10^{10} n_{eq}/cm^2 at least, as showed in Fig.3.12 for the RGB-HD and the NUV-HD SiPMs.

Therefore, assuming that G_c does not change with fluence, which is a reasonable assumption until 10^{11} n_{eq}/cm^2 at least as already observed in the previous section, using Eq.3.5 we get:

$$\frac{DCR_{\phi}(V_{ex})}{DCR_{\phi_0}(V_{ex})} = \frac{I_{\phi}(V_{ex})}{I_{\phi_0}(V_{ex})} = r(V_{ex}) \tag{3.6}$$

where ϕ_0 indicates the non-irradiated sample.

This method resulted to be very useful in high fluence conditions, where the noise may increase too high for an accurate distinction between signal and noise.

In the pulse-identification (P.I.) method the amplitude of the pulses is estimated and plotted as a function of the inter-arrival time. In this way primary events can be separated from correlated noise, obtaining the primary DCR.

Fig.3.13 shows the DCR for the NUV-HD technology obtained with both the described methods. Considering the uncertainty range, a good agreement between the results with the two methods can be noticed, at least up to 10^{10} n_{eq}/cm^2, which represents the limit for the pulse counting method in this specific technology. The DCR plot as a function of the fluence provides an accurate comparison of the noise among different SiPMs and different technologies. It can be observed that SiPMs with a higher DCR before irradiation show a smaller overall increment of noise because of irradiation. Despite the DCR starting level, the curves of DCR vs fluence seem to converge toward similar values.

The correlated noise in SiPMs is represented by direct cross-talk, delayed cross-talk and afterpulsing (given by traps or optically-induced). These are usually estimated separately, but for simplicity here the sum of their probabilities will be considered. The correlated noise was measured with the pulse-identification method, for this reason even in this case results are referred only to the lowest fluences. The results of the RGB-HD SiPM and the NUV-HD-RH SiPMs are visible in Fig.3.15, where a quite coherent trend at all the fluences considered can be observed. It would be interesting to know if this consistency is still valid for higher fluences, but a new measurement method needs to be investigated.

In particular, the DiCT shows the most interesting results, especially when the total noise gets very high. In fact, it is possible that two DCR events get closer than the minimum inter-time interval resolvable by the acquisition system. In this case, the two events are read as a single event with a double amplitude, which correspond to a DiCT event. In this way DiCT might result overestimated. The probability of such phenomenon increases as the DCR increases, thus it is very common in highly irradiated SiPMs. On the other hand, the probability decreases with increasing bandwidth of the acquisition system. The acquisition system used for the measure of the DiCT in this work uses an analog bandwidth of 1 GHz and the DLED algorithm [21] to improve the peak-finding capabilities and to reduce the effects of the pile-up of subsequent pulses. To solve the overestimation of the DiCT, a correction factor was introduced in [72]. In this work, a minor modification was also introduced, in fact the non-corrected cross-talk was calculated as the ratio of

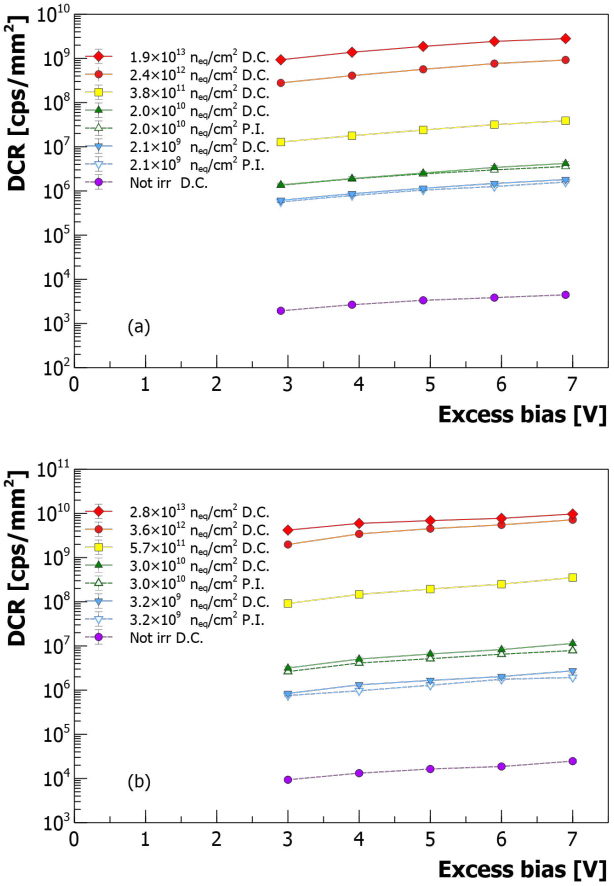

Figure 3.13: DCR as a function of the applied voltage estimated with the two methods (i.e. D.C. and P.I. methods) for the NUV-HD SiPM with 35μm cell pitch (a) and the RGB-HD SiPM with 25μm cell pitch (b).

the count rate of the 2 p.e. peak (i.e. events between 1.5 p.e. and 2.5 p.e.) over the count rate of the 1 p.e. peak (i.e. events between 0.5 p.e. and 1.5 p.e.), as reported in [39].

The resulting equation for the corrected DiCT is:

$$p_{CT} = 1 - \left[1 - \frac{P_{2p.e.}}{P_{1p.e.}}\right] \times e^{DCR_{0.5} \times \tau} \tag{3.7}$$

where τ is the minimum inter-arrival time that can be resolved by the acquisition system and $DCR_{0.5}$ represents the total DCR, measured with a 0.5 p.e. threshold level. In Fig.3.16 a comparison between the corrected and the not-corrected DiCT are visible for the NUV-HD-RH technology with

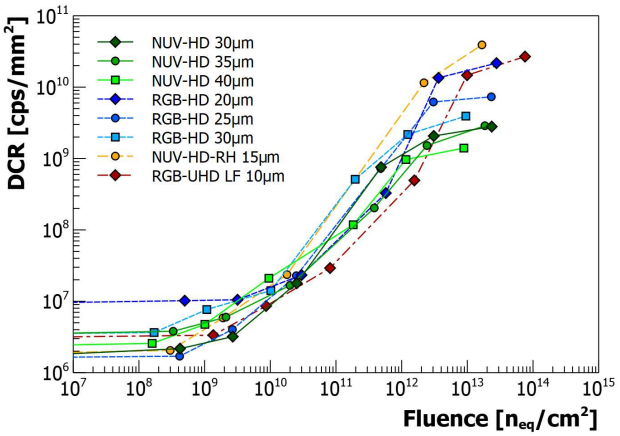

Figure 3.14: Estimated primary dark count rate (DCR) as function of the fluence at 5V of excess bias

15μm cell pitch and the NUV-HD SiPM with a 35μm cell pitch. A significant improvement of the DiCT estimation accuracy can be observed in the NUV-HD-RH especially at high fluences, showing a DiCT constant with fluence at least up to 10^{10} n_{eq}/cm^2, while no remarkable effects were identified in the other technologies tested.

3.3.5 PDE

The standard PDE measurement method in FBK is described in detail in [73]. The SiPM is exposed to a pulsed-light and the number of synchronous, calibrated, pulsed light and dark count events within a certain time window are detected.

PDE value is estimated as[73]:

$$PDE(V_{ex}) = \frac{N_L - N_D}{(I_L^{REF} - I_D^{REF}) \times L_{cal}} \tag{3.8}$$

where N_D is the number of events, generated in dark conditions, within the time window, whereas N_L is the number of events generated in light conditions in the same time window. In particular, N_L represents the sum of light and dark counts. N_D and N_L are estimated through a Poissonian statistics, not considering the correlated noise. I_L^{REF} and I_D^{REF} are the current of the reference diode in light and dark conditions respectively, whereas L_{cal} is the calibration factor depending on the geometry of the setup and the area of the SiPM.

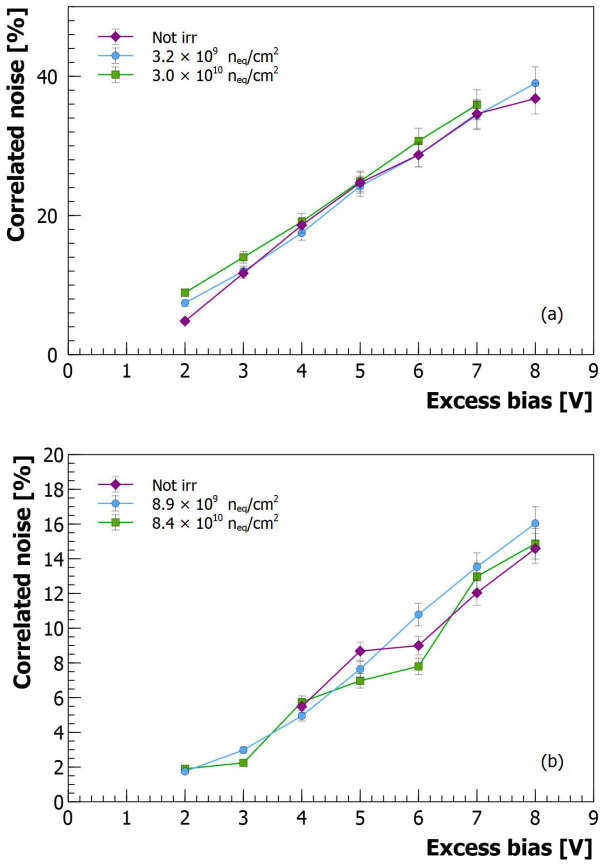

Figure 3.15: Correlated noise of the RGB-HD SiPM SiPM with 25μm cell pitch (a) and NUV-HD-RH SiPM with 15μm cell pitch (b) at two fluence levels.

Even for the PDE, as well as for the noise, a direct measure is not straightforward, due to the high number of noise pulses in the time window, making the value of N_D comparable to N_L and as a consequence introducing a not negligible error in the numerator in Eq.3.8. In particular, this approach resulted to be efficient at room temperature (20÷25°C) until 10^{10} n_{eq}/cm^2.

The main results for the NUV-HD and RGB-HD technologies are visible in Fig.3.17, where PDE is plotted as a function of the excess bias up to the maximum fluence which guarantees a good accuracy of this method, in the order of 10^{10} n_{eq}/cm^2. From the figures, no significant changes with irradiation are observed. At high excess bias values, this accuracy seem to get worse, especially in the RGB-HD technology, but this is mainly due to the increase of the DCR when the cell occupancy increases considerably.

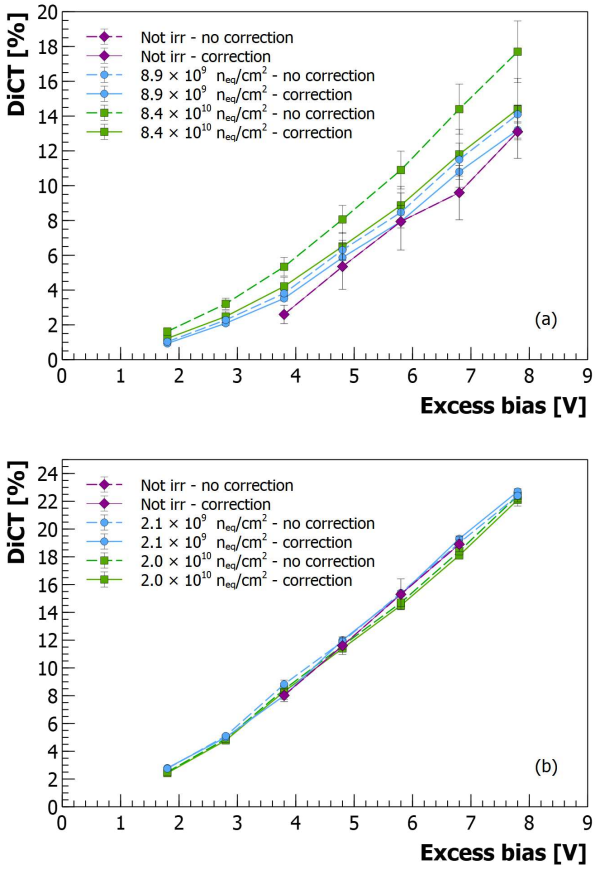

Figure 3.16: DiCT with and without the correction factor for the NUV-HD-RH SiPM with 15μm cell pitch (a) and NUV-HD SiPM with 35μm cell pitch (b).

An alternative approach to evaluate possible variations in the PDE is the measurement of the *Responsivity* in current mode which is calculated through the following equation:

$$R(V_{ex}) = \frac{I_L^{DUT}(V_{ex}) - I_D^{DUT}(V_{ex})}{W_{opt}} = \frac{I_L^{DUT}(V_{ex}) - I_D^{DUT}(V_{ex})}{\phi_{ph} \times q \times E_{ph}(\lambda)} \tag{3.9}$$

where I_L^{DUT} and I_D^{DUT} is the photo-current read on the SiPM in light and dark conditions respectively. W_{opt} represents the optical power of the light, and it depends on the number of photons per seconds that reach the SiPM and their energy. SiPMs are illuminated with a LED, in this measurement a 420nm LED was used. The optical power was determined using the reference

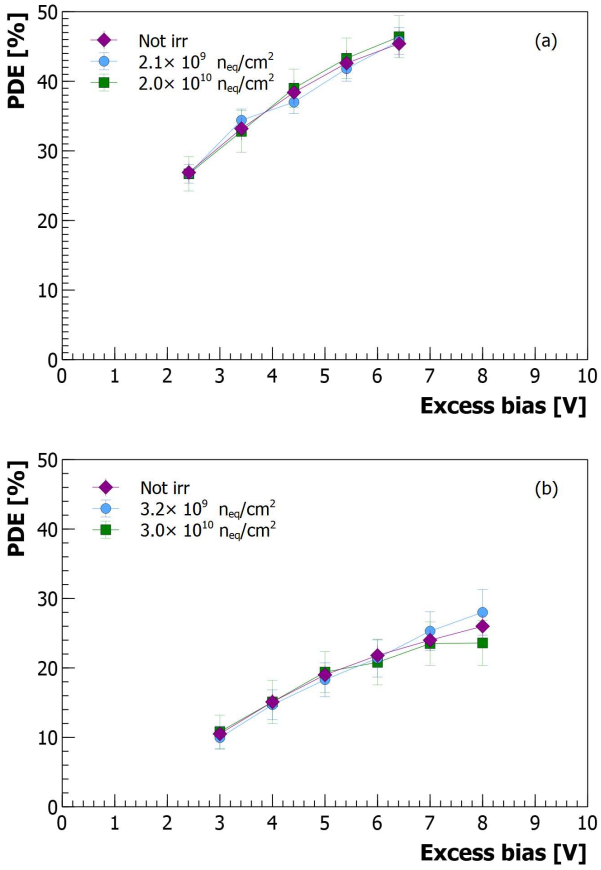

Figure 3.17: PDE plots for the NUV-HD SiPM with 35 μm cell pitch (a) and the RGB-HD SiPM with 25 μm cell pitch (b), measured on non-irradiated and two irradiated devices under a 420nm LED light, at $+20°C$.

diode currents (in dark and light conditions), multiplied by the calibration factor and by the elementary electron charge, as already observed in the previous method for the estimation of the PDE.

The main results of this approach for the RGB-HD and the NUV-HD technologies are visible in Fig.3.18. No significant changes are observed until 10^{11} n_{eq}/cm^2, whereas at higher fluences the responsivity (thus the PDE) is reduced by the increase of the cell occupancy by DCR, resulting in saturation effects.

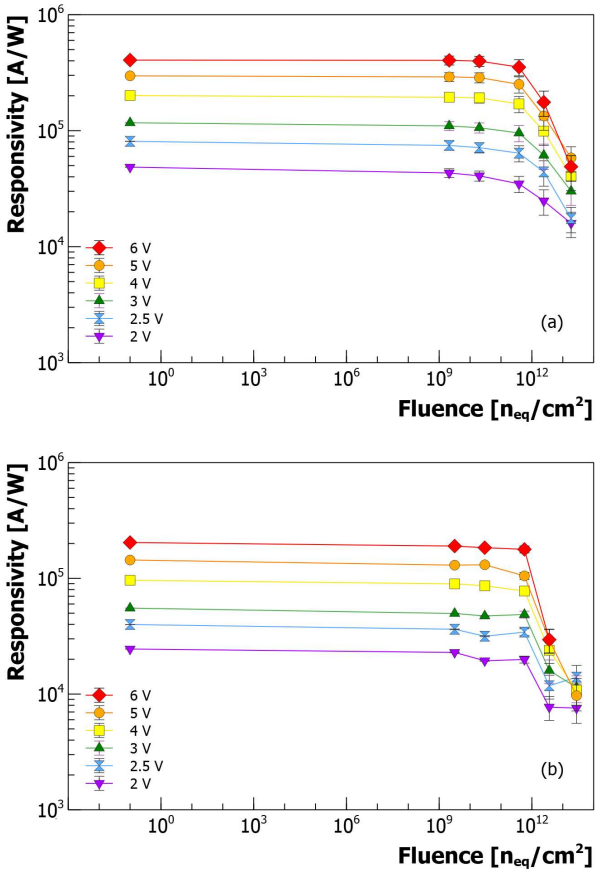

Figure 3.18: Plots of the Responsivity as a function of the protons fluence, for the NUV-HD SiPM with 35 μm cell pitch (a) and the RGB-HD SiPM with 25 μm cell pitch (b) at $+20°C$ and at several excess bias values.

3.3.6 Activation Energy

The SiPMs were placed in a thermostatic chamber and characterized at different temperatures to observe the effect of the temperature on their main parameters. In particular, the reverse current-voltage curves were extracted and they were compared at a fixed excess bias value, taking into account the dependence of the breakdown voltage on the temperature which results in a shift at each temperature step. Then, the reverse current at a given excess bias was plotted as a function of the inverse of the temperature in an interval $-50 \div 35°$C, as shown in Fig.3.19. At this point the slope of the curve in the thermal generation interval (in this case the range -15°C and +15°C was chosen to ensure a good linearity) was extracted to obtain the *activation energy* E_a. The thermal generation interval was chosen considering that

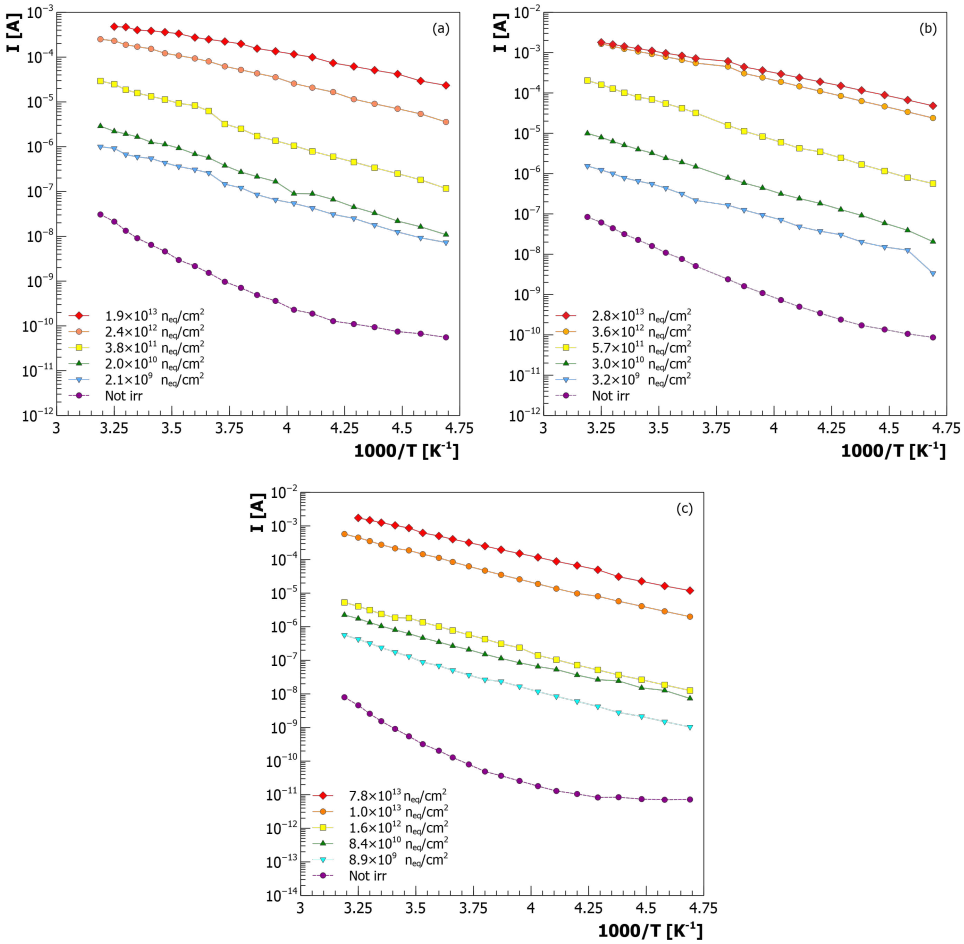

Figure 3.19: Reverse current as function of 1000/T for the NUV-HD with 35μm cell pitch (a), RGB-HD with 25μm cell pitch (b) and NUV-HD-RH with 15μm cell pitch (c) technologies.

the DCR generation is dominated by the field-enhanced SRH mechanism at room temperature, as visible in Fig.1.20. E_a is a key parameter to obtain an accurate interpretation of the microscopic effects of the damage inside the SiPM. Usually, when the DCR of the SiPMs is dominated by thermal generation , i.e. Shockley-Read-Hall recombination processes, it can be useful to extract the temperature dependence of the current generation and particularly the activation energy of the generation process. In this case it would be also useful to verify any possible variations of such activation energy as a function of the irradiation fluence.

The dark current has an Arrhenius-like dependence on the temperature described by the relation:

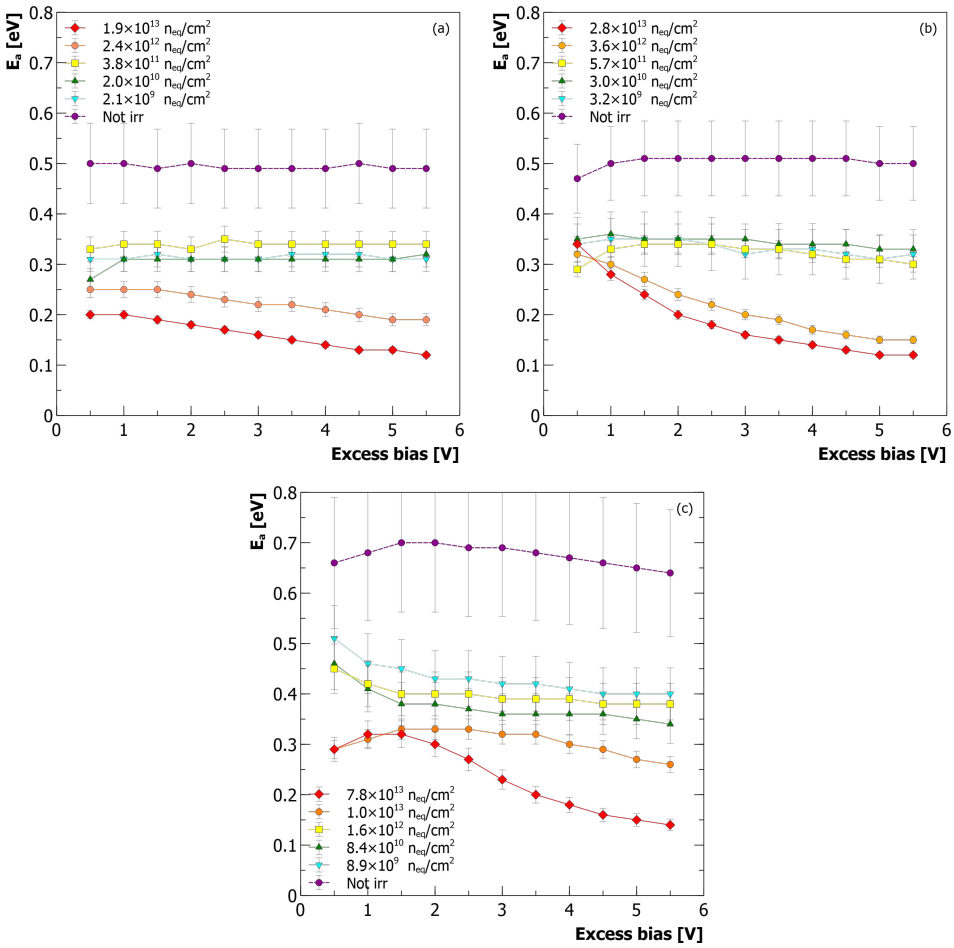

Figure 3.20: Activation energy (Ea) as function of the excess bias for the NUV-HD with 35μm cell pitch (a), RGB-HD with 25μm cell pitch (b) and NUV-HD-RH with 15μm cell pitch (c) technologies.

$$I(T) = I_0 e^{-\frac{E_a}{kT}} \tag{3.10}$$

The results of the estimation of the activation energy extracted from a fit of the reverse current as a function of the temperature is visible in Fig.3.20, where E_a is plotted as a function of the excess bias for the NUV-HD with 35μm cell pitch, RGB-HD with 25μm cell pitch and NUV-HD-RH with 15μm cell pitch SiPMs. A fictitious decrease of E_a is clearly visible. This might be due to some saturation effects (due to the high cell occupancy) at the highest fluence levels, starting at 10^{12} n_{eq}/cm^2. In this case, the DCR increase undergoes a non-linear saturation process providing a fictitious and lower

value of the effective DCR increase. An alternative hypothesis about the behaviour of E_a could be the introduction of new defects strongly dependent on the bias voltage. Since saturation effects were already observed in the DCR estimation in Sec.3.3.4, the assumption of having a new kind of defects can be considered as more unlikely than the one about saturation effects.

Assuming the E_a behaviour as due to saturation effects, in Fig.3.20 the beginning of the saturation is perfectly visible in the NUV-HD SiPM with 35μm cell pitch at 1 OV, and the decrease of the E_a with the fluence can be clearly observed. In the RGB-HD and NUV-HD-RH technologies the saturation effects are evident but it cannot be said with a good accuracy at which excess bias value they start. In particular, RGB-HD technology appears to have an earlier saturation than the NUV-HD, as visible in Fig.3.20. This might be due to a more significant damage in the RGB-HD technology, or to their higher DCR. In fact, in Fig.3.19 the RGB-HD SiPM reaches higher current values than the NUV-HD at similar fluences.

In the NUV-HD technology, at least two E_a levels can be outlined at fixed excess bias, apart from the saturated curves at high fluences. This means that the activation energy suffers a decrease from its value in the non-irradiated SiPMs (i.e. $0.5 \div 0.65$ eV) as a consequence of the radiation damage. In fact, at 10^{11} n_{eq}/cm^2 the activation energy results to be in a range $0.35 \div 0.4$ eV. These results have not been fully understood yet, but this behaviour might suggest the generation of some additional energy levels, lowering the activation energy from around mid-gap (i.e. around 0.6 eV) to a lower value, around 0.3 eV. This might be possibly due to the creation of vacancies and interstitial atoms due to the radiation effects.

A gradual decrease of E_a is well shown even in Fig.3.21, where it is plotted as a function of the fluence at 2V of excess bias and the saturation effects become more evident, starting at 10^{12} n_{eq}/cm^2, even at low over-voltage values (2OV), revealing an almost complete saturation at 10^{13} n_{eq}/cm^2.

3.3.7 Emission Microscopy

Emission microscopy (EMMI) technique, which was previously introduced in Ch.1, was used on the irradiated SiPMs assuming that the enhanced-light regions (hotspots) correspond to the regions where most likely a noise avalanche pulse is generated. Fig.3.22 and Fig.3.23 show a representation of EMMI images of a section of NUV-HD SiPM with 35μm cell pitch and the RGB-HD SiPM with 25μm cell pitch respectively, irradiated at 10^{12} n_{eq}/cm^2.

EMMI images were used to search for a preferred spatial localization of the enhanced light emission regions into the single microcells of the SiPM. The image was considered as a matrix of intensity points $I_{i,j}$ and an ellipse

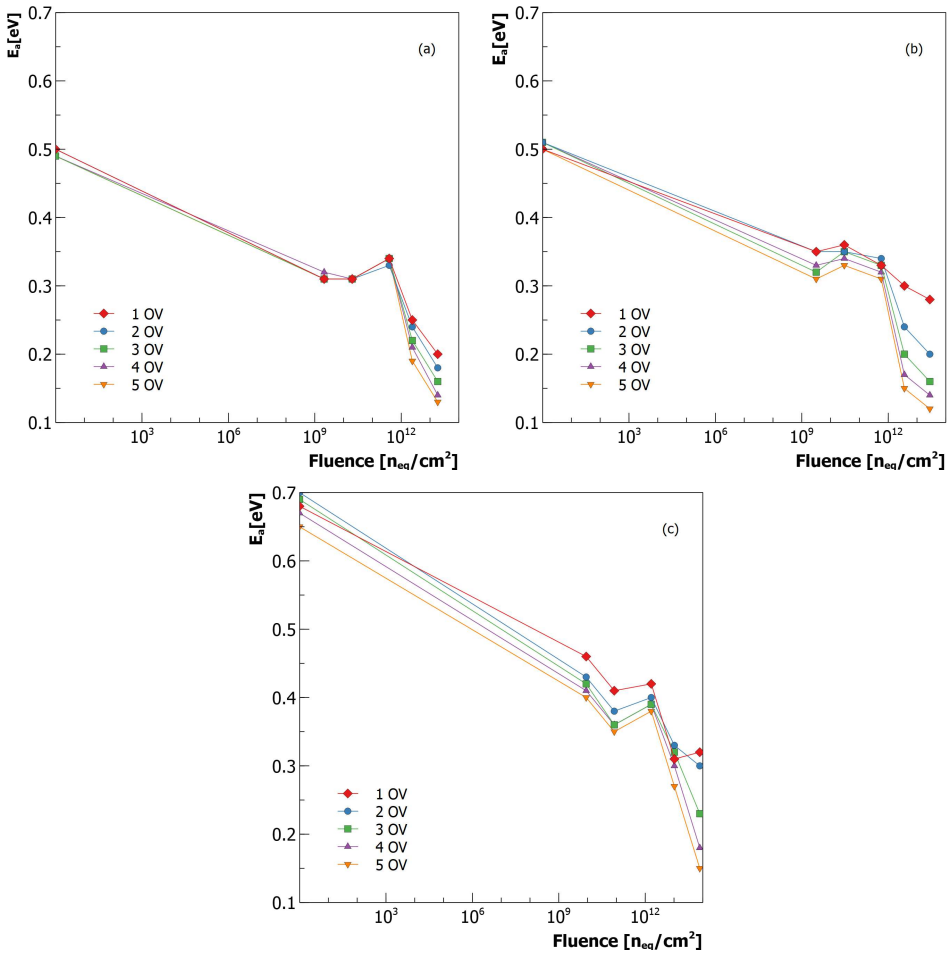

Figure 3.21: E_a as a function of the Φ for the NUV-HD with 35μm cell pitch (a), RGB-HD with 25μm cell pitch (b) and NUV-HD-RH with 15μm cell pitch (c) technologies.

was generated in the center of each microcell of the SiPM to differentiate between the border and the center. Then, an intensity threshold I_{th} was set and the high intensity points in the internal and external region $I_{i,j} \geq I_{th}$ were counted.

$$N_{points} = \sum n_{points}$$

with $I_{i,j} \geq I_{th}$(3.11)
The same procedure was applied setting different intensity thresholds and

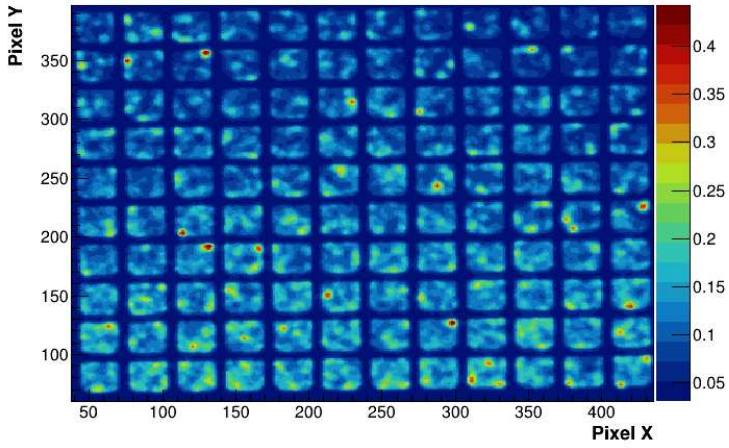

Figure 3.22: EMMI capture of the NUV-HD SiPM with 35μm cell pitch, fed at 2.5V excess bias with a zoom on a low number of cells.

ellipse sizes. The main purpose of this approach was to make a preliminary statistic of the spatial localization of the enhanced light regions for different light intensities, without taking into account the dimension of the hotspots. The results of the counting of the points outside the ellipse for the NUV-HD SiPM with 35μm cell pitch at 2.5V of excess bias are plotted in Fig.3.24 as a function of the intensity threshold, assuming that the region outside the ellipse corresponds to the border of the microcell. In particular, the dashed lines represent the ideal situation in case of equally distributed hotspots all over the cell area. A preferred spatial localization of the high-emission points on the borders of the microcells can be observed in the plot at high intensity threshold. On the contrary, a rather uniform distribution of the light regions over the entire cell was observed at low I_{th} which probably is not highly relevant, as it mainly represents the background light. A statistic of the enhanced light regions on the four corners of the microcell on the NUV-HD SiPM with 35μm cell pitch was also performed and the results are shown in Fig.3.25, where the hotspots appear to have a preference for the top-right corner at high intensity thresholds.

This should be considered as a very preliminary result which will hopefully lead to a full characterization of the spatial localization of the hotspots inside the microcell.

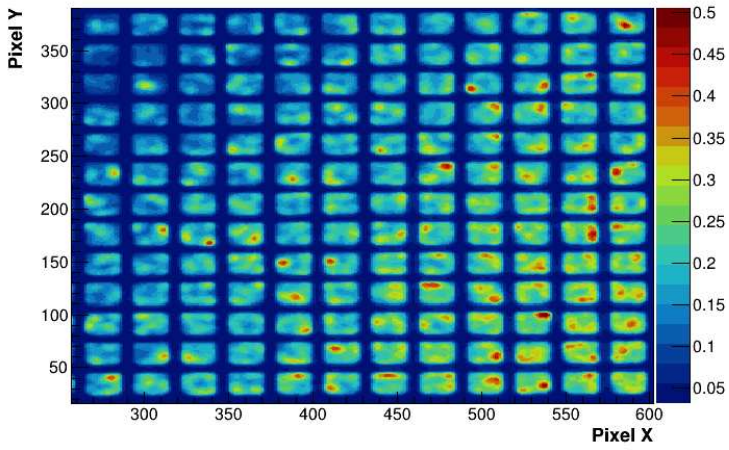

Figure 3.23: EMMI capture of the RGB-HD SiPM with 30μm cell pitch, fed at 3.5V excess bias with a zoom on a low number of cells.

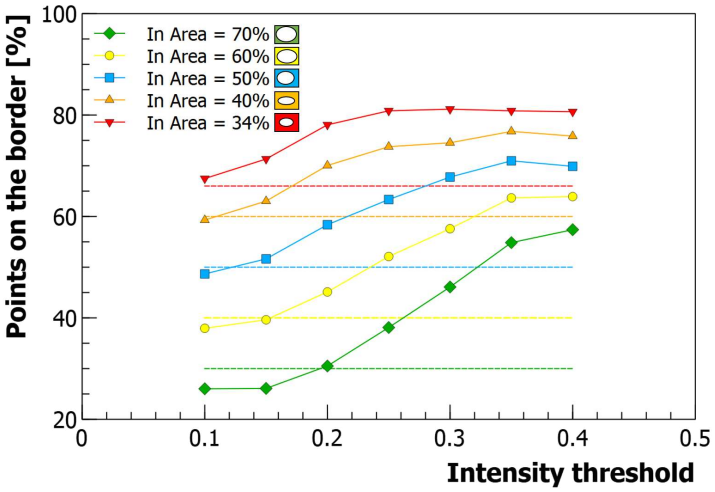

Figure 3.24: Plot of the points on the borders of the cell of the NUV-HD SiPM with 35μm cell pitch at 2.5V of excess bias. The dashed lines represent the values it would take if the points were equally-distributed inside the cell.

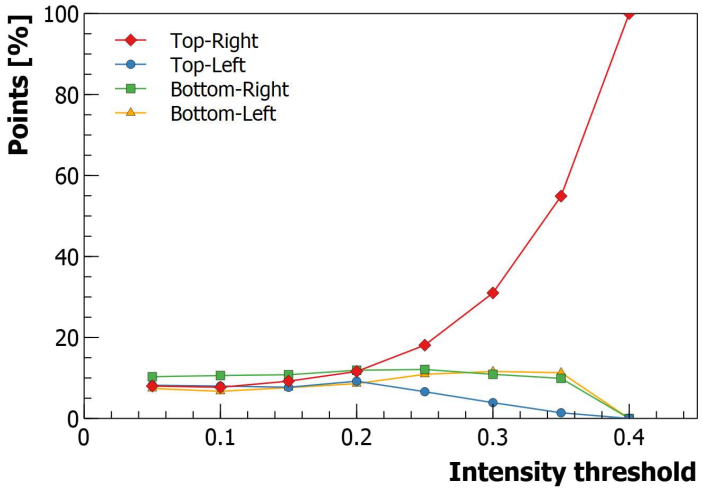

Figure 3.25: Percentage of the points distributed on the four angles of the cell of the NUV-HD SiPM with 35μm cell pitch at 2.5V of excess bias as function of the intensity threshold.

Chapter 4

Proton irradiation tests at Trento Proton Therapy Center

In this chapter, a SiPMs irradiation test at Trento Proton Therapy Center will be described. Differently from the irradiation test described in the previous chapter, this will be mainly focused on a radiation damage evaluation of SiPMs for space-satellite applications. In fact, there is only a handful satellites using SiPMs at the moment mainly due to the high radiation tolerance required to survive to the high level of radiations in space. For this reason, a preliminary characterization of SiPMs for this purpose is useful for future improvements and new applications. Moreover, this irradiation test will involve an online measurement of the SiPMs performance and a 30-days annealing process.

4.1 Trento Protontherapy Center

The Trento Proton Therapy Center was born as a facility for medical treatment in 2014. The facility has a double purpose, as it is equipped with an experimental area dedicated to scientific applications.

The experimental room is equipped with two proton beam lines, one for physics research and one for biology research, as visible in Fig.4.1. The apparatus consists of a cyclotron that accelerates the beam up to a maximum energy of 228 MeV. The minimum energy is set to 70 MeV, accessible through a rotating degrader with different thickness and materials placed at the cyclotron exit. Different beam intensities (currents) can be set at the cyclotron exit, between 1 and 300 nA. An ionization chamber is usually inserted in the beam line between the cyclotron exit and the Energy Selection System (ESS) which enables to set the beam energy. The current value is

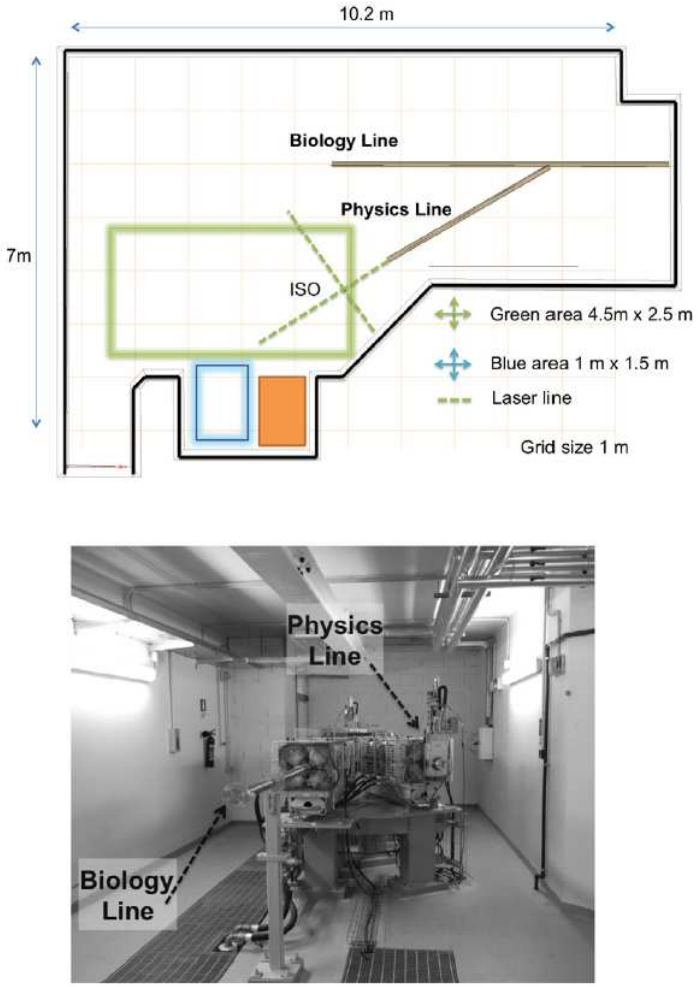

Figure 4.1: A picture (upper panel) and a schematic view (lower panel) of the experimental room at the Trento Proton Therapy centre[74].

measured by the total amount of charge collected by the ionization chamber. The beam is switched in one of the two lines through a dipole magnet placed at the entrance of the experimental cave.

The two proton lines differ in the beam profile and its size. The first one, called *physics line* features a gaussian beam shape, whose profile as a function of the energy has been described in detail in [74] and a graphic view of the results is visible in Fig.4.2 at different protons energy.

In the irradiation test described in this chapter, the *biology line* was used, featuring a higher uniformity in the irradiation intensity over an area of few centimeters than the physics line. This allows to have a larger beam spot, of approximately 5 cm. This is made possible by a dual-ring scattering system

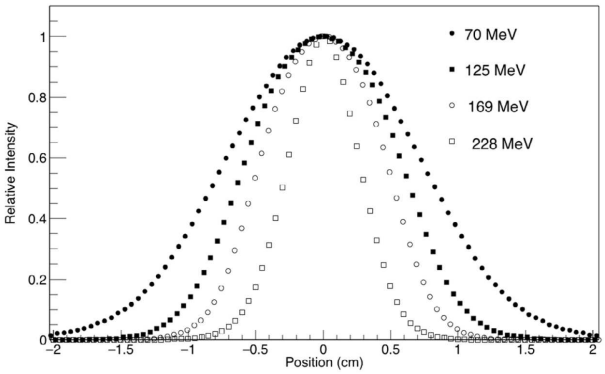

Figure 4.2: Gaussian beam profile at several energy values[74].

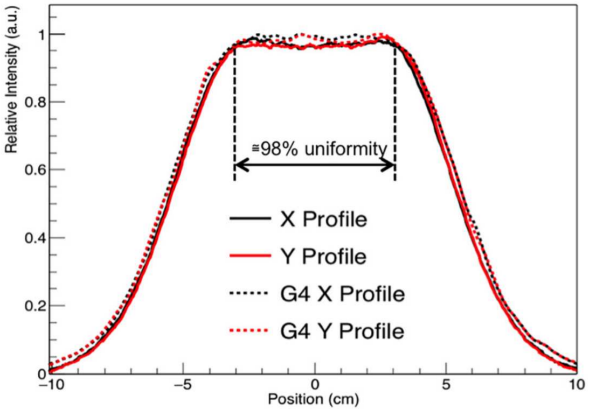

Figure 4.3: x-y profile of the beam from the dual-ring scattering system extracted at the center of the field[75].

and an energy 3D modulator resulting into an extended spread-out Bragg peak (SOBP) of 2.5 cm[75]. The beam is first enlarged by a scattering foil with a high atomic number, than there is an inner circular region surrounded by a ring structure which represents a second scattering structure. The two structures have different scattering power but same water-equivalent thickness. The combination of the two elements form the dual-ring structure[75]. The x-y profile of the beam from the dual-ring system is shown in Fig.4.3, where a uniformity of approximately 98% is obtained in the the center of the beam. The setup was further modified during this irradiation test by adding a few RW3 layers in between the dual-ring and the SiPMs, to lower the proton beam energy to 74 MeV. This modification was measured and considered as having a minor impact on the shape of the beam profile.

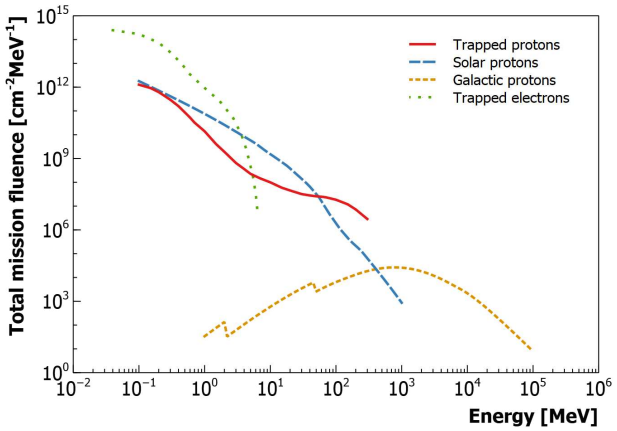

Figure 4.4: Output plot from SPENVIS software showing the total mission differential fluence as a function of the energy of trapped, solar, galactic protons and trapped electrons, along a circular polar LEO (550 km - 97°).

4.2 Fluence estimation

In this work, different types of SiPMs have been tested to obtain a preliminary characterization for future space applications. To this purpose, a typical orbit for satellites was chosen: a 550 km altitude and 97° inclination circular Low Earth Orbit (LEO), Polar[76].

The expected fluence along this orbit was estimated through the use of SPENVIS software[77], which provides the spectra of total mission average flux $[cm^{-2}s^{-1}MeV^{-1}]$ and total mission fluence $[cm^{-2}MeV^{-1}]$ related to several contributions: protons and electrons trapped into the terrestrial magnetic field, solar protons and galactic protons. In Fig.4.4 the total mission proton fluences as a function of the protons energy of trapped, solar, galactic protons and trapped electrons are visible along the selected circular polar LEO orbit.

The spectrum of the total displacement damage (1 MeV neutrons equivalent) in Silicon was obtained converting the fluence spectrum of each contribution (even from different particle types) into their equivalent damage, using the NIEL scaling hypothesis. This allows to compare the different damage contributions from the different particles. For each energy value of the spectrum E, the total displacement damage $DD(E)$ corresponding to the proton fluence $\phi(E)$ was calculated as:

$$DD(E) = D(E) \cdot \phi(E) \tag{4.1}$$

where $D(E)$ is the displacement damage cross section according to the

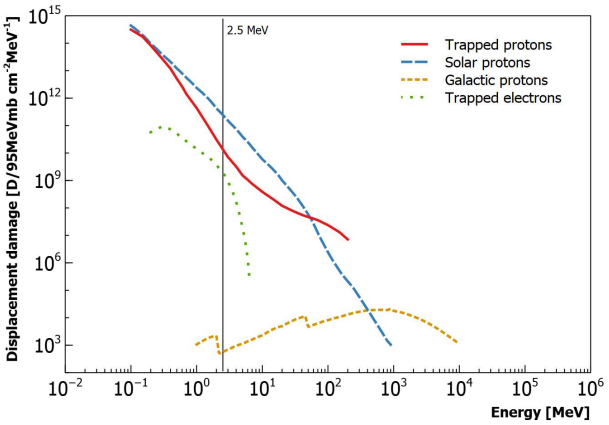

Figure 4.5: Total damage of trapped, solar and galactic protons and trapped electrons over the whole mission lifetime. The line marked at 2 MeV represents the energy cut which is assumed to be applied to data.

NIEL scaling hypothesis, which converts the effective particle damage into a 1 MeV neutron equivalent damage. In Fig.4.5 we can clearly observe that the highest impact on the total damage in Silicon is given by solar and trapped protons, while a minor impact is given by galactic protons and trapped electrons. For this reason, the last two contributions can be neglected.

Assuming a 80μm-thick Aluminum shielding of the whole detector, this produces a cut-off of the protons with energy lower than 2.5 MeV and reduces the total amount of damage on the sensors, as visible in Fig.4.6.

The resulting equivalent damage spectrum was then integrated over the whole protons energy range $[2.5MeV, E_{max}]$:

$$D_{tot} = \int_{2.5MeV}^{E_{max}} DD(E)dE \tag{4.2}$$

Lastly, the proton fluence at 74 MeV required to create such a total damage was extracted normalizing the total damage to the damage of a 74 MeV proton, according to the equation:

$$\phi(74MeV) = \frac{\int_{2.5MeV}^{E_{max}} D(E)\phi(E)dE}{D(74MeV)} = \frac{D_{tot}}{D(74MeV)} \tag{4.3}$$

where $D(E)$ is the 1 MeV neutron equivalent damage of the protons and $D(74MeV)$ is the 1 MeV neutron equivalent damage of 74 MeV protons. The 74 MeV equivalent fluence provided by SPENVIS software can be observed in Fig.4.7, where the trapped, solar and total protons fluence is plotted as a

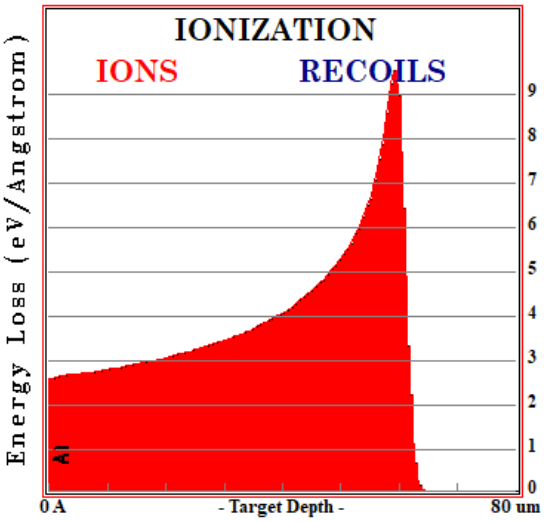

Figure 4.6: SRIM simulation of 2.5 MeV H ions energy loss in 80 μm Al target

function of the Al shield thickness. Here, it can be observed that with 80μm, 4×10^{11} 74 MeV total protons are obtained as maximum fluence, which means 6×10^{11} 1 MeV n_{eq}/cm^2. Therefore in this work, the irradiation fluence range considered is $7.4\times10^{4}\div6.4\times10^{11}$ n_{eq}/cm^2. Twelve intermediate fluence steps were chosen within this range, with a thicker spacing to the highest fluences.

The fluence absorbed by each SiPM was eventually obtained integrating the beam profile over the area of the sensor, which is $1 \times 1mm^2$ for almost all of them.

4.3 Experimental Setup

Originally designed for a 148 MeV proton beam as a representation of the typical energies in proton therapy field, the dual-ring scattering system was lowered to 74 MeV for the irradiation tests described in this chapter, to avoid possible nuclear activation of the samples under test. This was obtained through Water-equivalent polystyrene material (RW3) resulting in a beam with an equivalent uniform circular area with 7.8 cm radius.

The experimental setup can be observed in Fig.4.8, where the main setup components are visible: an ionization chamber which measured the total number of protons, a *dark box* which contains the SiPMs during the irradiation and the measurements, the RW3 blocks which lowered the beam energy and the measurement setup.

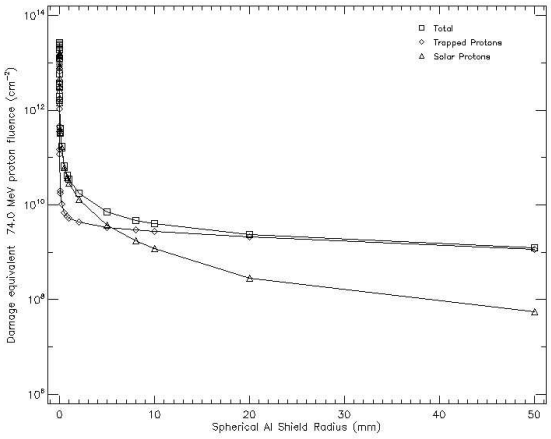

Figure 4.7: Equivalent 74 MeV protons fluence as a function of the radius of an Aluminum spherical shielding along a Low Polar Orbit (550 km - 97°) for trapped and solar protons.

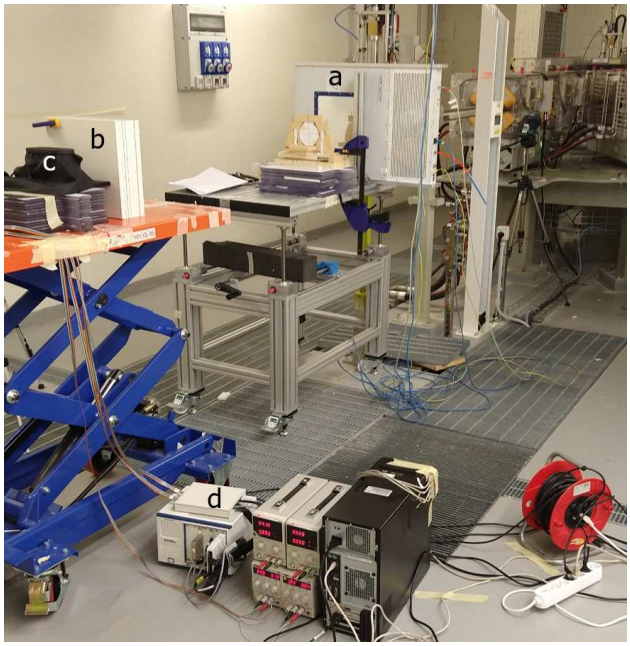

Figure 4.8: Irradiation setup with the double-ring scattering system at the Proton Therapy Center in Trento, where the different setup components are clearly visible: the ionization chamber (a), the PW3 used for the energy lowering of the beam (b), the dark box including the irradiated sensors (c) and the I-V measure setup (d).

Reverse current-voltage measures were taken on the irradiated SiPMs shortly after each fluence step. This was chosen as the best solution to prevent annealing effects from affecting the reverse I-V measures.

The sensors were placed on a custom Printed Circuit Board (PCB) as visible in Fig.4.9 featuring eight chip spots, each one occupied by a silicon chip dedicated to test structures, which included more than one $1 \times 1mm^2$ SiPM with different cell sizes. Each SiPM was then connected with wire bonding to the PCB and that was connected to the acquisition system through 2 m long cables. The PCB was inserted into a 3D plastic dark box with a motor-controlled light shutter which was left open during the irradiation and closed during the measure.

Two different PCB where irradiated, each one with a different final fluence: 1.4×10^8 n_{eq}/mm^2 and 6.4×10^9 n_{eq}/mm^2.

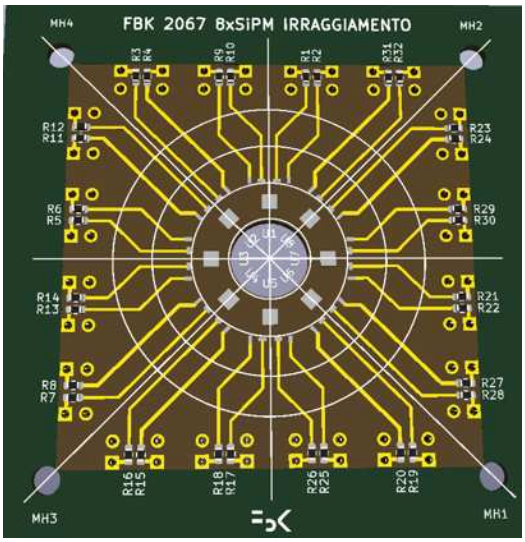

Figure 4.9: Layout image of the PCB used for the irradiation test

After irradiation, SiPMs were left annealing at room temperature ($20 \div 25°C$) for 30 days, connected to the acquisition system. During the whole annealing time, reverse I-V measures were taken once a day.

A set of SiPMs was irradiated as naked chips at 10^{11} n_{eq}/cm^2 and then mounted on a PCB at a later moment. This was useful to have a set of SiPMs available for functional characterization with standard FBK setups and boards.

The SiPM technologies under test are listed in Tab.4.1 where each technology is described in its own specific features. Not all the technologies described in the table were fully characterized, only the most promising of

them were chosen for this purpose. In particular, the technologies investigated in detail were: NUV-HD-RH, NUV-HD-cryo, RGB-HD, NIR-HD and VUV-HD2019 (or VUV-HD).

Technology	**cell size** [μ**m**]	**FF** [%]	$\mathbf{V}_{bd}$ [**V**]	$\mathbf{PDE}_{pk}$ [**nm**]
NUV-HD-RH	12.5	56.8	32.3	400
NUV-HD-RH	15	61.3	32.3	400
NUV-HD-RH	15	63.6	32.3	400
NUV-HD-RH	20	70.4	32.3	400
NUV-HD-RH	20	72.3	32.3	400
NUV-HD-cryo	15	56.0	33.0	420
NUV-HD-cryo	20	66.0	33.0	420
NUV-HD-cryo	40	82.0	33.0	420
VUV-HD-lowAP	35	80.0	31.2	420
VUV-HD-lowAP M0	35	80.0	31.2	420
VUV-HD	35	80.0	31.2	420
VUV-HD M0	35	80.0	31.2	420
NIR-HD	20	66.0	27.8	500
RGB-HD	20	66.0	27.8	525
RGB-HD EnhancedBorder	20	66.0	27.8	525

Table 4.1: Summary of the parameters and properties of the different technologies under test.

4.4 Results

In this section, as in Ch.3, the standard methods of characterization of silicon sensors (as in [50]) were adapted to devices with an internal gain like SiPMs.

Measurements were performed at both the irradiation facility and in the FBK laboratories. In particular, the reverse I-V measurements in both light and dark conditions were taken at the Trento Proton Therapy facility during the irradiation process, as described above.

4.4.1 Reverse Current

As mentioned in Ch.2, the defects produced by radiation damage result in an increase of the "leakage current" (from the surface defects, not multiplied) and the "dark current" (from the bulk defects, multiplied)[78]. A measurement of the variation of these two current components can provide

an indication of the quantity of damage that a SiPM has experienced and the effects of this damage. Reverse current-voltage measurements were performed shortly after each irradiation shot in both light and dark conditions through a current-controlled LED inside the dark box. As mentioned in Sec.3.3.2, measurements under fain illumination were necessary to estimate accurately the breakdown voltage from I-V characteristics. All the other measurements were taken in dark conditions. In Fig.4.10 the increase of the reverse current in the dark with fluence can be observed for the NUV-HD-RH SiPM with 20μm cell and the VUV-HD 2019 with 35μm cell in dark conditions.

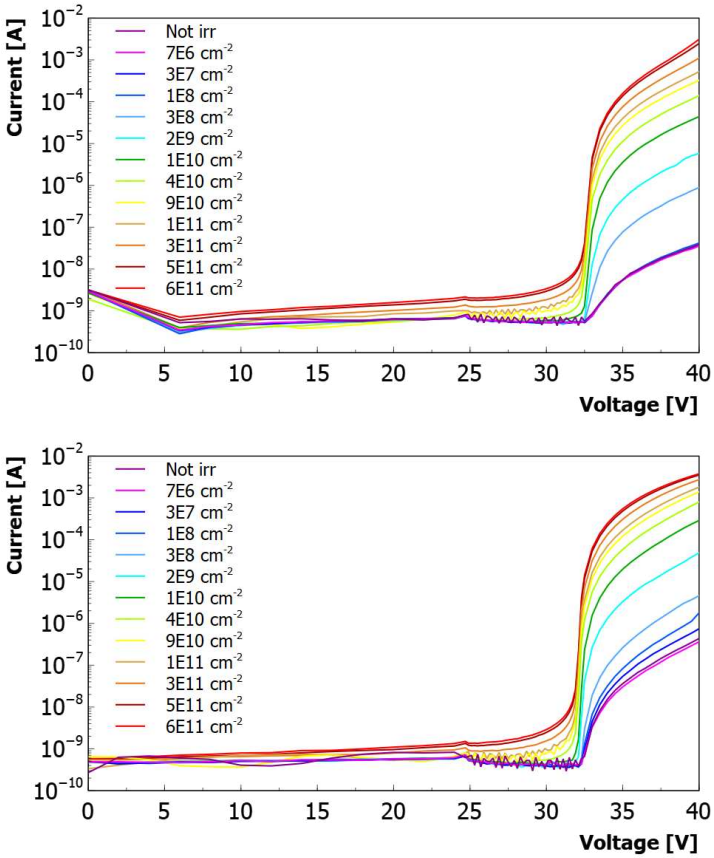

Figure 4.10: Reverse current as a function of the bias voltage at the several fluences for the NUV-HD-RH SiPM with 20μm cell (left) and the VUV-HD 2019 with 35μm cell (right) in dark conditions.

The reverse current, specifically the increase of the reverse current $\Delta I = I_\phi - I_{\phi_0}$ in dark conditions was used to extract the damage parameter α [50], as observed in Ch.3, normalized to the current gain value. In this way, it is

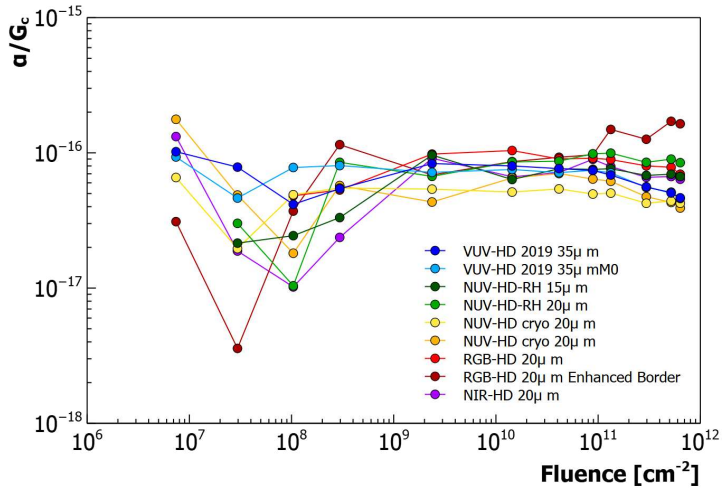

Figure 4.11: Damage parameter of the tested technologies as a function of the fluence at 3V excess bias.

possible to make a first comparison among the technologies. In Fig.4.11, the damage parameter α is plotted as a function of the fluence at 3V excess bias, showing a fairly uniform trend of all the tested technologies, apart form the RGB-HD SiPM with Enhanced border 20 μm cell, which shows an increase of α starting from 10^{11} n_{eq}/cm^2. This latter effect might be the result of a damage effect on the technology, or it might be an anomaly due to the fabrication process of that single SiPM.

From the reverse current-voltage curves the breakdown voltage was estimated using the second logarithmic derivative method SLD (see Sec.3.3.2). In Fig.4.12 the results are visible, showing that the breakdown voltage is constant for almost all the technologies in this irradiation range, except for the RGB-HD SiPM with Enhanced border 20 μm cell, where it starts to increase at 10^{11} n_{eq}/cm^2. This could be the result of a very high increase of the leakage current (higher than in the other technologies).

4.4.2 DCR

DCR was extracted from the dark current through the Current Gain G_c, which was previously introduced. The DCR can be estimated from Eq.3.5 which, in irradiated SiPMs, holds its validity under the assumption that the current gain, i.e. the Gain of the device and the correlated noise represented by the ECF, remains constant[78]. To verify this assumption, a direct measure of the current gain was performed on the samples irradiated at 10^{11}

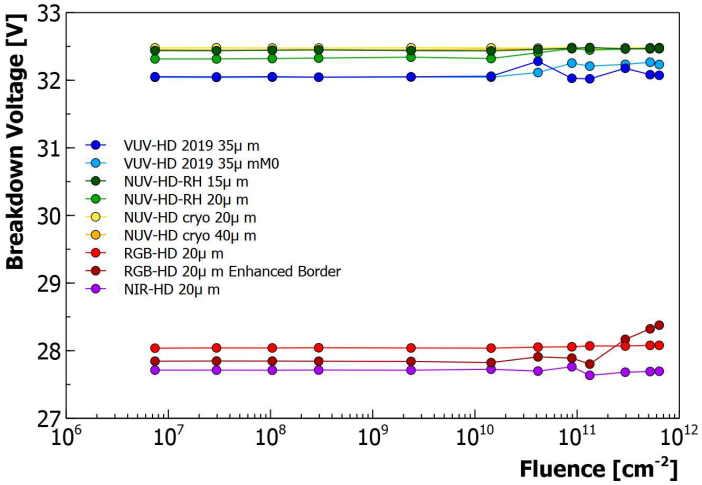

Figure 4.12: Breakdown voltage of the tested technologies as a function of the fluence.

n_{eq}/cm^2. Due to the high DCR, the measurement was made at -40°C, where the noise is significantly reduced by the temperature. The results can be observed in Fig.4.13, where the current gain is plotted as a function of the excess bias. The plot does not show any relevant change, suggesting that the current gain is not affected by the radiation, at least up to 10^{11} n_{eq}/cm^2[79].

After verifying that the current gain remains constant with irradiation, DCR was extracted form the dark current at the several fluences for all the technologies under test, as visible in Fig.4.14. In the plot, the curves start at different levels due to differences in the DCR before irradiation between different SiPM technologies and sample-to-sample variations, then they tend to converge toward similar values, looking more similar as the fluence increases. This could mean that the as the fluence increases, the defects introduced by the radiation damage prevail on the intrinsic defects and contaminants concentration of each technology and of each specific sample introduced during their fabrication process. The RGB-HD SiPM with Enhanced border 20 μm cell shows a more pronunced increase of the DCR starting at 10^{11} n_{eq}/cm^2, as already observed in the case of the damage parameter α and the breakdown voltage. It has to be pointed out that the DCR estimation is accurate until the G_c assumption holds true. For this reason, the DCR estimation above 10^{11} n_{eq}/cm^2 could result not completely accurate.

Although not obvious from Fig.4.14, some SiPMs, mainly the larger-sized ones, exhibit some saturation effects at high fluences. SiPM saturation (due to the high cell occupancy) means that the DCR values are comparable

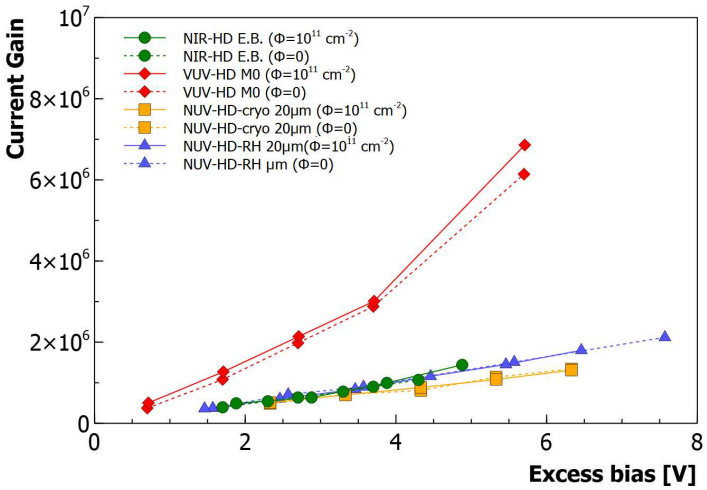

Figure 4.13: Gain current as a function of the excess bias mneasured at -40°C for the RGB-HD, NUV-HD-RH, VUV-HD 2019 and NUV-HD-cryo technologies, irradiated at 10^{11} n_{eq}/cm^2.

to the maximum possible count rate of a SiPM with all cells constantly triggering[78].

The effect of the saturation on the different SiPMs is visible in Fig.4.15 where the cell occupancy is plotted as a function of the fluence at 3V excess bias. Cell occupancy (C.O.) was estimated as:

$$C.O. = \frac{N_t^{tot}}{N_t^{tot}{}_{nosat}} \tag{4.4}$$

where N_t^{tot} is the number of counts, i.e. the number of SPADs triggered by the total light and noise events in a certain integration time window t_{int} taking into account cell saturation effects, $N_t^{tot}{}_{nosat}$ is the number of counts where saturation effects are neglected. These contributions are given by:

$$N_t^{tot} = N_{cell}\frac{t_{int}}{\tau}\left(1 - e^{-\frac{1+CT}{N_{cell}}(N_{ph/s}\cdot t_{int}\cdot PDE + DCR\cdot t_{int})\frac{\tau}{t_{int}}}\right) \tag{4.5}$$

$$N_t^{tot}{}_{nosat} = (1+CT)(N_{ph/s}\cdot PDE + DCR\cdot t_{int}) \tag{4.6}$$

where $N_{ph/s}$ is the number of incident photons per second, τ is the effective recharge time of the cells and CT is the cross-talk probability.

Here a clear reduction of the DCR triggering efficiency can be observed for the large-sized SiPMs, whereas the curve of small-sized cell SiPMs, remains almost constant.

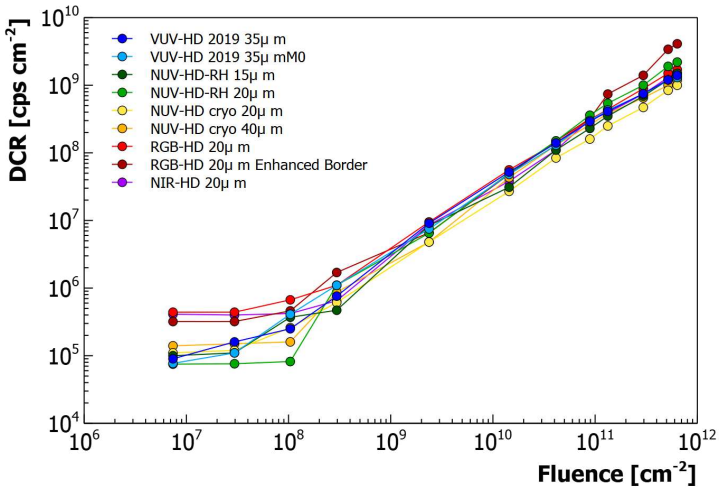

Figure 4.14: Dark Count Rate of the tested SiPMs as a function of the irradiation fluence.

4.4.3 PDE

As mentioned in ch.3, PDE measurement on damaged SiPMs is not straightforward due to their high noise which makes the dark current comparable to the light current when SiPMs are illuminated. As a consequence, the measurement does not result accurate. For this reason, the results on the PDE were derived by a *Responsivity* measurement on the samples irradiated at 10^{11} n_{eq}/cm^2, as described more in detail in Sec.3.3.5. These were illuminated with a 420nm LED using the setup described in Ch.3. The results are visible in Fig.4.16, where the responsivity is plotted as a function of the excess bias, for irradiated (straight line) and not-irradiated (dashed line) samples. One sample for each technology was considered, and no significant changes were observed in any of them. This means that the PDE remains constant with fluence, at least up to 10^{11} n_{eq}/cm^2 in all the technologies under test[79].

4.4.4 SNR

In the previous sections, the results of a complete functional characterization of the SiPMs have been shown and discussed in detail. These pieces of information are not enough to compare the different technologies and select the most promising ones for a given space application. For this reason, some figures of merit more related to specific experiments operating in space should be introduced. One of these is the Signal-to-Noise Ratio (SNR), which results useful to compare the performance of the SiPMs before and after irradiation.

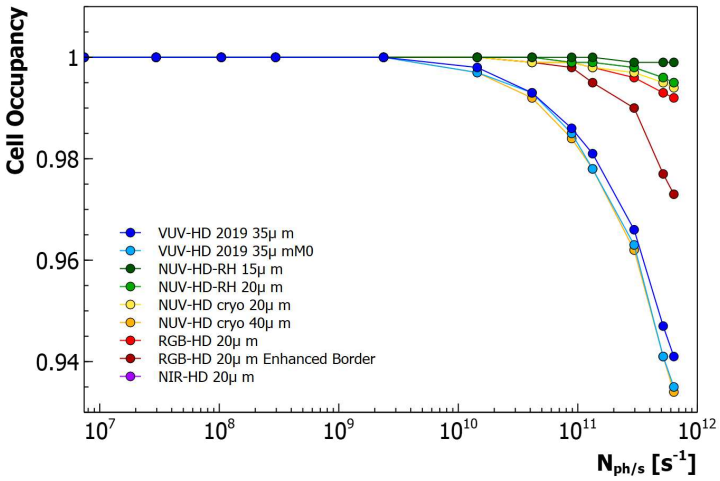

Figure 4.15: Saturation of SiPM cells as a function of the fluence at 3V excess bias, with visible effects on the devices with larger cell pitches.

In pulse counting detectors, SNR is defined as:

$$SNR = \frac{N_t^{tot} - N_t^{noise}}{\sqrt{ENF \cdot N_t^{tot}}} \tag{4.7}$$

where ENF is the Excess Noise Factor described in Sec.1.3, and:

$$N_t^{noise} = N_{cell} \frac{t_{int}}{\tau} \left(1 - e^{-\frac{1+CT}{N_{cell}}(DCR \cdot t_{int})\frac{\tau}{t_{int}}}\right) \tag{4.8}$$

where N_t^{noise} is the number of SPADs triggered by noise events in the same time window.

In Eq.4.7 the ENF is estimated as the uncertainty of the correlated noise in the SiPMs. In particular, this was estimated as[80]:

$$ENF = \frac{1}{1 - ln(1 - P_{corr})} \tag{4.9}$$

where P_{corr} represents the probability of having a correlated noise event, either cross-talk or afterpulsing.

The results of the SNR estimation at 3 V of excess bias are visible in Fig.4.17, where SNR is plotted as a function of the fluence (6.4×10^{11} n_{eq}/cm^2) and of number of incident photons at fixed integration time (2 μs) as in the ALPIDE Monolithic Active Pixel Silicon sensor[81], developed at CERN for the ALICE ITS Upgrade and also considered for future satellite particle trackers. From the plot, a better performance of the SiPMs with larger cell

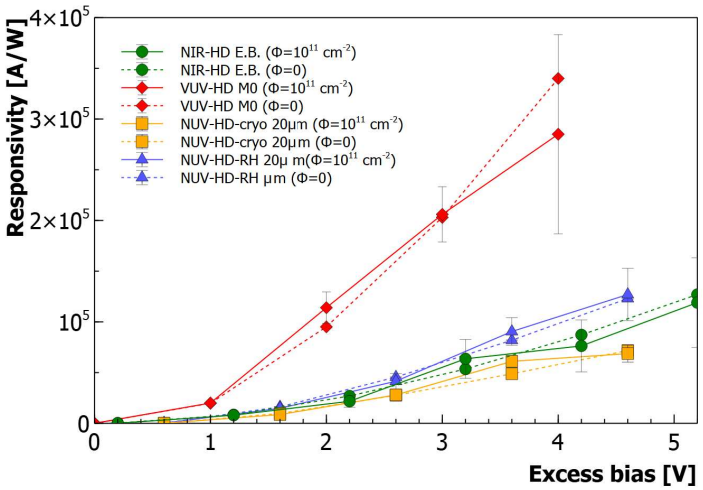

Figure 4.16: Responsivity as a function of the excess bias for RGB-HD, NUV-HD-RH, VUV-HD 2019 and NUV-HD-cryo technologies, irradiated at 10^{11} n_{eq}/cm^2 (straight line) and not-irradiated (dashed line).

size can be observed up to 10^{10} ph/s, where they start to suffer a saturation process. Their high SNR at low number of incident photons per second is mainly due to the high PDE, thanks to the higher FF of the larger microcells. Conversely, the small-sized SiPMs appear less affected by the saturation.

In order to extract quantitative values, thus compare the SiPM technologies, a specific case needed to be addressed. In this case, the sensors were supposed to detect 450 nm photons and, once fixed the rate of photons and the integration time, the SNR was estimated as a function of the fluence. The rate of photons impinging on the detector active area was fixed at 10^{10} ph/s to get an high SNR without considering saturation effects (see Fig.4.17). The integration time was fixed at 2 μs. The results are shown in Fig.4.18, where the SNR is plotted as a function of the fluence. Here, a general worsening of the performance of the sensors at around 10^{11} n_{eq}/cm^2 can be observed. Among the SiPMs with 20 μm cell pitch, we observe a low SNR (around 200) for the NIR-HD, NUV-HD cryo and RGB-HD technologies, whereas the NUV-HD-RH and NUV-HD-cryo with 20 μm cell pitch show an higher SNR. In particular, the most significant result comes from the NUV-HD-RH SiPM with 15 μm cell which shows a high SNR (around 440). Among the large-sized SiPMs, which are supposed to have an higher SNR due to their high FF and PDE but also an earlier saturation, the NUV-HD-cryo technology with 40 μm cell shows the highest SNR. Overall, it can be assumed that the SNR is deeply affected by PDE, DCR and saturation effects. At low fluences,

under the light conditions described above, the PDE has an high impact on the SNR. Nonetheless, SiPMs with large cell size (thus, high PDE) has a lower SNR than the ones with small cell size (thus, low PDE) and this can be attributed to saturation effects. RGB-HD SiPMs show a SNR lower or comparable to the one of the 35 μm even at low fluences and this is mainly due to their higher DCR, as visible in Fig.4.14.

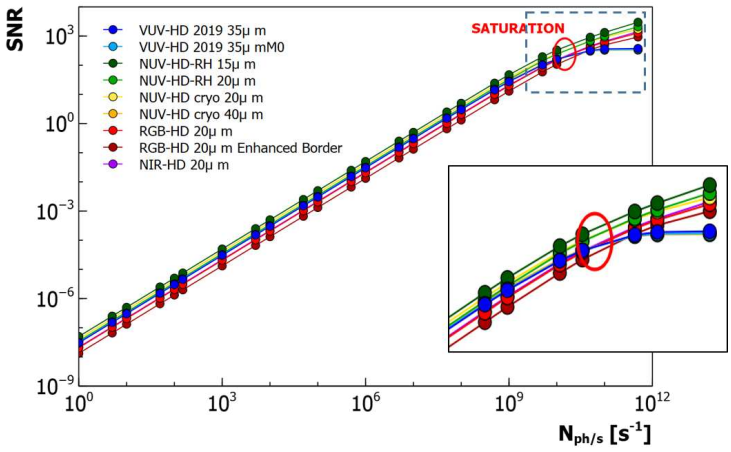

Figure 4.17: Signal-to-noise ratio as a function of the fluence at fixed excess bias (3V), integration time (6.8×10^{-8} s) and fluence (6.4×10^{11} n_{eq}/cm^2).

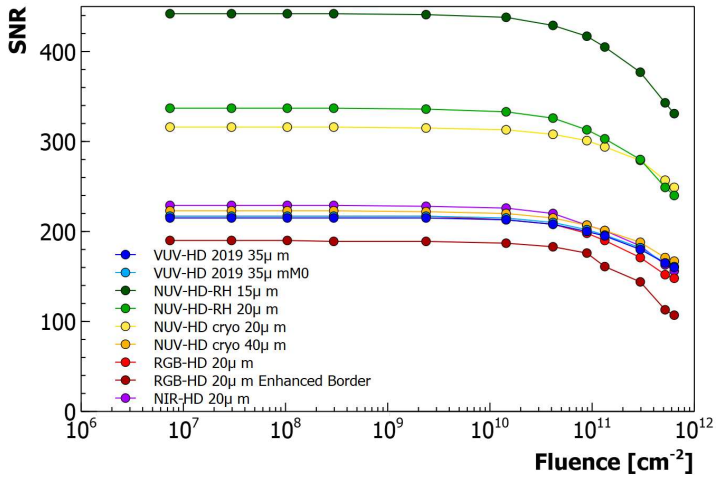

Figure 4.18: Signal-to-noise ratio as a function of the fluence at fixed excess bias (3V), integration time (6.8×10^{-8} s) and number of photons (2×10^{10}).

4.4.5 Energy Resolution

Energy resolution is a measure of the accuracy in detecting the energy of the particles. Energy resolution estimation is strictly dependent on the application of the sensors. In this case, X and γ-rays detected by a scintillator and read by SiPMs are considered as example of applications. Once the particle is detected, the charge collected by the scintillator is integrated over a certain time interval t_{int}. In the case described, the energy resolution, i.e. the resolution in the measurement of the number of photons observed in a given integration window, can be estimated as:

$$\sigma_E \propto \sqrt{\frac{ENF^*}{N_{ph/s} \cdot t_{int} \cdot PDE} + \frac{ENF^* \cdot DCR \cdot t_{int}}{(N_{ph/s} \cdot t_{int} \cdot PDE)^2}} \tag{4.10}$$

where ENF* is the Excess Noise Factor, in this case estimated as product of several ENF contributions[80] from PDE, DCR, gain, cross-talk, afterpulsing and non linearity.

In Fig.4.19 the estimated energy resolution obtained from Eq.4.10 for several SiPM technologies is plotted as a function of the fluence. Here, a distinction between the large-sized (35-40 μm) and the small-sized (15-20 μm) SiPMs is clearly visible. In particular, the large-sized ones have an higher σ_E, at around 1%. A trend with the cell size can be observed, apart from the RGB-HD SiPM with Enhanced border 20 μm cell which has an higher σ_E, nearly 1%, at the same level of the 35 μm cell SiPMs. Moreover, the energy resolution of the RGB-HD SiPM with Enhanced border 20 μm cell starts to increase at 10^{11} n_{eq}/cm^2 until reaching a 2% value.

Overall, NUV-HD-RH and NUV-HD-cryo technologies show the best performance under the conditions described above at 6.4×10^{11} n_{eq}/cm^2, with an higher SNR and a better energy resolution. It has to be pointed out that this result holds when applied to X-ray spectroscopy.

4.4.6 Annealing

An annealing test was performed on the irradiated sensors to test their recovery from the radiation damage. The SiPMs were subjected to a 30-days annealing at room temperature ($\sim$ 20°C), while their reverse current-voltage characteristics were measured approximately every twelve hours. The results of the annealing test are visible in Fig.4.20, where the normalized currents are plotted as a function of the annealing time at 3V of excess bias. From the figure, the RGB-HD SiPMs appear to show the fastest recovery, while the the RGB-HD SiPM with Enhanced border 20μm cell reduces its current

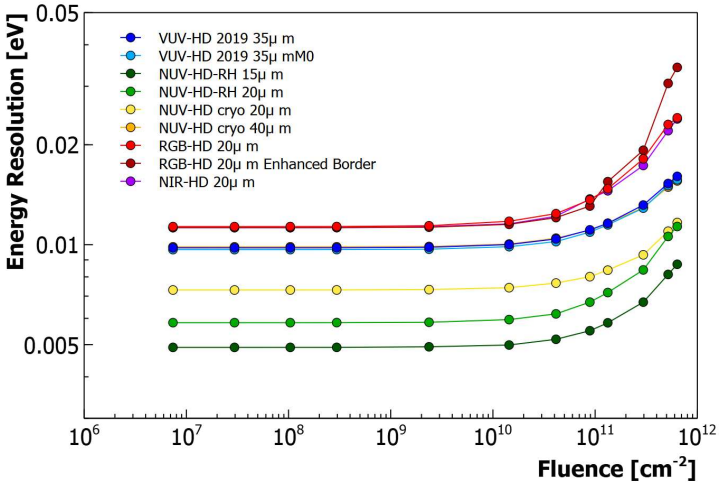

Figure 4.19: Energy resolution as a function of the fluence at fixed excess bias (3V), integration time (6.8×10^{-8} s) and number of photons (2×10^{10}).

by almost 60% after the whole 30 days annealing time. However, the RGB-HD with enhanced border is also the device that suffered the most from radiation damage, so that this result may not be representative of a general trend among devices and further investigation will be needed to draw conclusions. The other technologies show an initial fast decrease until approximately 5×10^3 minutes, where they present a knee and then a slow recovery. A similar situation was observed in silicon sensors without an internal gain in Fig.2.11, where a variation of the slope in the curve at room temperature at around is 5×10^3 visible. Overall, after the whole 30-days annealing time, the RGB-HD Enhanced Border, NUV-HD-RH and NUV-HD-cryo 20μm technologies are the ones recovering the most, while the VUV-HD and NUV-HD-cryo 40μm appear to recover the less. In the case of the the NUV-HD-RH and NUV-HD-cryo technologies this might be due to their lower internal field which enhances their dependence on the temperature.

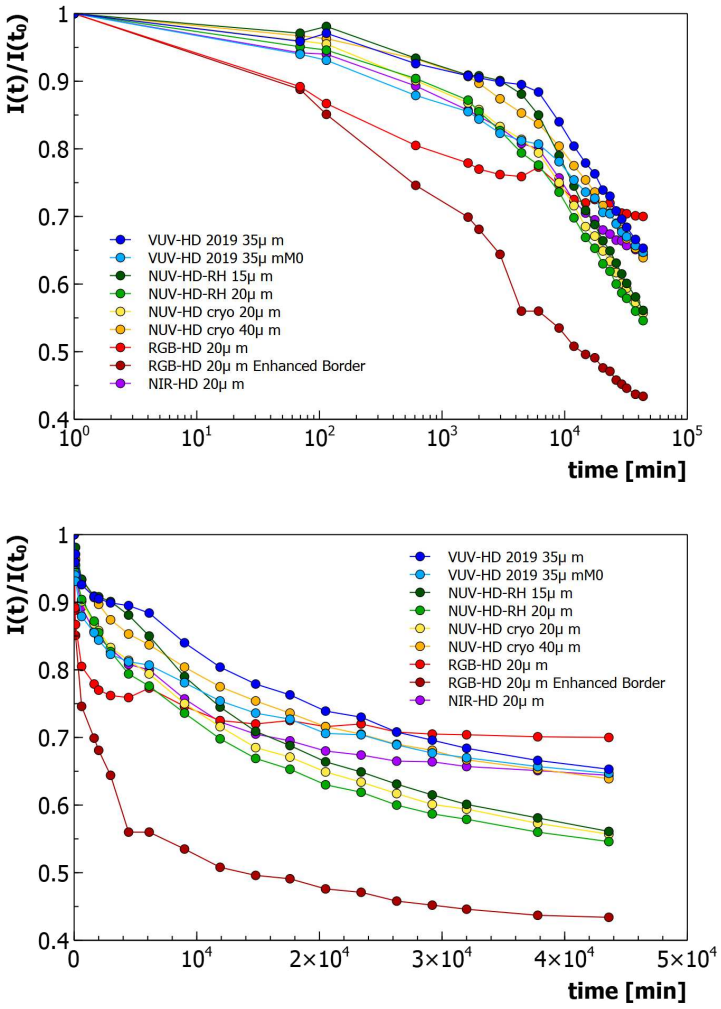

Figure 4.20: $I(t)/I(t_0)$ ratio as a function of the annealing time after irradiation at room temperature ($20 \div 25°C$), in logarithmic (top) and linear (bottom) scale.

Chapter 5

X-rays irradiation at TIFPA

In this chapter, the effects of the X-rays on SiPMs will be discussed. In particular, an irradiation test on several FBK SiPM structures was performed and their behaviour after irradiation was investigated. Contrary to the previous chapters, this one will be mainly focused on the effects of the ionizing radiation. As discussed in Sec.2.4, ionizing radiation mostly affects the surface of the SiPM, producing traps at the interface between the oxide (SiO_2) and the Silicon and fixed charge in the silicon oxide. From the functional characterization of the irradiated SiPMs the effects of the radiation damage on the surface and the bulk of the device will be investigated.

5.1 TIFPA X-rays irradiation facility

Irradiation tests took place at the Trento Institute for Fundamental Physics Applications (TIFPA) laboratories in Trento (Italy) in April 2021. The facility is mainly used for biological and biophysics cellular irradiation studies, while since late 2019 it started to operate also as a facility for testing of Total Ionizing Dose (TID) effects on silicon sensors and electronic devices. The X-rays setup is equipped with a Comet MXR 226 (3KW) tube inserted inside a Xstrahl RS 225 cabinet[82]. The tube is equipped with a tungsten (W) anode and a 0.8 mm Berillium (Be) exit window. The voltage on the anodes ranges from 30 kV and 197 kV, producing four emission lines: K-α, K-β, L-α, L-β emission peaks in the X-ray spectrum. Among these emission lines, the K-lines (50-70 keV) are typically used for biology applications or for analysis on materials, while for tests on silicon sensors require the use of L-lines (7-12 keV) is preferred, due to the small thickness of the silicon devices. The intensity spectrum is visible in Fig.5.1, where a 40 kV voltage applied on the anode and a 0.018 mm Al filter out of the tube window exit

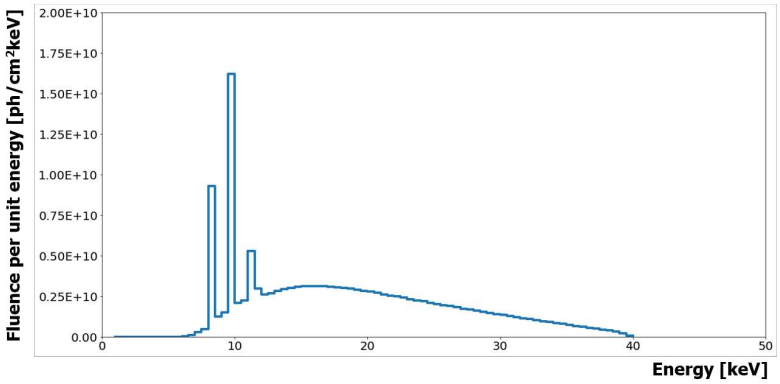

Figure 5.1: Example of X-rays spectrum considering a 40 kV voltage applied on the anode, a 0.018 mm of Al filter out of the tube window exit, a 20 mA current and a distance of 20 cmFSD.

are considered, setting the maximum and minimum values of the spectrum respectively.

A section of the Xstrahl RS 225 cabinet is visible in Fig.5.2, where the Focal Spot Distance and Irradiation Field Size can be observed, showing an irradiation angle of approximately 33°.

5.2 Experimental Setup

The irradiation setup consisted in the cabinet described above, the acquisition system and a dosimetric probe composed of a calibrated PTW Farmer Chamber read by an external electrometer. The whole irradiation setup can be seen in Fig.5.3, where all the components are distinguishable.

SiPMs were mounted on a custom PCB similar to the one used during the proton irradiation shown in Fig.4.9 and placed on a 3D printed support. This had the dual purpose of fixing the position of both the PCB and the LED illumination, and placing the PCB at exactly 20 FSD (see Fig.5.2). In this case, almost the same technologies as the ones in Ch.4 were irradiated. The PCB was placed inside the cabinet, providing a dark environment, and was remotely connected to the acquisition system outside the cabinet using 2m long cables. The PCB was fixed to the plastic support together with the dosimetric probe, which was placed in the center of the PCB. A detailed view of the PCB, the probe and the cables can be observed in Fig.5.4. The PCB was directly connected to a remotely controlled switching matrix performing online current-voltage measurements. I-V measurements were taken shortly after each irradiation step. In fact, the dose was gradually increased

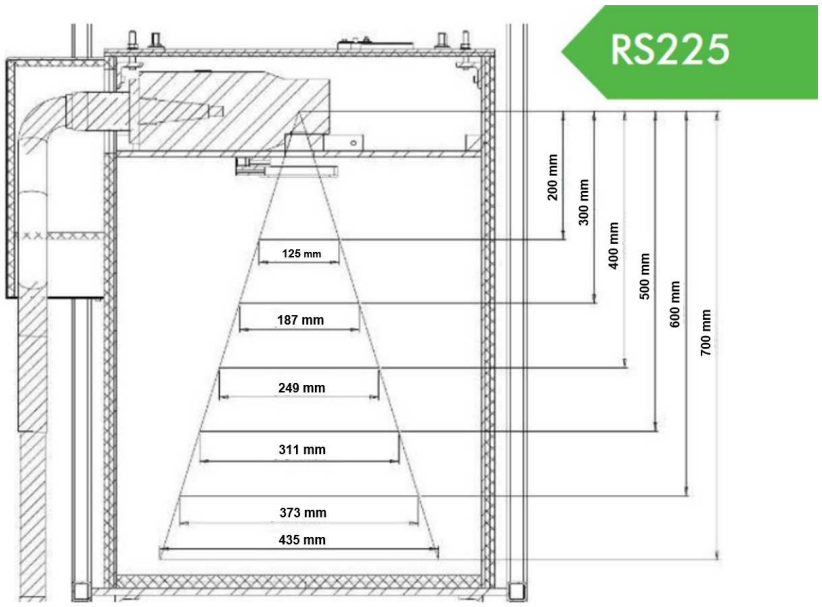

Figure 5.2: Focal Spot Distance and Irradiation Field Size of the Xstrahl RS 225 cabinet.

up to 100 kGy and taking measurements between one shot and another provided information about the effective damage on the sensors, minimizing the annealing effects.

5.2.1 SiPM technologies

Several FBK SiPM technologies were irradiated simultaneously during the tests. In particular, several test structures, each one including 1×1 mm^2 SiPMs with different cell size, were tested. The main purpose of this choice was to save time and to make an accurate comparison on the main X-rays damage effects on the different technologies irradiated at exactly the same doses.

The main properties of the FBK technologies under test are summarized in Tab.4.1, where the main functional parameters of each technology are also shown. Among the several technologies, only a few of them were fully characterized after irradiation, selected as the most interesting ones based on their cell dimension and their properties.

All the SiPMs under test were left annealing at room temperature for 30 days after irradiation, while reverse current-voltage measurements were performed on all the samples every 12 hours for the whole annealing time.

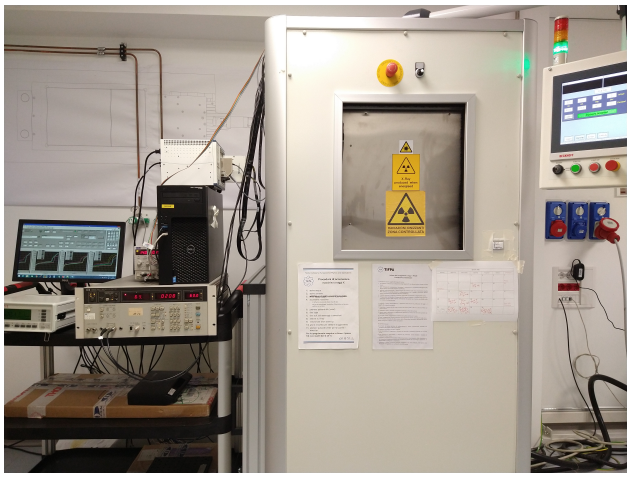

Figure 5.3: Complete setup of the X-rays irradiation, from the Xstrahl RS 225 cabinet to the acquisition system.

5.3 Results

This section will be organized differently with respect to the Sec.3.3 and Sec.4.4 as, after an initial discussion on the breakdown voltage, each technology will be individually investigated in detail in terms of noise and other functional parameters. Indeed, X-rays produce different effects on the devices compared to protons. In this case, some of the parameters used for the proton irradiation tests described above will not be used since they do not provide useful information on the evolution of the damage inside the sensors, nor on a possible comparison among the technologies. For example, some of the parameters described above, as for example the "damage parameter α" provide information about the radiation damage assuming the damage happening in the bulk of the SiPM, whereas in this case the X-rays damage results in macroscopic effects in both the bulk and the surface of the sensors.

5.3.1 Breakdown Voltage

The breakdown voltage was estimated from the reverse current using the maximum of its second derivative SLD (see Sec.3.3.2). In Fig.5.5 the results of the breakdown voltage as a function of the irradiation dose are shown. In particular, it remains constant up to 10^4 Gy for all the technologies, than it starts a slight increase until reaching a maximum increase of 0.2 V at 10^5 Gy in almost all the technologies, probably due to an increase of the pre-breakdown current. In the NUV-HD-cryo SiPM with a 40 μm cell pitch this shift is estimated in less than 0.1 V and this represents the minimum

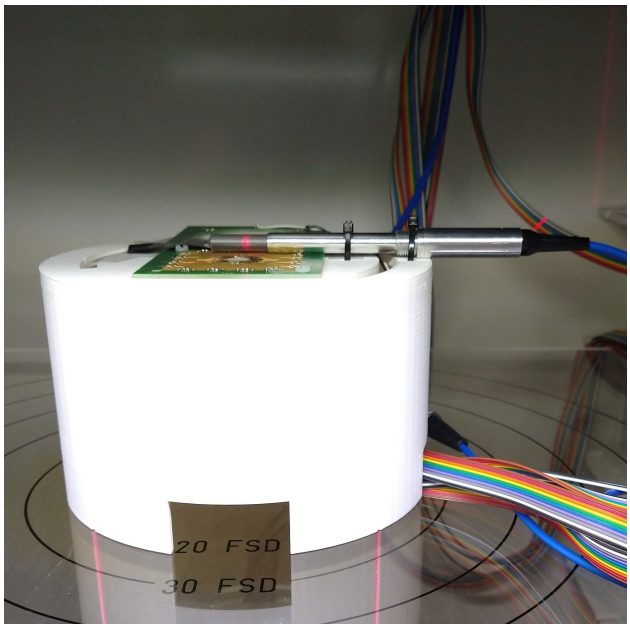

Figure 5.4: Detail of the SiPMs mounted on a PCB and placed inside the cabinet with a dosimeter probe fixed to the structure.

variation among the different technologies.

Overall, the breakdown voltage does not provide enough information to make a comparison among the technologies.

5.3.2 NUV-HD-RH

The NUV-HD-RH technology is one of the latest releases in FBK and, due to its small-sized cells and low internal field, it represents a good candidate for applications where a high radiation tolerance is required.

The results of the reverse current-voltage characteristics performed shortly after each irradiation shot can be observed in Fig.5.6, where the current values are plotted at several irradiation doses, including the current-voltage curve measured after the annealing process. As visible from the figure, there is a gradual increase of the current which becomes significant starting from 10 kGy. The shape of the high-dose curves suggests that there is a strong increase of the leakage current which tends to cover the dark current (i.e. the leakage current becomes the dominant current contribution, higher than the dark multiplied current), at least at low excess bias values. Due to the dominance of the leakage current, the DCR estimation from the current as in Eq.3.5 is no longer possible.

Several approaches were used to estimate the DCR from reverse I-V curves

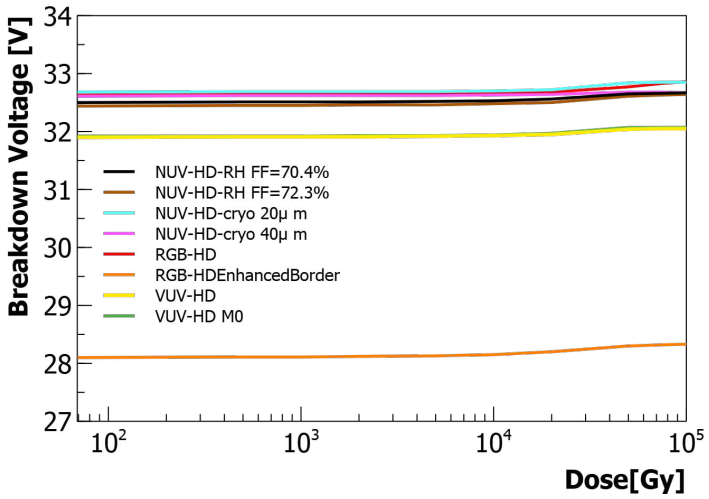

Figure 5.5: Breakdown voltage as a function of the irradiation dose for the different technologies.

and to compare the results to the ones obtained from a direct measurement of the DCR in pulse-counting mode at 20°C for irradiated and non-irradiated samples. Such different approaches are shown in Fig.5.7 for the NUV-HD-RH SiPM with 20 μm cell pitch and FF=72.3 %. The first approach was the standard estimation from the current using the Eq.3.5 as in the previous chapters. This showed a DCR two order of magnitude higher than the values obtained from the direct measurement, due to the dominance of the leakage current over the dark current. For this reason, in the second approach the dark current was extracted from the total current by (i) fitting the I_{leak} with a polynomial function before breakdown and (ii) subtracting the value of the fit function from the total current above breakdown. This provided results fully consistent with the DCR directly measured at 20°C. This confirms that I_{leak}, after irradiation, reaches values comparable to I_{dark} for some volts of excess bias above breakdown. As an example, in Fig.5.8 the total reverse current and its main contributions (leakage and dark currents) for the NUV-HD-RH SiPM with 20 μm cell pitch and FF=72.3 % are shown.

Because the DCR increase was moderate, it was possible to measure the PDE of the irradiated devices with the standard, pulsed technique, described in [83]. The PDE was observed not to change with increasing irradiation doses. This was measured at 800 nm and 450 nm. In particular, the 450 nm represents the wavelength where NUV and RGB are supposed to have similar values (see Fig.1.30, thus can be used to compare different technologies. The results of the PDE measurement are visible in Fig.5.9, where the irradiated

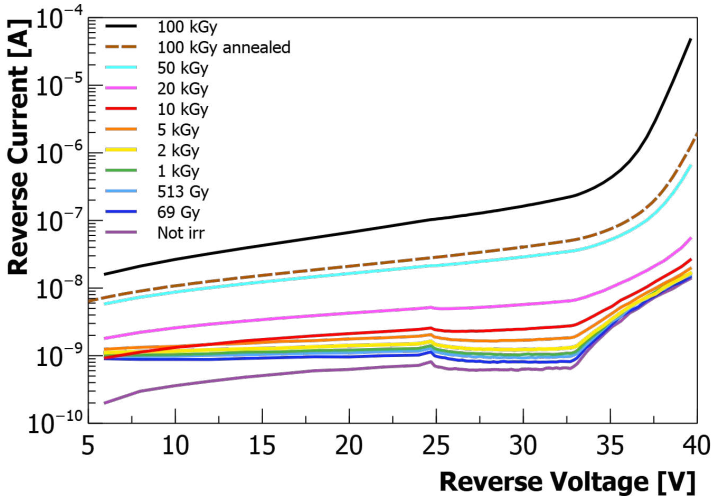

Figure 5.6: Reverse current-voltage characteristics with increasing radiation dose for the NUV-HD-RH SiPM with 20 μm cell pitch and FF=72.3 %.

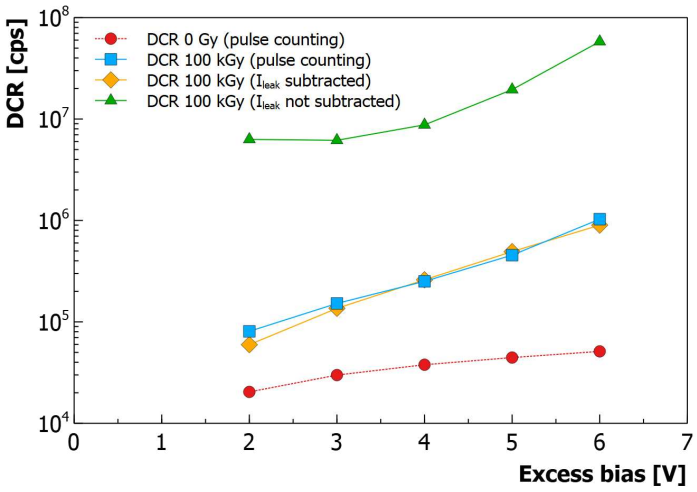

Figure 5.7: DCR as a function of the excess bias for the NUV-HD-RH SiPM with 20 μm cell pitch and FF=72.3 %. Several contributions can be compared: the DCR measured on the non-irradiated SiPM, the DCR measured at 20°C on the 100 kGy irradiated SiPM, the DCR estimated from only the dark current and the DCR estimated from the total current (leakage and dark currents).

and non-irradiated samples are compared at the two wavelength considered.

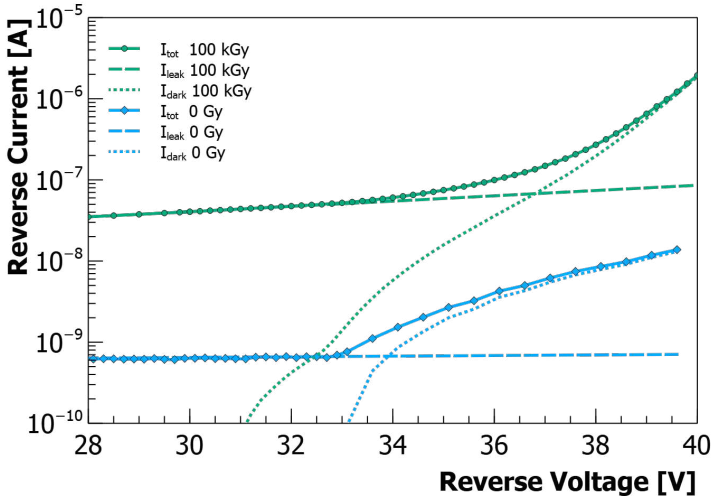

Figure 5.8: Detail of the reverse current contributions to the total current (I_{tot}, I_{leak} and I_{dark}) for the NUV-HD-RH SiPM with 20 μm cell pitch and FF=72.3 % at 100 kGy and 0 Gy.

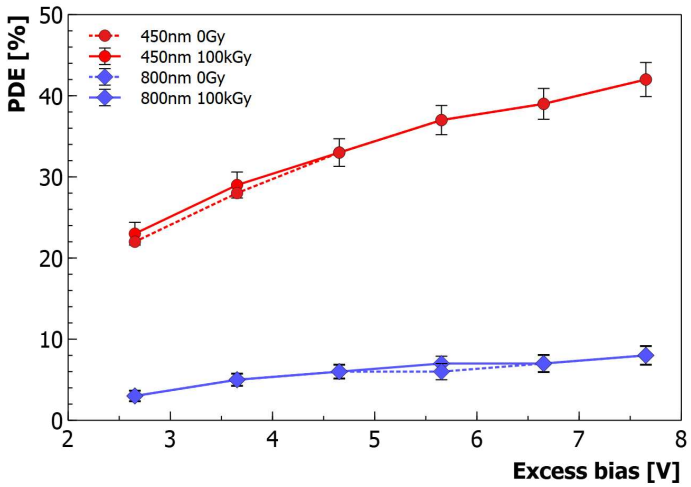

Figure 5.9: PDE as a function of the excess bias at 450 nm and 800 nm with a comparison between the irradiated and non-irradiated samples for the NUV-HD-RH SiPM with 20 μm cell pitch and FF=70.4 %.

5.3.3 NUV-HD-cryo

NUV-HD-cryo is a FBK technology designed for cryogenic applications due to its internal lower value of the electric field in the high-field region (i.e.

where the avalanche multiplication takes place). In this case two SiPMs were considered and compared, a SiPM with a 20 μm cell pitch and a SiPM with a 40 μm cell pitch.

The results of the reverse current-voltage measurements are shown in Fig.5.10 where in both cases a significant increase of the leakage current of at least one order of magnitude can be observed. It is interesting to observe a relevant increase of the current above the breakdown in the SiPM with 20 μm cell pitch, whereas this seems not to happen in the 40 μm cell pitch SiPM. As observed for the NUV-HD-RH technology, the increase of the current above the breakdown might not be strictly related to an increase of the DCR, while it may be the result of and increase of the leakage current.

The DCR was first directly measured at 20°C, then the results were compared to the DCR values estimated from the current (total current and dark current isolated fitting the leakage current with a third degree polynomial function), as already described in the previous section. From Fig.5.11, a slight increase of the DCR can be observed into the SiPM with 20 μm cell from 0 to 100 kGy. In particular, the DCR estimated through the total current (leakage and dark current) is much higher than the effective measured DCR curve in the SiPM with 20 μm cell pitch. Instead, no relevant changes are visible for the 40 μm cell SiPM. This might be due to the high dark current before irradiation, which remains higher than the leakage current even after a 100 kGy irradiation.

The PDE was estimated through a direct measurement at 20°C using a 450nm and a 800nm LED on the 20 μm cell pitch SiPM. The results are shown in Fig.5.12, where the non-irradiated samples are compared to the 100 kGy irradiated ones. At 450nm, there seems to be a slight variation of the PDE but this remains within the error bars, thus it can be assumed that PDE does not change with irradiation up to 100 kGy. The same conclusion can be drawn for the 40 μm cell pitch SiPM where the PDE was observed not to change at both the wavelengths under consideration.

5.3.4 RGB-HD

Unlike the previous ones, the RGB-HD technology consists of a n-on-p junction type and a p-type epitaxial and substrate. The reverse current-voltage characteristics of the RGB-HD SiPM with standard 20 μm cell pitch are shown in Fig.5.13, where a significant increase of both the leakage and dark current can be observed, around two order of magnitude in both cases. Here, the 50 kGy I-V curve is higher than the 100 kGy annealed curve, suggesting a fast annealing process. In this case, the annealing removes information about any possible increase of the noise in the non-annealed samples. Even

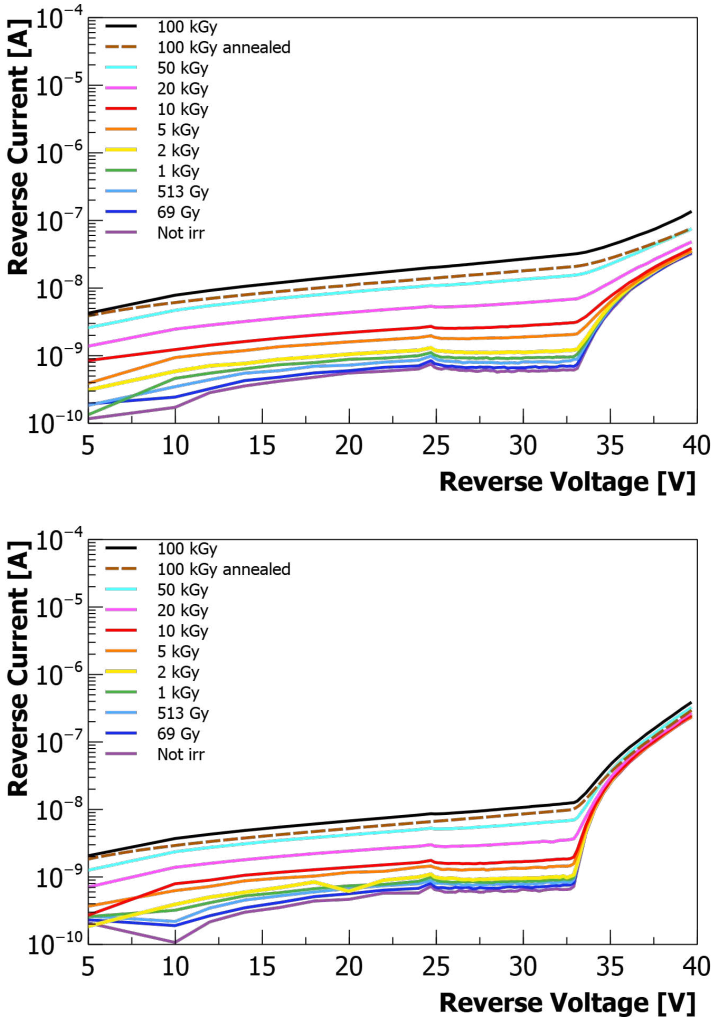

Figure 5.10: Reverse current-voltage plots with increasing radiation dose for the NUV-HD-cryo SiPMs with 20 μm (top) and 40 μm (bottom) cell pitch.

for this technology it can be useful to identify and isolate the leakage and dark components of the current, for the purpose of estimating and measuring the V_{bd} and the DCR with a good accuracy from the I-V curves.

The results are visible in Fig.5.14, where all the contribution from the direct measurements and the estimation from current measurements are shown. In the figure, the curve obtined with the pulse-counting method is slightly higher than the non-irradiated one. This might suggest an increase of the DCR but, observing the curve extracted from the dark current, the calculated DCR value is fully consistent with the non-irradiated plot. This means that

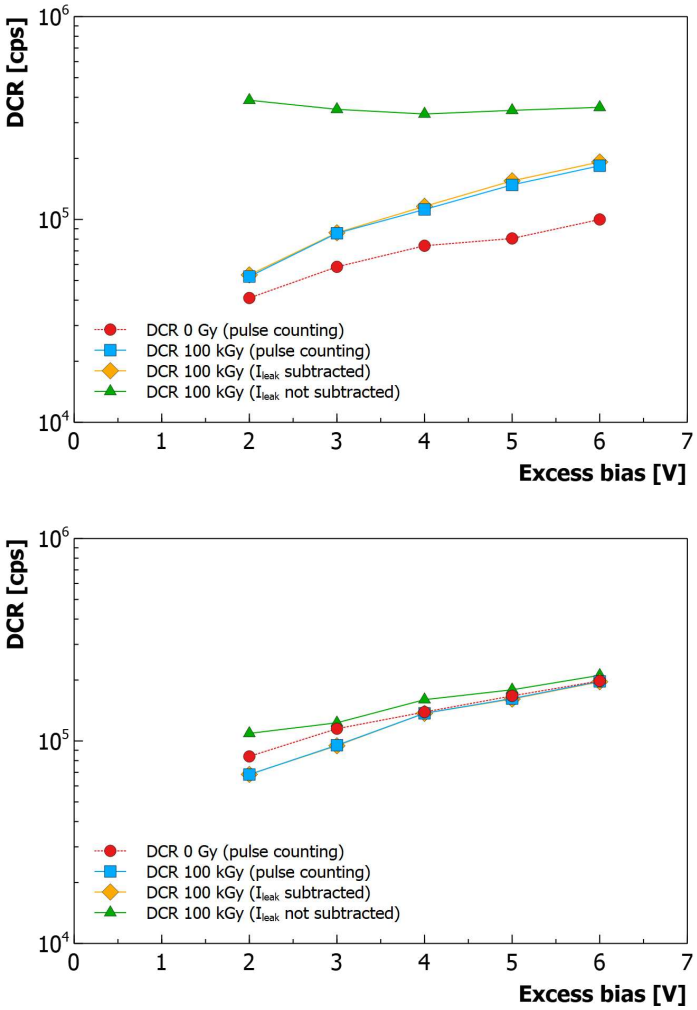

Figure 5.11: DCR as a function of the excess bias for the NUV-HD-cryo SiPMs with 20 μm and 40 μm cell pitch. Several contributions can be observed the DCR measured on the non-irradiated SiPM, the DCR estimated on the 100 kGy irradiated SiPMs from the total current (leakage and dark currents), the DCR measured at 20°C and the DCR estimated from only the dark current.

the DCR directly measured is affected by a measure uncertainty which was not identified during the measurement. Overall, the DCR can be assumed as not changing with irradiation at least in the 100 kGy annealed sample.

The PDE measurements on the RGB-HD technology showed interesting results, as visible in Fig.5.15. In this case, the comparison of the results ob-

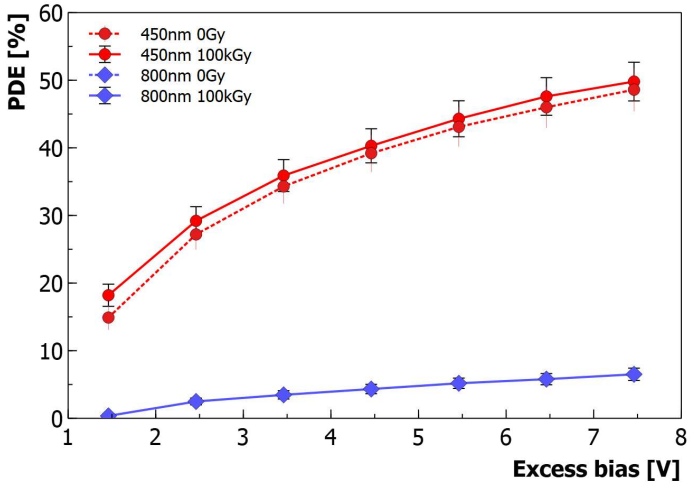

Figure 5.12: PDE as a function of the excess bias at 450 nm and 800 nm with a comparison between the irradiated and non-irradiated samples for the NUV-HD-cryo SiPM with 20 μm cell pitch.

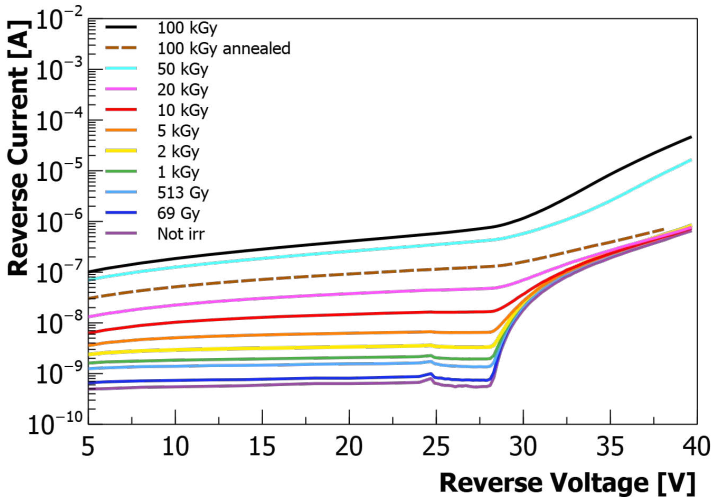

Figure 5.13: Reverse current-voltage plots with increasing radiation dose for the RGB-HD SiPM with standard 20 μm cell pitch.

tained with the standard PDE measurement, using a pulsed LED to identify dark and light counts, showed a significant variation of the PDE at both 450 nm and 800 nm. For this reason, the irradiated samples were also measured at several wavelengths by using a monochromator between 450 nm and 1100 nm. In Fig.5.15 this is visible as a oscillating curve. Fluctuations are due to

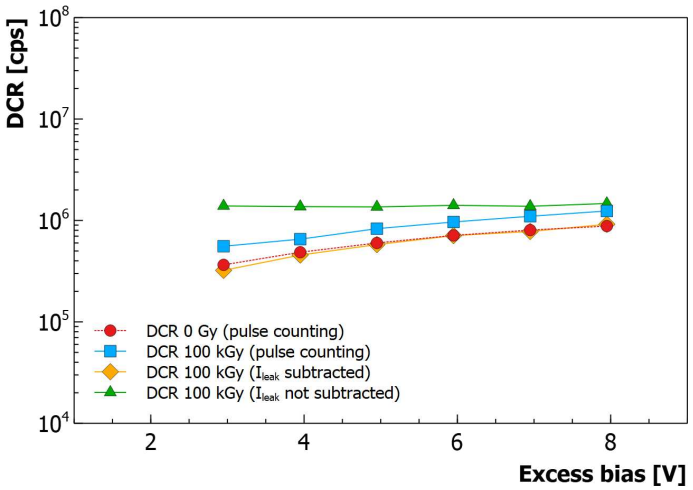

Figure 5.14: DCR as a function of the excess bias for the RGB-HD SiPM with standard 20 μm cell pitch. Several contributions can be observed the DCR measured on the non-irradiated SiPM, the DCR estimated on the 100 kGy irradiated SiPMs from the total current (leakage and dark currents), the DCR measured at 20°C and the DCR estimated from only the dark current.

the interference in the ARC on top of the active area of the SiPM microcells. This is typically smoothed in the non-irradiated device due to the protective resin on top, which was not placed on top of the irradiated samples becuse the special PCB used for irradiation did not allow it.

To take this into account, we fitted the oscillating curves obtained from the samples without protective resin with a polynomial function (straight line in figure). The smoothed PDE curves of the irradiated samples obtained in this way could then be compared to the PDE curves measured on the non irradiated samples. From the comparison of the results for irradiated and non-irradiated samples, a significant variation of the PDE can be identified at the several excess bias (or over-voltage) values. This is due to the so-called *border effect*[23]. This creates a depletion region on the internal borders of the cell, which reduces the effective fill factor with respect to the nominal value. With irradiation by X-rays, the silicon oxide, which is used to fill the deep trenches isolating adjacent cells of the SiPM (see Sec.1.4.5), gradually gets an increasing amount of positive charge. The mirror negative charge at the interface between trench and silicon enhances the border effect, thus decreasing PDE at longer wavelengths. Indeed, as described in[23], in FBK SiPM technologies, the border effect is relevant for charge that is photogenerated below the high-field region of the microcell, i.e. for longer wavelengths.

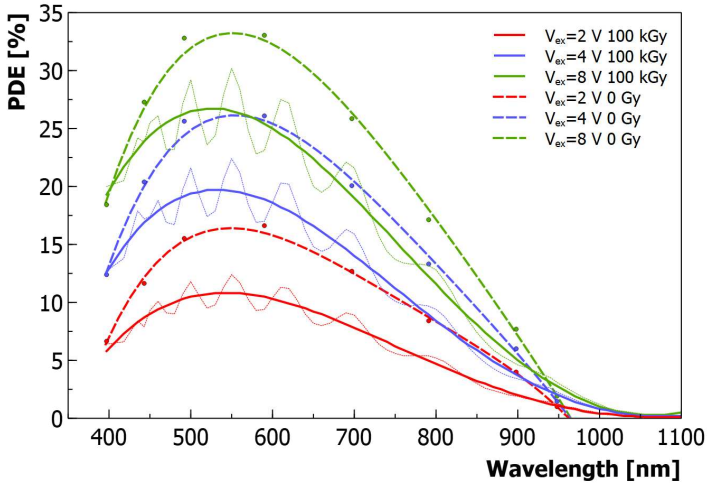

Figure 5.15: PDE as a function of the wavelength with a comparison between the irradiated (straight line) and non-irradiated (dashed line) samples using raw data and fitted data for the RGB-HD SiPM with 20 μm cell pitch.

As expected, the difference in the PDE at short wavelengths, that are absorbed near the silicon surface, is negligible, as can be seen in the figure at 400 nm. This happens because the role of the border effect in affecting charge collection and, thus, PDE near the silicon surface is negligible.

All the results presented in this section refer to the RGB-HD SiPM with standard 20 μm cell pitch but hold true also for the RGB-HD Enhanced-Border technology, where a significant decrease of the PDE is also visible, whereas DCR remains constant with irradiation.

5.3.5 VUV-HD

VUV technology consists of a p-on-n SiPM technology with some modifications, especially to the ARCs, which are modified with respect to the NUV-HD technology to detect photons in the VUV range. In particular, Silicon nitride is removed, as it would absorb photons below 250 nm.

The results of the reverse current-voltage measurements are visible in Fig.5.16, where a peculiar trend of the curve at 100 kGy after annealing can be observed. In fact, an increase of the leakage current of approximately two order of magnitude is clearly visible, in accordance with the results observed for the other technologies. However, a more pronounced divergence of the I-V curve can be noticed at about 38 V in the 100 kGy annealed and non-annealed samples.

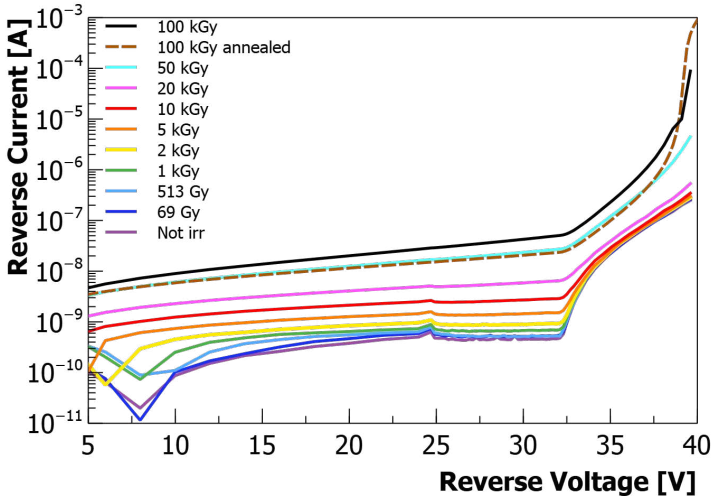

Figure 5.16: Reverse current-voltage plots with increasing radiation dose for the VUV-HD M0 SiPM with 35 μm cell pitch.

The DCR was directly measured and estimated from the current as observed above and the comparison of the results from the different methods is shown in Fig.5.17, where an increase of the DCR around one order of magnitude can be observed. From a direct measurement of the correlated noise, an increase of the Afterpulsing was found as an unexpected result. This might partially explain the divergence in the 100 kGy curves in Fig.5.16. The increase of both correlated and primary noise made their direct measurement at 20°C more complicated than the other technologies, especially at high excess bias values.

Also in this case, PDE was estimated using both LEDs and monochromator at 100 kGy and 0 Gy and the results were compared. From Fig.5.19 no significant changes can be observed, except a slight discrepancy at low wavelengths, but this might be due to the too few points considered in the non-irradiated sample using the pulsed LEDs approach. Overall, the PDE can be assumed as not changing with irradiation, at least in the visible range. Unfortunately, a measurement setup working in the VUV (e.g. below 200 nm) is not available at FBK. As a consequence of the high noise, the direct measure of the PDE resulted not straightforward, thus the maximum over-voltage value which was possible to measure was 6V.

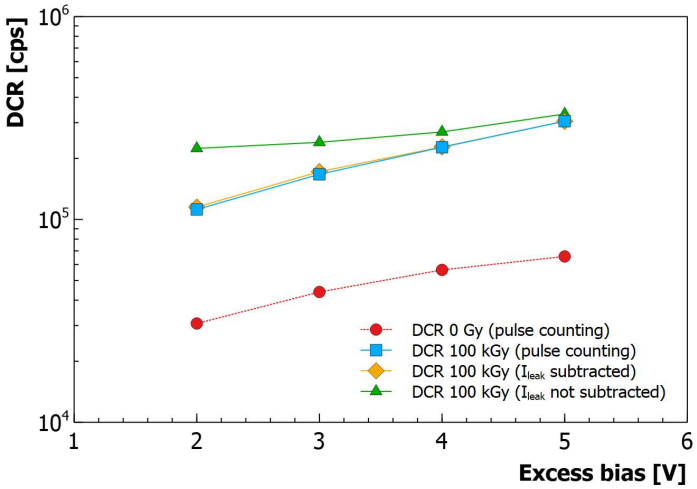

Figure 5.17: DCR as a function of the excess bias for the VUV-HD M0 SiPM with 35 μm cell pitch. Several contributions can be observed the DCR measured on the non-irradiated SiPM, the DCR estimated on the 100 kGy irradiated SiPMs from the total current (leakage and dark currents), the DCR measured at 20°C and the DCR estimated from only the dark current.

5.3.6 Annealing

After irradiation, a 30-day annealing was performed on the SiPMs, as mentioned at the beginning of this chapter. In particular, the SiPMs were left at room temperature (∼20°C) for 30 days and reverse current-voltage measurements were taken at regular time intervals of 12 hours. The results can be observed in Fig.5.20, where the normalized current is plotted as a function of the annealing time. As visible from the figure, the RGB-HD and the NUV-HD-RH technologies show the highest decrease of the current of approximately 80% after the whole annealing time interval. In particular, in the RGB-HD paragraph this feature was highlighted from the reverse current-voltage plot. Conversely, the NUV-HD-cryo exhibits the least amount of annealing, showing a decrease of the current of 30%. The slow recovery of the NUV-HD-cryo was partially expected considering that it resulted the technology less affected by the radiation damage during the test.

Overall, the annealing process shows a considerable improvement of the performance of the RGB-HD and the NUV-HD-RH SiPMs with time, which resulted the technologies most affected by the radiation damage in terms of current increase and PDE decrease, respectively.

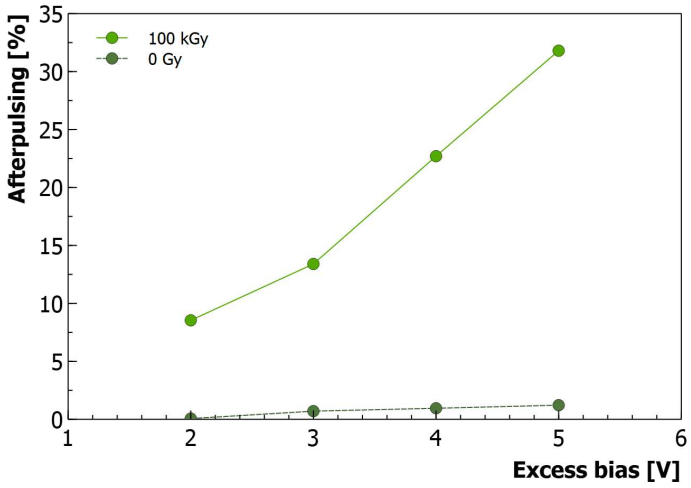

Figure 5.18: Afterpulsing as a function of the excess bias for the VUV-HD M0 SiPM with 35 μm cell pitch at 100 kGy and 0 Gy.

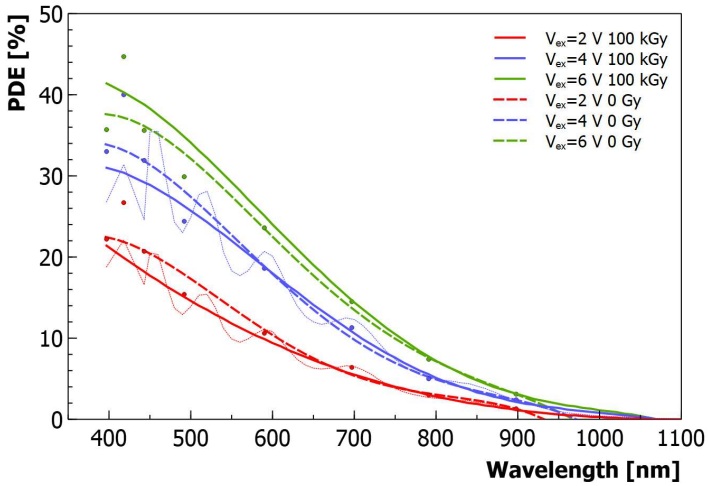

Figure 5.19: PDE as a function of the wavelength with a comparison between the irradiated (straight line) and non-irradiated (dashed line) samples using raw data and fitted data for the VUV-HD M0 SiPM with 35 μm cell pitch.

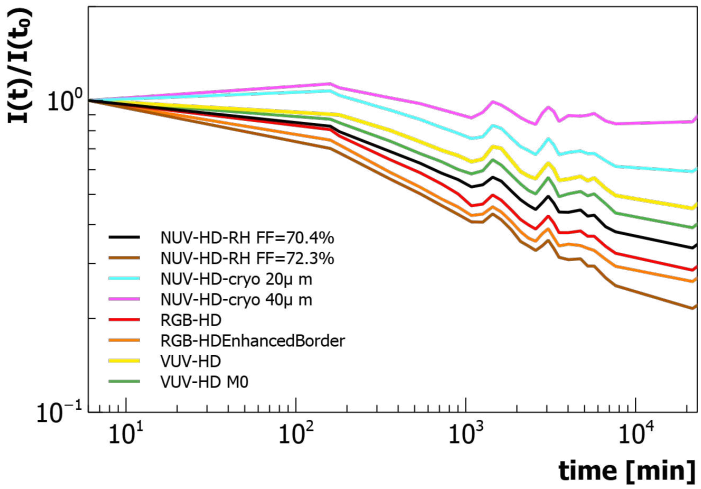

Figure 5.20: Normalized current as a function of the annealing time for the different technologies.

Chapter 6

CONCLUSION

This work aimed at investigating the radiation damage in SiPM technologies. A brief introduction of the main mechanisms of damage are described in detail in the first chapters. The main effect of the radiation damage in Silicon consists into the creation of defects affecting the performance of the detector. Depending on the nature of the particle and its energy, the damage in SiPMs can happen either on the surface or in the bulk. Surface damage generates charges into the oxide layer, resulting in a change of the electric field, thus of the breakdown voltage or it can create defects at the oxide-silicon interface, resulting into an increase of the leakage current. Bulk damage results in an increase of the noise. In particular, defects in the bulk may be caused by the displacement of Silicon Atoms called Primary Knock-on Atoms (PKA) out of their primary site in the lattice.

Defects can be divided into three main groups depending on the kinetic energy of the PKA atom:

- Point defects (or *single defects)*: $E_{K-PKA} > 25$ eV
- Cluster defects: $E_{K-PKA} > 1$ keV
- Multiple-cluster defects: $E_{K-PKA} > 12$ keV

In particular, point defects represent the simplest stage of the defects, mainly due to interstitials and vacancies, while cluster defects can be assumed as a groups of single defects following the same electrical properties and multiple-cluster defects consist into several cluster defects arranged in complex structures.

The main macroscopic effects of radiation damage expected in SiPMs are an increase of the current, both leakage current (current below the breakdown) and dark current (current above the breakdown). In particular, the

surface damage is expected to produce mainly an increase of the leakage current, whereas the bulk damage is supposed to create an increase of the dark current resulting in an increase of the noise, primary (DCR) and, in some cases, also correlated (Afterpulsing).

Three irradiation tests were carried out to investigate the main effects of the radiation damage on SiPMs.

FBK SiPMs were irradiated with 62 MeV protons at Laboratori Nazionali del Sud (LNS, INFN) in Catania (Italy) in August 2019, using a gaussian proton beam with a 1.8 cm FWHM. Several FBK technologies were tested arranged in chips dedicated to "test structures" and including 1×1 mm^2 SiPMs with different cell size. Each chip corresponding to a different technology. The chips were arranged in a single row, one behind the other, and they were placed into a plastic-printed stack. This setup produced a widening of the beam shape between the first and the last SiPM in the stack, up to 1.5 mm FWHM. This resulted in an uncertainty on the estimation of the effective fluence on each 1×1 mm^2 SiPM. SiPMs were irradiated at different fluence values, from 10^8 to 10^{13} 1 MeV n_{eq}/cm^2.

After irradiation, SiPMs were delivered to the FBK laboratories to be fully characterized, after a 30-day annealing at room temperature. From the reverse current-voltage measurement all the technologies showed a gradual increase of both leakage and dark current, as expected from theory. Although a functional characterization of the SiPMs was not always feasible due to the high noise levels reached even at moderate fluences, noise measurements on the SiPMs were performed using reverse current measurements. To extract the DCR from dark current, the so-called *current gain* was used, which takes into account the correlated noise of the SiPM and allows to estimate the DCR by dividing the dark current by the current gain. The current gain was proved not to change with irradiation, at least up to 10^{13} n_{eq}/cm^2. The DCR, as well as the reverse current, showed a gradual increase up to a saturation level when all the micro-cells appear fired at the same moment. Saturation was observed in all the technologies, starting at different fluence values from 10^{12} n_{eq}/cm^2. While the starting value of the DCR was significantly different for the different SiPM technologies under test, it was observed that the spread of the DCR value after a given amount of irradiation dose was much lower, meaning that the defects created by the radiation damage tend to overcome the intrinsic defects, responsible for the DCR of non-irradiated SiPMs due to the manufacture process. Gain, correlated noise and breakdown voltage were observed not to change with irradiation, whereas PDE showed some significant changes. Due to the high noise, a direct measurement of the PDE was not practicable, thus a responsivity measurement was required to derive some information about PDE. From the measurement on the NUV-HD and

RGB-HD technologies, a significant decrease of the responsivity was observed starting at 10^{11} n_{eq}/cm^2 for the NUV-HD SiPM with 35 μm cell and 10^{12} n_{eq}/cm^2 for the RGB-HD SiPM with 25 μm cell. Thus, PDE is affected by the radiation at high fluences, mainly due to the effects of the radiation on the quantum efficiency, as all the microcells are busy triggering DCR events and light events cannot be detected.

Activation energy of DCR was also measured in some of the technologies under test, performing reverse current-voltage measurements at different temperatures in the range $-50 \div 35$°C. Activation energy E_a was extracted from a fit of the I-T^{-1} curve in the SRH region, where the DCR is dominated by field-enhanced SRH generation statistics. Some saturation effects were observed starting from 10^{12} n_{eq}/cm^2, leading to a fictitious decrease of the E_a. This saturation effect appeared more evident in the NUV-HD SiPM with 35 μm cell. In the NUV-HD, NUV-HD-RH and RGB-HD technologies a clear decrease of the activation energy from the value of the not-irradiated sample (i.e. $0.5 \div 0.65$ eV) to the value of the samples irradiated at 10^{11} n_{eq}/cm^2 (i.e. about $0.35 \div 0.4$ eV) was observed. This behaviour might suggest the generation of some additional energy levels, bringing the observed activation energy from around mid-gap (i.e. around 0.6 eV) to a lower value, around 0.3 eV. This might be the result of the creation of vacancies and interstitial atoms due to the radiation effects. After a full characterization of the functional parameters of some of the technologies under test, an Emission Microscopy (EMMI) measurement was performed on the NUV-HD and RGB-HD samples. Emission microscopy is based on imaging of "hot carrier luminescence" (HCL), which is due to accelerated carriers suddenly losing their energy in high electric field regions. In particular, in SiPMs the emission of secondary photons happens during the avalanche process. This measurement basically consisted of an imaging of biased SiPM in Geiger mode, looking for bright spots indicating a secondary light emission. For NUV-HD and RGB-HD SiPMs irradiated at 10^{12} n_{eq}/cm^2, a preferred spatial localization was clearly visible on the borders of the cell. This might be due to the electric field shape on the cell borders or due to the damage at the SiO_2-Si interface.

Overall, during this first irradiation test all the technologies showed an increase of the current before and after the breakdown, resulting in an increase of the DCR, which reaches similar values for all the technologies up to a saturation value at 10^{12} n_{eq}/cm^2. The most important results of this irradiation test were: the linear dependence of the DCR from fluence with a slope depending on the specific technology, the convergence of the DCR of all the technologies toward similar values regardless of their starting DCR value, the decrease of the energy gap which leads to assume the creation of new defects in the bandgap and the preferred spatial localization of the de-

fects on the borders of the micro-cell. In particular, this latter result opens up the possibility of working on the layout, the dose of the dopant layers and the electric field shape to improve the radiation hardness of the SiPMs.

In February 2021, a second irradiation campaign was performed with 74 MeV protons at the Proton Therapy Center in Trento. This second irradiation campaign was aimed at testing SiPM characteristics after irradiation in view of their possible use in space mission on satellites. Thus, the dose and the steps of the irradiation were chosen accordingly. A second goal of the irradiation test was to improve the accuracy of the dose delivered to each SiPM sample, which suffered a significant degree of uncertainty in the test at LNS for different technical reasons. In this case, FBK SiPMs were placed on single custom PCBs and connected to a switching matrix located into the same irradiation room and controlled remotely to perform reverse and forward current measurements shortly after each irradiation step. This new irradiation setup aimed to avoid annealing effects between the delivery of the dose and the moment the devices were measured, to get as much information as possible about the radiation damage mechanisms. SiPMs were subjected to a gradual increase of the fluence from 7.4×10^6 n_{eq}/cm^2 to 6.4×10^{11} n_{eq}/cm^2. The irradiation setup included a dual-ring double scattering system providing a large field irradiation with a 98% uniformity on a circular area with an approximately 5.3 cm diameter. This allowed to place many SiPMs in the same irradiation spot, obtaining a uniform irradiation on all of them. Several FBK technologies were irradiated and compared: VUV-HD, NUV-HD-RH, NUV-HD-cryo, RGB-HD and NIR-HD.

From the reverse current-voltage measurements a gradual increase of the current both below and above the breakdown was observed, as expected from theory. As in the previous irradiation test, DCR was estimated from the current measurement because the high noise did not allow a direct measurement of the DCR, at least at temperatures higher than -40°C. To do this, the current gain was assumed constant with fluence. This was confirmed by a direct measurement at -40°C on samples irradiated at 10^{11} n_{eq}/cm^2. From DCR estimation, all the technologies showed a similar trend with similar values at high fluence, even starting from different DCR values. This behaviour was already seen in the previous irradiation test and was attributed to the new defects generated as a consequence of the radiation damage. The breakdown voltage, as well as the PDE, was observed not to change with irradiation up to 10^{11} n_{eq}/cm^2. Some saturation effects was observed starting at approximately 10^{11} n_{eq}/cm^2, resulting in an increase of the cell occupancy, especially in the large-sized SiPMs. The different technologies under test were compared using, as figures of merit, the Signal-to-Noise Ratio (SNR) and the energy resolution, in a specific application, which is X-

and γ-rays spectroscopy. This application was a representative example of possible space applications of SiPM aboard satellites. To estimate the SNR, three parameters should be set: fluence, flux of incident photons (at 450 nm) and integration time. The integration time was fixed at $2 \times 10^{-6}s$ taking the ALPIDE Monolithic Active Pixel Silicon sensor developed at CERN for the ALICE ITS Upgrade as an example of the application of the SiPMs in HEP. Setting the fluence at 6.4×10^{11} n_{eq}/cm^2, the trend of the SNR as a function of the number of photons showed a better performance of the large-sized SiPMs, thanks to their higher PDE and the fact that increase of noise is comparable among different cell sizes and SiPM technologies. However, they started to suffer some saturation effects from 10^{10} ph/s, whereas the small-sized SiPMs appeared less affected by saturation, thanks to a higher cell density and a faster recharge time. Keeping constant the flux of incoming photons at 10^{10} ph/s, just before saturation of the SiPM because of the light flux only (i.e. not considering the additional effect of the DCR), the SNR plot as a function of the fluence revealed better performance of the small-sized NUV technologies. Even with a higher PDE, the large-sized SiPMs are deeply affected by saturation effects which in turns, strongly limit the SNR. The energy resolution was estimated considering X-ray or γ-ray spectroscopy as possible applications for the SiPMs, keeping the integration time and the rate of incident photons constant, as in the SNR. Regardless of the scintillator under consideration, energy resolution is estimated using an integration time constant, fixed at the value required to integrate all the light emitted by the scintillator, depending on the scintillator type. It has to be pointed out that energy resolution due to the scintillator is dominated by the intrinsec contribution of the scintillator (for example, LYSO has an intrinsic contribution of 10% at 500 keV, while the the energy resolution due to the photon counting statistic and to the SiPM noise is much lower). Even in this case, plotting the energy resolution as a function of the fluence, the NUV small-sized SiPMs show the best performance with a general worsening of the energy resolution at 10^{11} n_{eq}/cm^2 for all the technologies.
All the technologies were annealed for 30 days at room temperature after irradiation. The results of the normalized current measurement after the annealing process showed the RGB-HD SiPMs to have the fastest recovery with a time constant decrease, whereas the other technologies showed a knee between 10^3 and 10^4 minutes and then a faster recovery. Apart from the RGB-HD technology, the NUV small-sized SiPMs appeared to recover the most after the whole annealing time, although they did not suffer the highest level of damage. This leads to the conclusion that, overall, the small-sized NUV-HD-RH (15-20 μm) and NUV-HD-cryo (20 μm) technologies remain the best choice for the applications considered in this thesis. In particular,

the small-sized SiPMs have the considerable advantage of having a smaller cell occupancy, a low saturation, a lower power consumption and a lower correlated noise, all features that are favorable in many applications.

A third irradiation test was performed on FBK SiPMs in May 2021 with X-rays at TIFPA (INFN) irradiation facility in Trento, equipped with an X-ray source featuring a tungsten (W) anode and producing four emission lines, $K-\alpha,\beta$ and $L-\alpha,\beta$. Among these lines, the L lines (7-12 keV) are considered the most appropriate ones for tests on silicon sensors due to the small thickness of the silicon devices. During the irradiation, the SiPMs were placed on the same custom PCB used in the proton irradiation tests described above, and they were arranged in "test structure" dies containing single $1 \times 1\ mm^2$ SiPMs with different cell sizes. The PCB was equipped with a dosimetric probe and placed into a cabinet. The sensors were irradiated with increasing doses up to 100 kGy. The SiPMs on the PCB were connected to the acquisition system placed outside the cabinet and controlled remotely. Reverse current-voltage measurements were performed shortly after each irradiation step, to minimize any annealing effect. Several FBK technologies were irradiated: NUV-HD-RH SiPMs with 12.5-15-20 μm cell pitch and different fill factors, NUV-HD-cryo SiPMs with 15-20-40 μm cell pitch, VUV-HD SiPMs with 35 μm cell pitch with and without mask (a special layout split aimed at enhanced timing response), RGB-HD SiPMs with 20 μm cell pitch with and without enhanced border. An increase of the leakage current was expected form theory as a result of a surface damage, while no significant damage effects were expected in the bulk of the SiPM.

The NUV-HD-RH technology showed a gradual increase of the current below and above the breakdown. An increase of the leakage current (i.e. below breakdown) was expected but the increase of the dark current (i.e. above breakdown) required some further investigations, especially with regard to its connection with the DCR. A DCR measurement was performed at 20°C and the results were compared to the DCR estimated from reverse, dark current divided by the current gain. From the comparison of the two results, a discrepancy was clearly visible. In fact, it is wrong to assume the current above the breakdown as a purely generated by the dark counts of the devices (i.e. the pulses generated in geiger-mode) when the leakage current is very high. The solution was found by fitting the leakage current below the breakdown with a third degree polynomial and then subtracting the extrapolated leakage current component to the total current above the breakdown to obtain a more accurate estimate of the current generated by the dark counts. Results from the DCR estimated from the corrected dark current was in accordance with the DCR values obtained from functional characterization (waveform analysis), showing an increase of approximately

one order of magnitude at the maximum irradiation dose. This may indicate that the increase of the leakage current is so big that part of it reaches the high-field region of the microcell and gets multiplied, thus generating dark counts. On the other hand, other explanations are possible, including a modification of the electric field inside the microcell because of the build-up of positive charge in the dielectric layers, inducing a "soft" breakdown at the microcell edges. Distinguishing between the different hypotheses would require additional work, including simulation of the electric field inside the microcells, which is outside the scope of this thesis. PDE was measured at room temperature with pulsed LEDs, emitting photons at 450 nm and 800 nm, and no significant changes were observed.

For the NUV-HD-cryo technology, a small-sized SiPM with 20 μm cell and a large-sized SiPM with 40 μm cell were considered. In both cases an increase of the reverse current was observed, whereas DCR showed a slight increase only in the SiPM with 40 μm cell pitch. This difference might be due to the lower impact of the charge into the trench due to the small perimeter-area ratio than the small-sized SiPM. Even in the NUV-HD-cryo technology, no significant changes in the PDE were observed at 450 nm and 800 nm.

For the RGB-HD technology, the SiPM with standard 20 μm cell pitch was characterized in detail. An increase of the reverse dark current was observed also in this case, up to two order of magnitude. DCR was directly measured and estimated from the effective dark current with the leakage current subtracted, showing no relevant variations with respect to the non-irradiated values. The most interesting results were observed in the PDE measurement, carried out using a monochromator at several wavelengths in the range 450$\div$1100 nm. Results showed a significant decrease of the PDE, especially at long wavelengths. This was attributed to the enhancement of the so-called "border effect", caused by the positive charge build-up in the dielectric layers used to fill the trenches between microcells. The induced electric field reduced the charge collection efficiency of the microcell for charge generated below the high-field region, reducing the effective fill-factor and, thus, the PDE for impinging photons with longer wavelengths, which are absorbed also in this region (as opposed to short-wavelength photons, for example at 400 nm). This effect gets relevant in the n-on-p based junctions, as in the case of the RGB technology, while it is not visible in p-on-n technologies, such as the NUV-HD.

For the VUV-HD technology, the SiPM with 35 μm cell with mask was fully characterized. In the VUV-HD technology a gradual increase of the current with the irradiation dose, consistent with the results of the other technologies, was observed. In addition, the DCR curve of the sample at 100 kGy, measured after annealing, was observed to strongly deviate at high

excess biases from the DCR measured before irradiation. From waveform analysis measurements, it was possible to attribute this divergence to a significant increase of the afterpulsing probability at high excess bias. This result is interesting as it represents the only instance in which an increase of correlated noise was observed after irradiation with X-rays. Also in this case, differences in oxide charge as well as increased number of defects at the silicon-silicon oxide interface are possible candidates to explain the phenomenon, in particular considering that the main differences between the NUV-HD and the VUV-HD technologies are in the ARCs. PDE was also measured on VUV-HD and no significant changes with the irradiation dose were found.

After describing in detail all the irradiation tests with ionizing and non-ionizing radiation, some final conclusion can be drawn. SiPMs represent a very reliable sensor for many applications in HEP in terms of radiation hardness. As an example, the Inner Tracking System (ITS3) of the ALICE experiment at CERN expected for the next LHC Long Shutdown (LS3) can be considered. This includes the ALPIDE Monolithic Active Pixel Silicon sensor previously introduced in Ch.4, which is expected to survive radiation levels well below 10^{13} n_{eq}/cm^2 (NIEL) and 10kGy (TID)[84]. From the irradiation tests described in this work on the FBK SiPMs, almost all the technologies were observed to survive to such levels for both ionizing and non-ionizing radiations. If considering as another example the next MIP Timing Detector (MTD) of the Phase II upgrade of the CMS detector at CERN, this requires a few comments. The MTD will consist of a Barrel Timing Layer (BTL) and an Endcap Timing Layer (ETL). In particular, the BTL is expected to receive a radiation quantity in the order of 2×10^{14} n_{eq}/cm^2[85] over the whole detector operation time, whereas the ETL is expected to receive a fluence of about 2×10^{15} n_{eq}/cm^2[85]. In this case, separate considerations should be made for each section. In this work, SiPMs were tested up to a fluence in the order of 10^{13} n_{eq}/cm^2, where they reached a DCR saturation level at around 10^{12} n_{eq}/cm^2, mainly due to the increase of the noise and their small size (1×1 mm^2 SiPMs were tested here). Due to the long detector operation time, a long annealing should be taken into consideration which could significantly reduce the noise level. For these reasons, it cannot be concluded here that SiPMs are well suited for this application but definitely they might be investigated for this purpose. Regarding the ETL, this seems a way more complicated situation, since 10^{15} n_{eq}/cm^2 represents a very high limit for SiPMs, at least on the results emerging from this work. Instead, for what concerns possible space applications of the SiPMs, an example is provided in Ch.4, assuming a circular Low Earth Orbit in its worst-scenario case

(Polar Orbit). In this case, SiPMs were observed to survive to medium-high fluences under the assumption of a proper shielding. In particular, NUV-HD technology appears to suit most in case of non-ionizing dose, showing an higher SNR and a better energy resolution, at least as regards the applications taken into account in this thesis. From the results of the tests with ionizing radiation, the NUV-HD technology results the most promising one in terms of PDE, which is observed to change only in n-on-p based technologies. Among the different NUV technologies considered into this work, the NUV-HD-RH and the NUV-HD-cryo appear the most interesting ones, especially with small cell size, which can guarantee a lower saturation, thus a weaker dependence of their performance on the increase of the SiPM noise (mainly its DCR). In particular, they seem to have similar performance when subjected to non-ionizing radiation, whereas the NUV-HD-cryo is the only technology not to show an increase either of the noise and the PDE when tested with ionizing radiation. Overall, both can be assumed as the most suitable FBK technologies for applications requiring radiation hardness, so far.

6.1 What's next?

So far, SiPMs were tested only with protons and X-rays but additional information on the radiation damage could be derived testing them with other particles. As an example, irradiating the SiPMs with neutrons and low-energy X-rays could help isolating the bulk damage from the surface damage. The results could be compared to the effects of protons (producing both surface and bulk damage) on the same technologies. This could allow to spot new possible damage mechanisms depending on the interaction of that specific particle with silicon, including potential interaction mechanisms with the high electric field inside the SiPMs.

Another aspect which was not possible to investigate was the impact of the particle energy on the main functional parameters of a SiPM. Furthermore, depending on the dopant profiles of each FBK SiPM technology, the DLTS method might be adapted to SiPMs to obtain at least a shallow defects characterization which could lead to understand the single and cluster defects dynamic in such a complex structure as a SiPM.

In addition, the study of the spatial localization of defects inside the single micro-cell through the EMMI imaging technique could be extended to other FBK technologies, searching for potential connections with the different SiPM layouts and doping profiles.

It is not easy to carry on such a complex subject which requires long

times to get some results. This thesis aimed to pave the way for future research on the next generation of radiation hardened FBK technologies, humbly pretending to be considered as a good starting point for what will come next.

Ringraziamenti

Questo lavoro di tesi, che con troppa presunzione porta solo il mio nome, è in realtà un lavoro condiviso con diverse persone che meritano di essere non solo citate ma anche ringraziate, per il loro supporto materiale ed emotivo in questi tre anni.

Il primo ringraziamento va senza dubbio al mio supervisore Alberto, non solo per avermi dato la preziosa possibilità di intraprendere questo meraviglioso viaggio ma anche per averne condiviso con me una parte, per non avermi mai privata del confronto, ed averlo sempre affrontato con onestà.

Grazie a Fabio, da cui ho imparato tanto, tutto. Avrei voluto più tempo per tutte le domande che non sono riuscita a fargli, e per poterle rifare più volte, come al solito. Grazie per l'immensa pazienza, la spietata sincerità e la tenera umanità, doti troppo spesso sottovalutate in un ambiente competitivo come la ricerca.

Grazie a Veronica, mia prima mentore e amica in FBK. Grazie per avermi spronata ad andare avanti e cercare il sole nonostante la pioggia incessante. Alla fine il sole è arrivato, e ha portato un panorama bellissimo.

Grazie a Gabriele, collega, amico. Grazie per essere sempre stato in ascolto. Non mi sono mai sentita sola in questi anni sapendoti vicino. Grazie per aver gioito delle mie vittorie e avermi consolata nelle sconfitte, nel lavoro e nella vita.

Grazie ad Andrea, Elena, Stefano e Stella, per esserci stati sempre, soprattutto quando non credevo di averne bisogno.

Grazie ad Michele, Carina, Alberto M., Giacomo, Vlad, Massimo e Nicola, per avermi accompagnata in questo percorso di lavoro e di vita.

Grazie a Benedetto, che di questa tesi ha condiviso una buona parte, senza mai farmi mancare il supporto e la stima.

Grazie a Giulia, amica, sorella. Grazie per gli abbracci, la protezione e l'affetto di cui mi hai circondata. Non importa quanto lontane saremo da domani, ovunque io sarò, per te sarà sempre casa.

Grazie a Pietro, per così tante cose che non saprei da dove iniziare. Mi limiterò a ringraziarti per aver condiviso con me la casa, il divano e, soprat-

tutto, il tempo.

Grazie a Daniele, Marzia e Valeria, persone meravigliose con cui poter essere se stessi. Grazie per avermi donato uno sguardo nuovo sul mondo, più essenziale e più profondo.

Grazie a Alessia, Bea e Fabrizia, per essermi sempre accanto nonostante la distanza. Grazie per essere certezza, porto sicuro in cui rifugiarsi durante la tempesta.

Grazie a Laura, per la poesia e per la prosa.

Grazie a Pippo, Mariapia, Carla, Tiziana e Annalisa per essere compagni di strada da tutta la vita, anche a distanza. Amici preziosi, amici con cui crescere, amici da cui tornare.

Grazie allə compagnə di Possibile Trentino-Alto Adige, per aver condiviso con me progetti, idee e ideali.

Per ultimo un grande grazie alla mia fagmiglia, ai miei genitori Carmela e Franco per avermi accompagnata fino a qui, e ai miei fratelli Gianni, Tony e Maurizio, per non cercare affannosamente di essere la famiglia perfetta ma per farmi ogni giorno il regalo più bello: esserci.

Diverse altre persone non sono state ringraziate singolarmente ma vorrei sapessero che non le ho dimenticate. Ricordo ognuno dei loro sguardi, messaggi, abbracci e sorrisi. E li porto nel cuore, là dove entrano solo le cose belle, là dove le cose belle restano per sempre.

Bibliography

[1] "Photomultiplier tube," Jan 2022. [Online]. Available: https://en.wikipedia.org/wiki/Photomultiplier_tube#History

[2] R. Jöhren, R. Berendes, W. Buglak, D. Hampf, V. Hannen, J. Mader, W. Nörtershäuser, R. Sánchez, and C. Weinheimer, "Apds as single-photon detectors for visible and near-infrared wavelengths down to hz rates," *Journal of Instrumentation*, vol. 7, no. 02, p. P02015–P02015, Feb 2012. [Online]. Available: http://dx.doi.org/10.1088/1748-0221/7/02/P02015

[3] D. S. Bethune, W. P. Risk, and G. W. Pabst, "A high-performance integrated single-photon detector for telecom wavelengths," *Journal of Modern Optics*, vol. 51, no. 9-10, pp. 1359–1368, 2004. [Online]. Available: https://doi.org/10.1080/09500340408235278

[4] G. Lutz and R. Klanner, *Solid State Detectors*. Cham: Springer International Publishing, 2020, pp. 137–200. [Online]. Available: https://doi.org/10.1007/978-3-030-35318-6_5

[5] G. Llosa, N. Belcari, M. G. Bisogni, G. Collazuol, A. D. Guerra, S. Marcatili, S. Moehrs, and C. Piemonte, "Silicon photomultipliers and sipm matrices as photodetectors in nuclear medicine," in *2007 IEEE Nuclear Science Symposium Conference Record*, vol. 5, 2007, pp. 3220–3223.

[6] E. Garutti, "Silicon photomultipliers for high energy physics detectors," *Journal of Instrumentation*, vol. 6, no. 10, pp. C10 003–C10 003, oct 2011. [Online]. Available: https://doi.org/10.1088%2F1748-0221%2F6%2F10%2Fc10003

[7] R. Zimmermann, F. Braun, T. Achtnich, O. Lambercy, R. Gassert, and M. Wolf, "Silicon photomultipliers for improved detection of low light levels in miniature near-infrared spectroscopy instruments," *Biomedical optics express*, vol. 4, pp. 659–66, 05 2013.

[8] A. D. Mora, E. Martinenghi, D. Contini, A. Tosi, G. Boso, T. Durduran, S. Arridge, F. Martelli, A. Farina, A. Torricelli, and A. Pifferi, "Fast silicon photomultiplier improves signal harvesting and reduces complexity in time-domain diffuse optics," *Opt. Express*, vol. 23, no. 11, pp. 13 937–13 946, Jun 2015. [Online]. Available: http://www.opticsexpress.org/abstract.cfm?URI=oe-23-11-13937

[9] K. T. Son and C. C. Lee, "Multiple-target laser rangefinding receiver using a silicon photomultiplier array," *IEEE Transactions on Instrumentation and Measurement*, vol. 59, no. 11, pp. 3005–3011, 2010.

[10] "The Phase-2 Upgrade of the CMS Barrel Calorimeters," CERN, Geneva, Tech. Rep., Sep 2017, this is the final version, approved by the LHCC. [Online]. Available: https://cds.cern.ch/record/2283187

[11] Wikipedia, "Permittivity — wikipedia, l'enciclopedia libera," 2021, [Online; controllata il 4-August-2021]. [Online]. Available: https://en.wikipedia.org/wiki/Permittivity

[12] F. Acerbi and S. Gundacker, "Understanding and simulating sipms," *Nuclear Instruments and Methods in Physics Research Section A: Accelerators, Spectrometers, Detectors and Associated Equipment*, vol. 926, pp. 16–35, 2019, silicon Photomultipliers: Technology, Characterisation and Applications. [Online]. Available: https://www.sciencedirect.com/science/article/pii/S0168900218317704

[13] G. Paternoster, L. Ferrario, F. Acerbi, A. G. Gola, and P. Bellutti, "Silicon photomultipliers technology at fondazione bruno kessler and 3d integration perspectives," in *ESSDERC 2019 - 49th European Solid-State Device Research Conference (ESSDERC)*, 2019, pp. 50–53.

[14] S. Vinogradov, A. Arodzero, R. Lanza, and C. Welsch, "Sipm response to long and intense light pulses," *Nuclear Instruments and Methods in Physics Research Section A: Accelerators, Spectrometers, Detectors and Associated Equipment*, vol. 787, pp. 148–152, 2015, new Developments in Photodetection NDIP14. [Online]. Available: https://www.sciencedirect.com/science/article/pii/S0168900214013850

[15] Advansid, "Introduction to sipms," Advansid, Tech. Rep. 2, 9 2014.

[16] C. Piemonte and A. Gola, "Overview on the main parameters and technology of modern Silicon Photomultipliers," *Nuclear Instruments and Methods in Physics Research A*, vol. 926, pp. 2–15, May 2019.

[17] G. Hurkx, D. Klaassen, and M. Knuvers, "A new recombination model for device simulation including tunneling," *IEEE Transactions on Electron Devices*, vol. 39, no. 2, pp. 331–338, 1992.

[18] M. Ghioni, A. Gulinatti, I. Rech, F. Zappa, and S. Cova, "Progress in silicon single-photon avalanche diodes," *IEEE Journal of Selected Topics in Quantum Electronics*, vol. 13, no. 4, pp. 852–862, 2007.

[19] A. Lacaita, F. Zappa, S. Bigliardi, and M. Manfredi, "On the bremsstrahlung origin of hot-carrier-induced photons in silicon devices," *IEEE Transactions on Electron Devices*, vol. 40, no. 3, pp. 577–582, 1993.

[20] A. Nepomuk Otte, "On the efficiency of photon emission during electrical breakdown in silicon," *Nuclear Instruments and Methods in Physics Research Section A: Accelerators, Spectrometers, Detectors and Associated Equipment*, vol. 610, no. 1, pp. 105–109, 2009, new Developments In Photodetection NDIP08. [Online]. Available: https://www.sciencedirect.com/science/article/pii/S0168900209010390

[21] A. Gola, C. Piemonte, and A. Tarolli, "The dled algorithm for timing measurements on large area sipms coupled to scintillators," *IEEE Transactions on Nuclear Science*, vol. 59, no. 2, pp. 358–365, 2012.

[22] F. Acerbi, G. Paternoster, A. Gola, N. Zorzi, and C. Piemonte, "Silicon photomultipliers and single-photon avalanche diodes with enhanced nir detection efficiency at fbk," *Nuclear Instruments and Methods in Physics Research Section A: Accelerators, Spectrometers, Detectors and Associated Equipment*, vol. 912, pp. 309–314, 2018, new Developments In Photodetection 2017. [Online]. Available: https://www.sciencedirect.com/science/article/pii/S0168900217313542

[23] F. Acerbi, A. Gola, V. Regazzoni, G. Paternoster, G. Borghi, N. Zorzi, and C. Piemonte, "High efficiency, ultra-high-density silicon photomultipliers," *IEEE Journal of Selected Topics in Quantum Electronics*, vol. 24, no. 2, pp. 1–8, 2018.

[24] G. Gallina, F. Retière, P. Giampa, J. Kroeger, P. Margetak, S. Byrne Mamahit, A. De St. Croix, F. Edaltafar, L. Martin, N. Massacret, M. Ward, and G. Zhang, "Characterization of sipm avalanche triggering probabilities," *IEEE Transactions on Electron Devices*, vol. 66, no. 10, pp. 4228–4234, 2019.

[25] W. G. Oldham, P. Antognetti, and R. R. Samuelson, "New method for breakdown voltage determination in p-n junctions," *Applied Physics Letters*, vol. 19, no. 466, 1971.

[26] W. Oldham, R. Samuelson, and P. Antognetti, "Triggering phenomena in avalanche diodes," *IEEE Transactions on Electron Devices*, vol. 19, no. 9, pp. 1056–1060, 1972.

[27] G. Gallina, F. Retiere, P. Giampa, J. Kroeger, P. Margetak, S. Byrne Mamahit, A. De St. Croix, F. Edaltafar, L. Martin, N. Massacret, and et al., "Characterization of sipm avalanche triggering probabilities," *IEEE Transactions on Electron Devices*, vol. 66, no. 10, p. 4228–4234, Oct 2019. [Online]. Available: http://dx.doi.org/10.1109/TED.2019.2935690

[28] *p-n Junctions*. John Wiley Sons, Ltd, 2006, pp. 77–133. [Online]. Available: https://onlinelibrary.wiley.com/doi/abs/10.1002/9780470068328.ch2

[29] F. Acerbi, A. Ferri, G. Zappala, G. Paternoster, A. Picciotto, A. Gola, N. Zorzi, and C. Piemonte, "Nuv silicon photomultipliers with high detection efficiency and reduced delayed correlated-noise," *IEEE Transactions on Nuclear Science*, vol. 62, no. 3, pp. 1318–1325, 2015.

[30] C. Piemonte, F. Acerbi, A. Ferri, A. Gola, G. Paternoster, V. Regazzoni, G. Zappala, and N. Zorzi, "Performance of nuv-hd silicon photomultiplier technology," *IEEE Transactions on Electron Devices*, vol. 63, no. 3, pp. 1111–1116, 2016.

[31] S. Vinogradov, "Perfomance of Silicon Photomultipliers in photon number and time resolution," *PoS*, vol. PhotoDet2015, p. 002, 2016.

[32] R. Newman, "Visible light from a silicon $p - n$ junction," *Phys. Rev.*, vol. 100, pp. 700–703, Oct 1955. [Online]. Available: https://link.aps.org/doi/10.1103/PhysRev.100.700

[33] D. J. Rose, "Microplasmas in silicon," *Phys. Rev.*, vol. 105, pp. 413–418, Jan 1957. [Online]. Available: https://link.aps.org/doi/10.1103/PhysRev.105.413

[34] J. Shewchun and L. Wei, "Mechanism for reverse-biased breakdown radiation in p-n junctions," *Solid-State Electronics*, vol. 8, no. 5, pp. 485–493, 1965. [Online]. Available: https://www.sciencedirect.com/science/article/pii/0038110165900249

[35] C. Piemonte, "A new silicon photomultiplier structure for blue light detection," *Nuclear Instruments and Methods in Physics Research Section A: Accelerators, Spectrometers, Detectors and Associated Equipment*, vol. 568, no. 1, pp. 224–232, 2006, new Developments in Radiation Detectors. [Online]. Available: https://www.sciencedirect.com/science/article/pii/S016890020601271X

[36] C. Piemonte, R. Battiston, M. Boscardin, G.-F. Dalla Betta, A. Del Guerra, N. Dinu, A. Pozza, and N. Zorzi, "Characterization of the first prototypes of silicon photomultiplier fabricated at itc-irst," *IEEE Transactions on Nuclear Science*, vol. 54, no. 1, pp. 236–244, 2007.

[37] A. Ferri, A. Gola, C. Piemonte, T. Pro, N. Serra, A. Tarolli, and N. Zorzi, "First results on NUV-SiPMs at FBK," *Nucl. Instrum. Meth. A*, vol. 718, pp. 371–372, 2013.

[38] T. Pro, A. Ferri, A. Gola, N. Serra, A. Tarolli, N. Zorzi, and C. Piemonte, "New developments of near-uv sipms at fbk," *IEEE Transactions on Nuclear Science*, vol. 60, no. 3, pp. 2247–2253, 2013.

[39] F. Acerbi, G. Paternoster, M. Capasso, M. Marcante, A. Mazzi, V. Regazzoni, N. Zorzi, and A. Gola, "Silicon photomultipliers: Technology optimizations for ultraviolet, visible and near-infrared range," *Instruments*, vol. 3, no. 1, 2019. [Online]. Available: https://www.mdpi.com/2410-390X/3/1/15

[40] F. Acerbi, A. Ferri, G. Zappala, G. Paternoster, A. Picciotto, A. Gola, N. Zorzi, and C. Piemonte, "Nuv silicon photomultipliers with high detection efficiency and reduced delayed correlated-noise," *IEEE Transactions on Nuclear Science*, vol. 62, no. 3, pp. 1318–1325, 2015.

[41] F. Acerbi, A. Gola, V. Regazzoni, G. Paternoster, G. Borghi, N. Zorzi, and C. Piemonte, "High efficiency, ultra-high-density silicon photomultipliers," *IEEE Journal of Selected Topics in Quantum Electronics*, vol. 24, no. 2, pp. 1–8, 2018.

[42] F. Acerbi, S. Davini, A. Ferri, C. Galbiati, G. Giovanetti, A. Gola, G. Korga, A. Mandarano, M. Marcante, G. Paternoster, and et al., "Cryogenic characterization of fbk hd near-uv sensitive sipms," *IEEE Transactions on Electron Devices*, vol. 64, no. 2, p. 521–526, Feb 2017. [Online]. Available: http://dx.doi.org/10.1109/TED.2016.2641586

[43] T. C. collaboration, C. Adloff, Y. Karyotakis, J. Repond, A. Brandt, H. Brown, K. De, C. Medina, J. Smith, J. Li, and et al., "Construction

and commissioning of the calice analog hadron calorimeter prototype," *Journal of Instrumentation*, vol. 5, no. 05, p. P05004–P05004, May 2010. [Online]. Available: http://dx.doi.org/10.1088/1748-0221/5/05/P05004

[44] "The t2k experiment," *Nuclear Instruments and Methods in Physics Research Section A: Accelerators, Spectrometers, Detectors and Associated Equipment*, vol. 659, no. 1, pp. 106–135, 2011. [Online]. Available: https://www.sciencedirect.com/science/article/pii/S0168900211011910

[45] F. Simon, "Silicon photomultipliers in particle and nuclear physics," *Nuclear Instruments and Methods in Physics Research Section A: Accelerators, Spectrometers, Detectors and Associated Equipment*, vol. 926, pp. 85–100, 2019, silicon Photomultipliers: Technology, Characterisation and Applications. [Online]. Available: https://www.sciencedirect.com/science/article/pii/S0168900218316176

[46] G. W. Simon, J. M. Denney, and R. G. Downing, "Energy dependence of proton damage in silicon," *Phys. Rev.*, vol. 129, pp. 2454–2459, Mar 1963. [Online]. Available: https://link.aps.org/doi/10.1103/PhysRev.129.2454

[47] A. Lechner, "Particle interactions with matter," *CERN Yellow Rep. School Proc.*, vol. 5, p. 47, 2018.

[48] L. Gonella, "TID Tolerance of commercial 130nm CMOS Technologies for HEP experiments," 2006, presented 27 Oct 2006. [Online]. Available: https://cds.cern.ch/record/2252791

[49] E. Garutti and Y. Musienko, "Radiation damage of SiPMs," *Nucl. Instrum. Meth. A*, vol. 926, pp. 69–84, 2019.

[50] M. Moll, "Radiation damage in silicon particle detectors: Microscopic defects and macroscopic properties," Ph.D. dissertation, Hamburg U., 1999.

[51] G. H. Kinchin and R. S. Pease, "The displacement of atoms in solids by radiation," *Reports on Progress in Physics*, vol. 18, no. 1, pp. 1–51, jan 1955. [Online]. Available: https://doi.org/10.1088/0034-4885/18/1/301

[52] J. Erfle, "Irradiation study of different silicon materials for the cms tracker upgrade," 2014.

[53] M. Huhtinen, "Simulation of non-ionising energy loss and defect formation in silicon," *Nuclear Instruments and Methods in Physics Research Section A: Accelerators, Spectrometers, Detectors and Associated Equipment*, vol. 491, no. 1, pp. 194–215, 2002. [Online]. Available: https://www.sciencedirect.com/science/article/pii/S0168900202012275

[54] A. Junkes and DESY, "Influence of radiation induced defect clusters on silicon particle detectors; 1st edition," Dr., Universität Hamburg, Hamburg, 2011, universität Hamburg, Diss., 2011. [Online]. Available: https://bib-pubdb1.desy.de/record/89366

[55] B. R. Cossick, "Disordered regions in semiconductors bombarded by fast neutrons," *Journal of Applied Physics (U.S.)*. [Online]. Available: https://www.osti.gov/biblio/4238099

[56] E. M. Donegani, "Energy-Dependent Proton Damage in Silicon," Dr., Universität Hamburg, Hamburg, 2017, universität Hamburg, Diss., 2017. [Online]. Available: https://bib-pubdb1.desy.de/record/333246

[57] V. Eremin, E. Verbitskaya, and Z. Li, "The origin of double peak electric field distribution in heavily irradiated silicon detectors," *Nucl. Instrum. Meth. A*, vol. 476, pp. 556–564, 2002.

[58] T. Matsubara, H. Tanaka, K. Nitta, and M. Kuze, "Radiation damage of MPPC by gamma-ray irradiation with Co-60," *PoS*, vol. PD07, p. 032, 2006.

[59] S. Sánchez Majos, P. Achenbach, C. Ayerbe Gayoso, J. Bernauer, R. Böhm, M. Distler, M. Gómez Rodríguez de la Paz, H. Merkel, U. Müller, L. Nungesser, J. Pochodzalla, B. Schlimme, T. Walcher, M. Weinriefer, and C. Yoon, "Noise and radiation damage in silicon photomultipliers exposed to electromagnetic and hadronic radiation," *Nuclear Instruments and Methods in Physics Research Section A: Accelerators, Spectrometers, Detectors and Associated Equipment*, vol. 602, no. 2, pp. 506–510, 2009. [Online]. Available: https://www.sciencedirect.com/science/article/pii/S0168900209000643

[60] M. C. Vignali, V. Chmill, E. Garutti, R. Klanner, M. Nitschke, J. Schwandt, and S. Sonder, "Neutron induced radiation damage of ketek sipms," in *2016 IEEE Nuclear Science Symposium, Medical Imaging Conference and Room-Temperature Semiconductor Detector Workshop (NSS/MIC/RTSD)*, 2016, pp. 1–5.

[61] L. Calabretta *et al.*, "Invited paper: Commissioning of the k800 infn cyclotron," in *Proc. 14th Int. Cyclotron Conf. and Their Applications (Cyclotrons'95)*. JACoW Publishing, Oct. 1995, paper A-02, pp. 12–19.

[62] A. Calanna, "High-intensity extraction from the superconducting cyclotron at lns-infn," *Nuovo Cim. C*, vol. 40, no. 2, p. 101, 2017.

[63] D. L. Vincenzo, "Ciclotrone superconduttore - infn - laboratori nazionali del sud," Nov 2017. [Online]. Available: https://www.lns.infn.it/it/acceleratori/ciclotrone-superconduttore.html

[64] G. Gallo, L. Allegra, G. Costa, E. Messina, and E. Zappalà, "Mechanical aspects of the lns superconducting cyclotron upgrade," 2017.

[65] N. Iwasa, H. Geissel, G. Münzenberg, C. Scheidenberger, T. Schwab, and H. Wollnik, "Mocadi, a universal monte carlo code for the transport of heavy ions through matter within ion-optical systems," *Nuclear Instruments and Methods in Physics Research Section B: Beam Interactions with Materials and Atoms*, vol. 126, no. 1, pp. 284–289, 1997, international Conference on Electromagnetic Isotope Separators and Techniques Related to Their Applications. [Online]. Available: https://www.sciencedirect.com/science/article/pii/S0168583X97010975

[66] H. Weick *et al.*, "Slowing down of relativistic few electron heavy ions," *Nucl. Instrum. Meth. B*, vol. 164-165, pp. 168–179, 2000.

[67] B. G. S. P. A. Martin and K. Hess, "Electric field enhanced emission from non-coulombic traps in semiconductors," *J. Appl. Phys.*, vol. 52, 1981.

[68] V. Chmill, E. Garutti, R. Klanner, M. Nitschke, and J. Schwandt, "Study of the breakdown voltage of SiPMs," *Nucl. Instrum. Meth. A*, vol. 845, pp. 56–59, 2017.

[69] "Characterisation of sipms," *Nuclear Instruments and Methods in Physics Research Section A: Accelerators, Spectrometers, Detectors and Associated Equipment*, vol. 926, pp. 36 – 56, 2019, silicon Photomultipliers: Technology, Characterisation and Applications. [Online]. Available: http://www.sciencedirect.com/science/article/pii/S0168900218317091

[70] Y. Musienko, A. Heering, R. Ruchti, M. Wayne, Y. Andreev, A. Karneyeu, and V. Postoev, "Radiation damage of prototype sipms

for the cms hcal barrel phase i upgrade," *Nuclear Instruments and Methods in Physics Research Section A: Accelerators, Spectrometers, Detectors and Associated Equipment*, vol. 912, pp. 359 – 362, 2018, new Developments In Photodetection 2017. [Online]. Available: http://www.sciencedirect.com/science/article/pii/S0168900217314651

[71] M. Simonetta, M. Biasotti, G. Boca, P. Cattaneo, M. De Gerone, F. Gatti, R. Nardò, M. Nishimura, W. Ootani, G. Pizzigoni, M. Prata, M. Rossella, N. Shibata, Y. Uchiyama, and K. Yoshida, "Test and characterisation of sipms for the megii high resolution timing counter," *Nuclear Instruments and Methods in Physics Research Section A: Accelerators, Spectrometers, Detectors and Associated Equipment*, vol. 824, pp. 145–147, 2016, frontier Detectors for Frontier Physics: Proceedings of the 13th Pisa Meeting on Advanced Detectors. [Online]. Available: https://www.sciencedirect.com/science/article/pii/S0168900215013856

[72] L. L. Futlik, E. V. Levin, S. L. Vinogradov, V. E. Shubin, D. A. Shushakov, K. Y. Sitarskii, and E. V. Shelegada, "Methodical problems of crosstalk probability measurements in solid-state photomultipliers," *Bulletin of the Lebedev Physics Institute*, vol. 38, pp. 302–310, 11 2011.

[73] G. Zappalà, F. Acerbi, A. Ferri, A. Gola, G. Paternoster, V. Regazzoni, N. Zorzi, and C. Piemonte, "Study of the photo-detection efficiency of FBK high-density silicon photomultipliers," *Journal of Instrumentation*, vol. 11, no. 11, pp. P11 010–P11 010, nov 2016. [Online]. Available: https://doi.org/10.1088/1748-0221/11/11/p11010

[74] F. Tommasino, M. Rovituso, S. Fabiano, S. Piffer, C. Manea, S. Lorentini, S. Lanzone, Z. Wang, M. Pasini, W. Burger, C. La Tessa, E. Scifoni, M. Schwarz, and M. Durante, "Proton beam characterization in the experimental room of the trento proton therapy facility," *Nuclear Instruments and Methods in Physics Research Section A: Accelerators, Spectrometers, Detectors and Associated Equipment*, vol. 869, pp. 15–20, 2017. [Online]. Available: https://www.sciencedirect.com/science/article/pii/S0168900217306654

[75] F. Tommasino, M. Rovituso, E. Bortoli, C. La Tessa, G. Petringa, S. Lorentini, E. Verroi, Y. Simeonov, U. Weber, P. Cirrone, M. Schwarz, M. Durante, and E. Scifoni, "A new facility for proton radiobiology at the trento proton therapy centre: Design and implementation," *Physica Medica*, vol. 58, pp. 99–106, 2019. [Online]. Available: https://www.sciencedirect.com/science/article/pii/S1120179719300213

[76] F. Fiore *et al.*, "The HERMES-Technologic and Scientific Pathfinder," in *SPIE Astronomical Telescopes + Instrumentation 2020*, 1 2021.

[77] M. Kruglanski, E. de Donder, N. Messios, L. Hetey, S. Calders, H. Evans, and E. Daly, "Space Environment Information System (SPENVIS)," in *38th COSPAR Scientific Assembly*, vol. 38, Jan. 2010, p. 8.

[78] A. R. Altamura, F. Acerbi, C. Nociforo, V. Regazzoni, A. Mazzi, and A. Gola, "Characterization of silicon photomultipliers after proton irradiation up to $10^{12} n_{eq}/mm^2$," 2021.

[79] A. R. Altamura, F. Acerbi, B. D. Ruzza, E. Verroi, S. Merzi, and A. Gola, "Radiation damage on sipms for space applications," 2021.

[80] S. Vinogradov, "Perfomance of silicon photomultipliers in photon number and time resolution," 06 2016, p. 002.

[81] G. Aglieri Rinella, "The ALPIDE pixel sensor chip for the upgrade of the ALICE Inner Tracking System," *Nucl. Instrum. Methods Phys. Res., A*, vol. 845, pp. 583–587, 2017. [Online]. Available: https://cds.cern.ch/record/2239752

[82] B. Di Ruzza, "Proton and x-ray irradiation of silicon devices at the TIFPA-INFN facilities in Trento," *PoS*, vol. ICHEP2020, p. 685, 2021.

[83] G. Zappalà, F. Acerbi, A. Ferri, A. Gola, G. Paternoster, N. Zorzi, and C. Piemonte, "Set-up and methods for SiPM photo-detection efficiency measurements," *Journal of Instrumentation*, vol. 11, no. 08, pp. P08 014–P08 014, aug 2016. [Online]. Available: https://doi.org/10.1088/1748-0221/11/08/p08014

[84] "Expression of Interest for an ALICE ITS Upgrade in LS3," Oct 2018. [Online]. Available: http://cds.cern.ch/record/2644611

[85] M. Lucchini, "Development of the CMS MIP timing detector," *Nucl. Instrum. Methods Phys. Res., A*, vol. 958, p. 162090. 4 p, 2020. [Online]. Available: https://cds.cern.ch/record/2712851